POLITECNICO DI TORINO

Collegio di Ingegneria Chimica e dei Materiali

Master of Science course
in Materials Engineering

Master of Science Thesis

Fabrication of Chitosan/ Recycled Polyethylene Terephthalate Nanofibrous Membrane for Oil-Water Separation

Supervisors

Prof Kenji Kinashi – Kyoto Institute of Technology
Prof Marco Sangermano – Politecnico di Torino
Ph.D. candidate Hoan Doan Ngoc

Candidate

Andrea Baggio

October 2020

Riassunto

Introduzione

Negli ultimi decenni, l'attenzione verso le tematiche riguardanti l'impatto ambientale è diventata via via sempre più importante nel dibattito pubblico. In particolare, i temi legati alla corretta gestione e smaltimento delle acque reflue e all'inquinamento degli oceani dovuto alla dispersione di petrolio e altri derivati sono diventati di primaria importanza a livello [1, 2]. Anche se la quantità di oli provenienti da grandi incidenti petroliferi è in continuo calo, esistono numerose altre fonti come le regolari operazioni delle piattaforme petrolifere, il trasporto, scarti industriali o municipali, che, insieme, contribuiscono in maniera importante all'inquinamento dell'ecosistema marino [3, 4]. Negli anni sono state elaborate diverse tecniche per la separazione dell'acqua dagli inquinanti oleosi come ad esempio i separatori API [5], separatori a centrifuga [6] e gli idrocicloni [7, 8]. Sfortunatamente la maggior parte di queste strumentazioni richiedono grandi quantità di energia e di tempo per essere utilizzate. Per questo motivo, negli ultimi anni, molti studi si sono concentrati progettazione di membrane che consentissero il filtraggio meccanico di emulsioni di oli in acqua e viceversa [9–15]. Tra queste, le membrane composte di nanofibre polimeriche realizzate per elettrofilatura rappresentano un'interessante alternativa grazie alla loro elevata flessibilità di utilizzo e alle alte performance di separazione [16–18]. Per fabbricare questi filtri sono stati utilizzati diversi tipi di polimeri come polisulfonati [19], poliimmidi [20], polistirene [21], polivilidenfluoruro [22], e poliuretani [23].

Per rispondere alla crescente domanda di metodi sostenibili e a basso costo per produrre le membrane, alcuni studi hanno anche esplorato la possibilità di utilizzare materiale riciclato per ottenere la separazione di olio e acqua. Per esempio, W. Liu et al. hanno progettato una membrana per la separazione di emulsioni e semplici miscele di olio e di acqua composta da una rete in acciaio inossidabile ricoperta da fibre prodotte da filtri delle sigarette riciclati [24]. Anche P. Sow et al. hanno realizzato una membrana super oleofilica per la purificazione degli oli. Per farlo è stato filato del polistirene riciclato tramite la tecnica di *blow spinning*. I risultati dei test di separazione ottenuti hanno mostrato efficienze superiori al 97% [25].

Il Polietilene tereftalato (PET) è un poliestere termoplastico a basso costo. Questo polimero è molto utilizzato nei settori del packaging, automotive, elettrico, elettronico e, in particolare, nell'industria tessile [26], che rappresenta il principale mercato del PET [27]. Il crescente utilizzo di questo polimero, specialmente nella produzione di bottiglie, ha reso la gestione del fine vita di questo materiale un problema sempre meno trascurabile. Negli anni sono state elaborate diverse tecnologie per il riciclo del PET [28] e per il riutilizzo del materiale recuperato [29–31]. Sfortunatamente, il PET riciclato (r-PET) dalle bottiglie è spesso utilizzato per la produzione di oggetti a basso valore aggiunto, così che i profitti generati risultino relativamente bassi. L'utilizzo del r-PET come materiale di base per la produzione di membrane fibrose per la separazione di olio e acqua potrebbe portare al duplice vantaggio di minori costi rispetto al materiale vergine e una riduzione dell'impatto ambientale. Infatti, un aumento del valore aggiunto dei prodotti in r-PET incoraggerebbe la raccolta e il riciclo di questo polimero, riducendo così la dispersione di questa tipologia di plastica nell'ambiente. Alcuni studi sono già stati condotti sull'utilizzo di PET riciclato per la fabbricazione di filtri composti da fibre. N. Zander et al. hanno prodotto con successo nanofibre di r-PET per il filtraggio di particelle dai 30 ai 2000 nm disperse in acqua [32]. In un lavoro precedente sono state testate le capacità di filtraggio di membrane di r-PET funzionalizzate, raggiungendo efficienze di separazione maggiori [33].

Recentemente sono state introdotte anche membrane fibrose definite smart, capaci quindi di controllare il processo di separazione tramite la risposta a diversi stimoli come la temperatura [34], il pH [35], la luce UV [36], il numero di ioni nel mezzo liquido [37], un campo elettrico [14], e la pre-immersione della membrana (*prewetting*) [10, 38]. Proprio quest'ultima tipologia di filtri è considerata la più promettente grazie alla facilità di fabbricazione e utilizzo. La membrana utilizzata nei processi di pre-bagnatura deve possedere proprietà anfifiliche, così da ottenere un comportamento super idrofobico quando immersa in un olio e super oleofobico quando immersa in acqua. In questo modo, quando la membrana sarà pre-bagnata con un olio, quest'ultimo sarà libero di fluire attraverso la membrana, mentre l'acqua verrà trattenuta sulla superficie del filtro. Al contrario, quando la membrana viene precedentemente immersa in acqua, gli oli saranno trattenuti, mentre

l'acqua verrà filtrata. In questo modo, scegliendo il liquido con cui bagnare il filtro, è possibile controllare la natura del prodotto separato, così da poter utilizzare il medesimo prodotto sia con emulsioni di olio in acqua che viceversa.

In uno studio precedente [33] sono state già dimostrate le proprietà super idrofobiche e super oleofiliche delle membrane fibrose realizzate in r-PET. Tuttavia, al fine di ottenere un materiale anfifilico è necessaria un'ulteriore funzionalizzazione di tali prodotti. In questo studio è stato elaborato un metodo semplice e sostenibile che si propone di modificare il r-PET con il chitosano, un polimero idrofilo e biodegradabile. È ragionevole aspettarsi che le nanofibre prodotte da tale blend manifestino le proprietà anfifiliche, grazie alla contemporanea presenza di gruppi idrofobici dal PET e idrofili dal chitosano.

Materiali e metodi

Materiali

I pellet di PET riciclato da bottiglie di acqua (CR-8816) usate sono stati gentilmente forniti dal Dr. Kazushi Yamada (Advanced Fibro-Science, Kyoto Institute of Technology, Kyoto, Japan). Il chitosano (grado di deacetilazione 75-85%, peso molecolare basso: 50-190 kDa) e il dodecilbenzensulfonato di sodio sono stati prodotti da Sigma-Aldric. L'acido trifluoroacetico (TFA), il tetracloruro di carbonio, il tetracloroetilene e il sorbitano monoleato sono stati ottenuti dalla Wako Co., Osaka, Japan. Il kerosene, l'esano e l'idrogenocarbonato di sodio sono stati forniti dalla Nacalai Tesque, Kyoto, Japan. Tutti i prodotti chimici sono stati usati senza ulteriori purificazioni.

Elettrofilatura

Prima di tutto sono state preparate otto soluzioni contenenti una quantità costante di rPET e una concentrazione di chitosano crescente. La prima soluzione, composta solamente per l'8 wt% da r-PET, è stata usata come riferimento in molte misurazioni. Essa è stata preparata aggiungendo il corretto quantitativo di pellets a del TFA, successivamente il preparato è stato miscelato tramite una centrifuga planetaria (ARE-310, Thinky Co., Tokyo, Japan) a 2000 rpm per 28.5 minuti, seguito da un ciclo di degassaggio a 2200 rpm per 1.5 minuti. Le restanti soluzioni sono formate da un contenuto crescente di chitosano, da 1 wt% a 4 wt%. In questo caso, per ottenere una miscela più omogenea, i due polimeri sono stati aggiunti al solvente separatamente. Prima di tutto il chitosano è stato disciolto nel TFA seguendo una procedura simile a quanto visto in precedenza. Successivamente i pellet di r-PET sono stati aggiunti e il composto è stato miscelato nuovamente. Al termine del processo, le soluzioni sono state lasciate circa 10 ore sopra un agitatore magnetico per omogeneizzare ulteriormente la miscela.

Le membrane fibrose sono state realizzate tramite un macchinario per l'elettrofilatura progettato e costruito nel nostro laboratorio. La velocità del flusso della soluzione durante il processo è stata mantenuta a 0.5 mL h^{-1} da una pompa per siringa (KDS-100, KD Scientific Inc., Massachusetts, USA). Un alimentatore ad alta tensione (HVU-30P100, MECC Co., Japan) è stato usato per generare una tensione di 15 kV all'ago (30 G) collegato alla siringa. Un cilindro metallico avente diametro di 61 mm, una velocità di rotazione di 120 rpm e ricoperto da una rete di Nylon (No. 34), è stato posto a 12.5 cm dall'ago della siringa e utilizzato come collettore. Durante il processo di elettrofilatura la temperatura e l'umidità relativa sono state monitorate da un igrotermografo e sono state mantenute pari a 22.5 ± 4.0 °C e 42 ± 8%, rispettivamente. Utilizzando la procedura appena descritta sono state preparate otto membrane aventi rapporti chitosano/r-PET nelle fibre differenti: 0.0/8, 1.0/8, 1.5/8, 2.0/8, 2.5/8, 3/8, 3.5/8 e 4/8. Per maggiore chiarezza, le membrane verranno identificate di qui in avanti con le seguenti denominazioni: as-spun r-PET, r-PET@Chit1, r-PET@Chit1.5, r-PET@Chit2, r-PET@Chit2.5, r-PET@Chit3, r-PET@Chit3.5 e r-PET@Chit4.

Successivamente al processo di elettrofilatura, le membrane sono state neutralizzate, immergendole in una soluzione acquosa di idrogenocarbonato di sodio ($NaHCO_3$) sovrasatura per almeno 6 ore. In seguito, le stesse sono state risciacquate in acqua pura per più volte e poi asciugate a 50 °C per 4 ore. Le membrane così ottenute

verranno denominate rispettivamente r-PET@Chit1_n, r-PET@Chit1.5_n, r-PET@Chit2_n, r-PET@Chit2.5_n, r-PET@Chit3_n, r-PET@Chit3.5_n e r-PET@Chit4_n [39].

Caratterizzazione

La morfologia delle membrane è stata studiata utilizzando un microscopio elettronico a scansione con sorgente ad emissione di (FE-SEM) (JEOL-7600, JEOL Ltd., Japan). La superficie dei campioni è stata ricoperta da uno strato di 30 nm di platino, così da riuscire a raccogliere le immagini utilizzando un fascio di elettroni accelerato a 15 V. I valori di diametro medio sono stati misurati processando le immagini di 100 fibre per ogni membrana tramite il software ImageJ. Un microscopio 3D a scansione laser (VK-2000, Keyence Co., Japan) è stato utilizzato per determinare la rugosità superficiale tramite una profilometraggio laser senza contatto. La viscosità delle soluzioni è stata valutata utilizzando un viscosimetro vibrazionale (SV-1 and SV-100, A&D, Tokyo, Japan). La loro conducibilità è stata invece misurata tramite un Oakton PC700 pH/mV/Conductivity/°C metro da banco (Oakton Instruments, Vernon Hills, IL, USA). Uno spettrometro a infrarossi a trasformata di Fourier (FT/IR 4700, JASCO International Co., Japan), equipaggiato con un accessorio universale a riflettanza totale attenuata (ATR), è stato usato per raccogliere lo spettro IR dei provini nel range di lunghezze d'onda da 4000 a 400 cm^{-1}. La composizione chimica della superficie delle membrane è stata ulteriormente investigata tramite l'utilizzo di una spettroscopia fotoelettronica a raggi X (XPS) (JEOL 9010, JEOL Ltd., Japan). Le proprietà meccaniche delle membrane neutralizzate sono state valutate utilizzando un macchinario universale per prove di trazione (TENSILON RTF-1210, A&D Co., Japan) con una velocità della traversa di 1 mm s^{-1} e la cella di carico di 100 N. I provini con uno spessore di circa 50 μm sono stati tagliati a forma di osso di cane (tipo 5B in BS ISO 527: 2012) e incollati ad un supporto rettangolare di carta 20x30 mm, con un'apertura centrale di dimensioni 4x25 mm. Questa soluzione è stata adottata per permettere di posizionare i provini con più facilità nel macchinario, evitando il più possibile che questi venissero danneggiati. Prima della misura le parti laterali del supporto di carta sono state tagliate per evitare di falsare la misurazione. L'analisi degli angoli di contatto (CA) è stata condotta utilizzando un Phoenix 300 (Kromtek Co., Malaysia). Le immagini raccolte sono state poi processate tramite il software ImageJ. Durante la misurazione, le membrane sono state incollate ad un vetrino da laboratorio e poste in aria, in acqua oppure in vari tipi di oli per misurare rispettivamente gli angoli di contatto dell'acqua (WCA), degli oli (OCA), degli oli con la membrana immersa in acqua (*under water oil contact angle*, UWOCA) e dell'acqua con la membrana immersa negli oli (*under oil water CA*, UOWCA). Per questa misurazione sono stati utilizzati quattro tipi diversi di solventi: il kerosene, l'esano, il tetracloruro di carbonio (CTC) e il tetracloroetilene (TCE). Per come sono state progettate le membrane, durante il processo di separazione, il liquido che viene trattenuto dalla membrana si accumula sopra di essa. In questo modo aumenta la pressione che la colonna di liquido esercita sul filtro. Quando questa pressione supera un certo livello di soglia, detto pressione di intrusione, la membrana non è più in grado di respingere il fluido selezionato. Per misurare tale limite le membrane sono state tagliate con una forma circolare del diametro di 25 mm e poste all'interno di un apposito portafiltro KGS-25 (Advantec CO., Japan), equipaggiato con un supporto formato da una rete di acciaio inossidabile. La membrana è stata così pre-bagnata con il liquido più denso (acqua nel caso del test per la pressione di intrusione del kerosene e dell'esano, CTC e TCE negli altri casi) e la parte superiore del portafiltro è stata riempita con 10 ml del liquido più leggero. Tramite un flusso controllato di azoto, la pressione sulla membrana è stata aumentata fino a che la prima goccia di solvente è permeata attraverso il filtro. Il valore di pressione letto sul manometro è stato poi utilizzato per calcolare il valore di pressione di intrusione tramite la seguente equazione:

$$p_i = (p_f - p_0) + \rho_l g h_l \quad (1)$$

dove p_i identifica la pressione di intrusione, p_f il valore della pressione letta sul manometro, p_0 is la pressione atmosferica, ρ_l la densità del liquido trattenuto dalla membrana, g l'accelerazione gravitazionale e h_l è l'altezza della colonna di liquido sopra il filtro. In Fig. 4.6 è riportata una rappresentazione schematica della strumentazione utilizzata.

Test di separazione olio-acqua

La capacità della membrana nel filtrare sia miscele che emulsioni di olio e acqua è stata valutata utilizzando un sistema di filtraggio composto dallo stesso portafiltro utilizzato in precedenza. Per queste misurazioni è stata scelta la membrana che avesse mostrato le caratteristiche più promettenti nelle analisi precedenti, ovvero la r-PET@Chit2. Questa è stata così tagliata in campioni circolari di diametro di 25 mm, pre-bagnata con il liquido corrispondente e posta all'interno del portafiltro.

Per quanto riguarda la separazione di semplici miscele, sono stati utilizzati i quattro tipi di oli già visti in precedenza: il kerosene, l'esano, il CTC e il TCE. Per il test, l'acqua è stata colorata utilizzando un colorante blu, mentre gli oli con uno rosso, così da distinguerli più facilmente. In seguito, le membrane sono state bagnate con l'acqua o l'olio corrispondente e 20 ml di miscela di olio/acqua (rapporto in volume di 1/1) sono stati versati nel portafiltro. Nel caso in cui l'acqua è stata separata dagli oli leggeri, il filtro è stato pre-bagnato con l'acqua, altrimenti è sono stati usati gli oli pesanti. Durante il test il liquido più denso, filtrato dalla membrana, è stato raccolto in un becher. Il flusso (J) attraverso la membrana è stato calcolato mediante la seguente equazione:

$$J = \frac{V}{At} \tag{2}$$

dove V è il volume del liquido raccolto, t il tempo di durata del test e A è l'aera effettiva di filtraggio. Dall'altra parte, l'efficienza di separazione è stata calcolata mediante l'equazione:

$$\eta_m = \frac{M}{M_0} \times 100\% \tag{3}$$

dove η_m è l'efficienza di separazione, M il peso del liquido raccolto nel becher e M_0 è il peso iniziale del liquido separato prima del test.

Le emulsioni, invece, sono state preparate utilizzando due diversi emulsionanti: il sorbitano monoleato per le emulsioni di acqua in olio e il dodecilbenzensulfonato di sodio per quelle di olio in acqua. Prima di tutto alla fase continua è stato aggiunto lo 0.1 wt% di emulsionante. La soluzione è stata quindi miscelata tramite un dispersore Ultra Turrax IKA T-18 (IKA; Werke GmbH & Co. KG, Staufen, Germany) per 5 minuti a 18,000 rpm. Successivamente, la fase dispersa è stata aggiunta con una concentrazione dell'1 wt% e miscelata nuovamente per 5 minuti. La dimensione delle particelle di emulsione è stata misurata tramite un'analisi della diffusione dinamica della luce (DLS) (ELSZ-1000, Otsuka Electronics Co., Ltd., Osaka, Japan).

Come già fatto in precedenza, i campioni sono stati preparati e disposti nel portafiltro. Questo è stato poi riempito con 15 ml di emulsione – mantenuti constanti per non alterare la pressione applicata alla membrana. Dopo 1 minuto, il liquido filtrato è stato pesato per calcolare il valore del flusso mediante l'Equazione **Errore. L 'origine riferimento non è stata trovata.**. La concentrazione della fase dispersa post filtraggio è stata misurata tramite un gascromatografo-spettrometro di massa (GCMS-QP2010 Ultra, Shimadzu, Kyoto, Japan) per le emulsioni di olio in acqua e un Karl Fischer Moisture Tritator MKC-710 (Kyoto Electronics Manufacturing Co., Kyoto, Japan) per le emulsioni di acqua in olio. I risultati di queste misurazioni sono stati quindi usati per calcolare le efficienze di separazione secondo la seguente formula:

$$\eta_e = \frac{C_i - C_f}{C_i} \times 100\% \tag{4}$$

dove η_e rappresenta l'efficienza e C_i and C_f le concentrazioni della fase dispersa rispettivamente prima e dopo il filtraggio.

Discussione dei risultati

Morfologia

Come è stato già dimostrato in studi precedenti la morfologia della membrana e in particolare la sua rugosità può influenzare in maniera significativa le proprietà superficiali del prodotto, in particolare la sua bagnabilità e di conseguenza le capacità di separazione [40].

Per questo motivo il diametro medio delle fibre e, in generale, la loro morfologia è stata studiata con attenzione. Come viene mostrato in Figura 1, anche a partire da basse concentrazioni di chitosano (da 1.5 wt% in soluzione) le fibre presentano un aspetto uniforme e liscio, con l'assenza dei rigonfiamenti tipici di un processo di elettrofilatura instabile (Sezione 3.2.3).

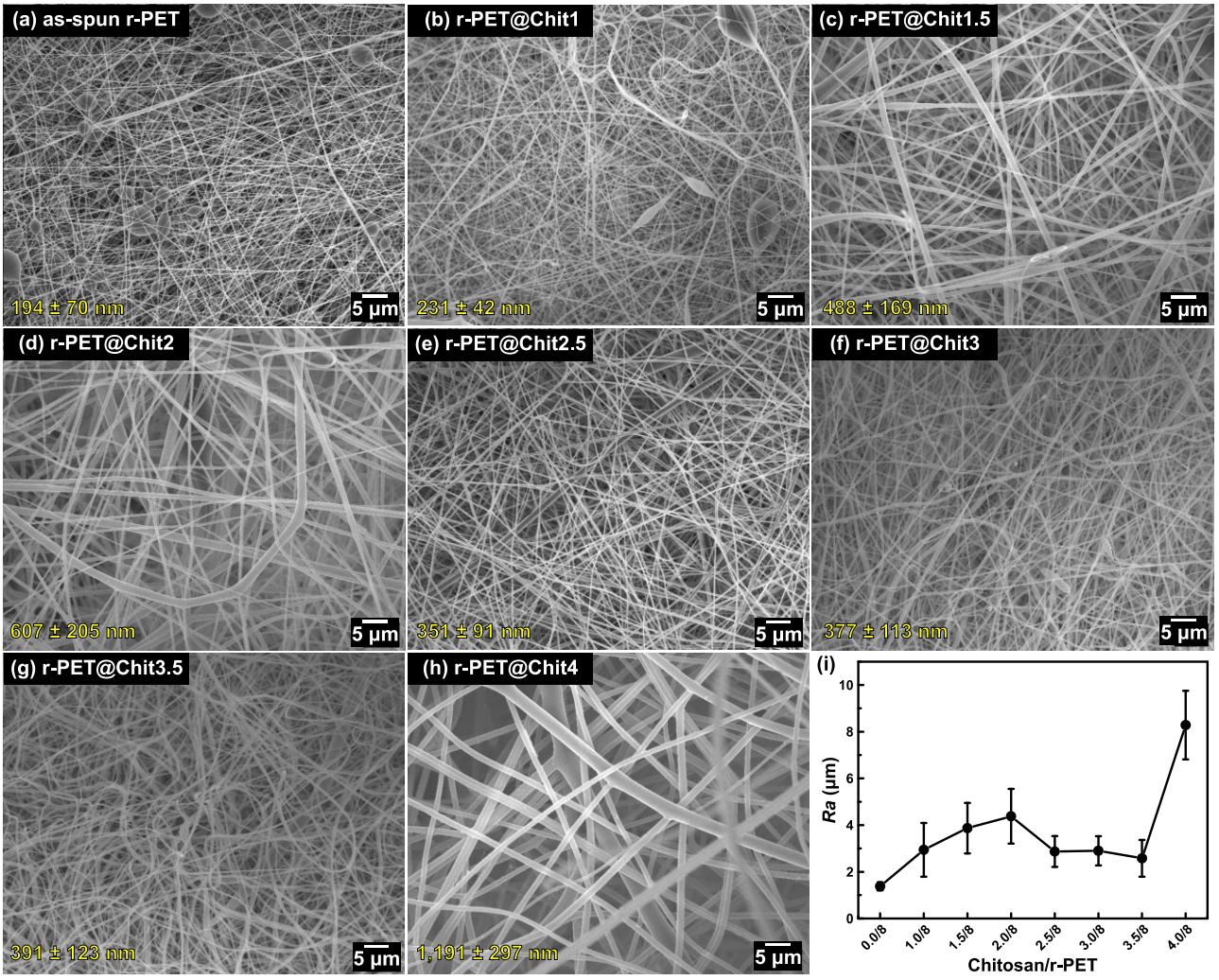

Figura 1. Immagini raccolte al FE-SEM usando il segnale degli elettroni secondari raffiguranti le membrane (a) as-spun r-PET, (b) r-PET@Chit1, (c) r-PET@Chit1.5, (d) r-PET@Chit2, (e) r-PET@Chit2.5, (f) r-PET@Chit3, (g) r-PET@Chit3.5 e (h) r-PET@Chit4. (i) Rappresentazione dei valori di rugosità delle diverse membrane con concetrazioni crescenti di chitosano.

I valori di diametro medio delle fibre, misurati tramite l'analisi al FE-SEM e riportati in **Figura 1**, mostrano un comportamento particolare; infatti, inizialmente, un aumento nella concentrazione di chitosano in soluzione corrisponde ad un conseguente aumento del diametro delle fibre – da ca. 194 a 607 nm. A partire dal r-PET@Chit2.5 lo spessore delle fibre diminuisce bruscamente e rimane constante per le concentrazioni superiori, per poi crescere nuovamente alla concentrazione del 4 wt% di chitosano (**Figura 1**).

Le misurazioni della rugosità delle membrane eseguite tramite il microscopio laser, hanno dimostrato una correlazione stretta fra questa grandezza e la dimensione delle fibre. Infatti, come è possibile notare da Figura 1i, l'andamento della rugosità dei campioni segue in maniera molto simile quello relativo al diametro medio delle fibre.

Come spiegato nella Sezione 3.3.4, durante il processo di elettrofilatura, le proprietà della soluzione come la conducibilità e la viscosità giocano un ruolo fondamentale nel determinare la morfologia delle fibre. In

particolare, è stato dimostrato che un aumento della viscosità determina un conseguente aumento nella dimensione delle fibre, mentre conducibilità elevate facilitano lo stiro del filamento polimerico, risultando in fibre più fini. Dalla misurazione di queste due grandezze è stato notato come un incremento del contenuto di chitosano produce un conseguente aumento sia della conducibilità che della viscosità della soluzione. Le evidenze sperimentali mostrano come per basse concentrazioni di chitosano l'effetto dell'aumento della viscosità risulta essere più marcato, mentre per concentrazioni superiori al 2.5 wt%, la conducibilità giochi un peso maggiore nel determinare la morfologia del filato.

Composizione chimica

La composizione chimica delle fibre influenza un modo cruciale le proprietà superficiali della membrana, quindi la sua bagnabilità e le sue prestazioni di filtraggio. Per questo motivo sono stati collezionati gli spettri IR relativi alle membrane a diverse concentrazioni di chitosano. Come viene mostrato in Figura 2a, i campioni analizzati mostrano dei picchi di assorbimento a 1675 cm^{-1} e 1530 $cm^{-1,}$ che corrispondono al segnale relativo allo stretching di gruppi amminici protonati (NH_3^+). Inoltre, la debolezza dei segnali a 3300 e 3400 cm^{-1} (stretching dei gruppi amminici) e la presenza di un picco a 1200 cm^{-1} (gruppi carbossilati) e di tre nell'intervallo fra 840-720 cm^{-1} suggeriscono la presenza di tracce di acido trifluoroacetico nelle fibre sotto forma di Sali amminici [39, 41, 42].

Per uno studio più completo è stata realizzata un'analisi XPS nell'intervallo energetico fra 1000 e 0 eV. I risultati, riportati in **Figura 2**b, hanno confermato la presenza di solvente residuo, resa evidente dal segnale a 688 eV, associato alla presenza di fluoro sulla superficie delle fibre. Inoltre, per le diverse concentrazioni di chitosano nelle fibre sono presenti i segnali relativi al C1s, O1s e N1s, che suggeriscono la contemporanea presenza di r-PET e chitosano sulla superficie del filato, come voluto in fase di progettazione delle membrane.

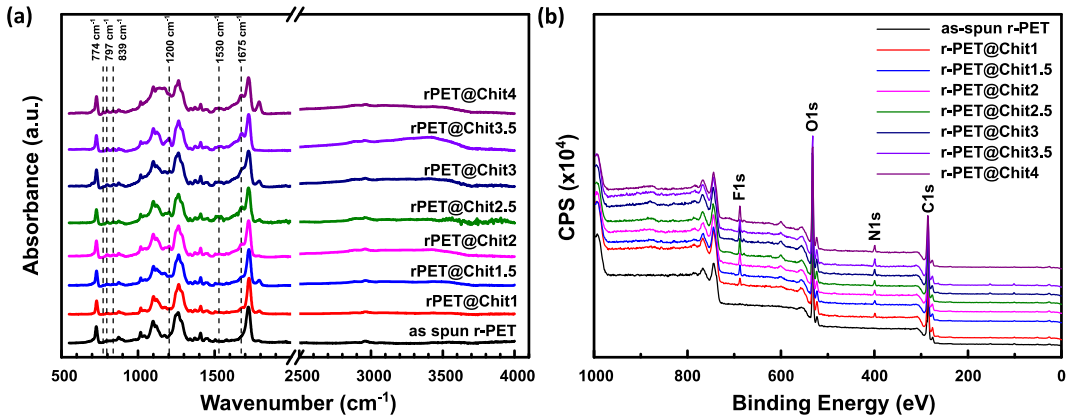

Figura 2. Spettri (a) FT-IR e (b) XPS delle membrane elettrofilate con un crescente contenuto di chitosano nelle fibre.

Qualora le membrane fossero immerse in acqua, i residui di sale presenti sulla superficie potrebbero disciogliersi, inquinando il fluido con un componente potenzialmente tossico e acidificandolo, causando così la dissoluzione del chitosano [49]. Questo rende necessario un processo di neutralizzazione della membrana per eliminare ogni traccia residua di TFA. Per questo motivo il trattamento chimico con la soluzione sovrasatura di $NaHCO_3$, descritto in precedenza, è stato applicato a tutti i campioni. Come si può evincere dalle misurazioni eseguite tramite l'FT-IR e l'XPS (Figura 3) il trattamento si è rivelato utile nell'eliminazione totale dei sali amminici. Inoltre, dalle immagini raccolte al FE-SEM dopo il trattamento (Fig. 5.6), si può anche notare come le fibre non subiscano alcun danno a seguito della neutralizzazione. Invece, i valori di R_a misurati tramite l'utilizzo del microscopio laser mostrano come, durante il trattamento chimico, le fibre si riorganizzino determinando così una generale diminuzione della rugosità superficiale (Fig. 5.6).

Dal momento che la quantità di chitosano sulla superficie delle fibre determina il numero di gruppi idrofili presenti, influenzando direttamente le proprietà di filtraggio delle membrane, l'analisi dell'XPS è stata usata per uno studio più approfondito sulla composizione chimica superficiale delle membrane. In particolare, sono state misurate le concentrazioni atomiche degli elementi presenti sulla superficie di un film di r-PET e della

polvere di chitosano. I valori trovati sono quindi stati usati per calcolare la concentrazione teorica degli elementi sulla superficie delle membrane con un contenuto di chitosano crescente, come spiegato in modo più approfondito nella Sezione 5.2.2. Comparando tali risultati con le concentrazioni misurate sperimentalmente dai campioni (Tabella 1) è possibile notare che la concentrazione di azoto sulla superficie delle fibre risulti essere più alta di quella attesa. Questo risultato suggerisce che il chitosano tende a concentrarsi maggiormente sulla superficie delle fibre rispetto che nella loro parte più interna [43]. Una possibile spiegazione di questo fenomeno può essere ricondotta al fatto che durante il processo di elettrofilatura le cariche libere siano forzate ad accumularsi nella parte esterna del flusso polimerico, così il chitosano disciolto, ricco di gruppi protonati, è stato spinto verso la superficie.

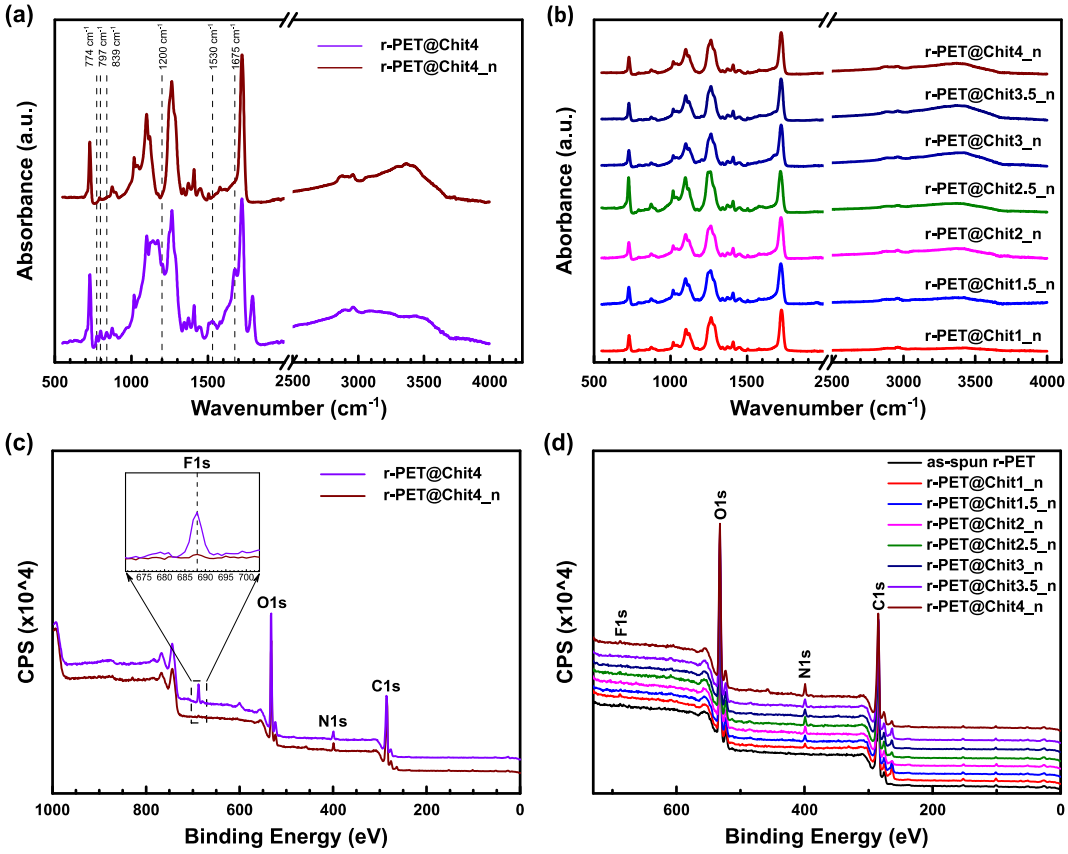

Figura 3. (a) Spettro FT-IR della membrana r-PET@Chit4 prima e dopo la neutralizzazione. I picchi relativi alla presenza di TFA sono evidenziati. (b) Comparazione degli spettri IR di assorbimento di tutti i campioni neutralizzati. (c) Segnale XPS della membrana r-PET@Chit4 prima e dopo la neutralizzazione. La regione del picco F1s è stata ingrandita per valutare meglio la differenza di intensità del segnale. (d) Spettri XPS delle membrane con diversi contenuti di chitosano dopo la neutralizzazione.

Tabella 1. Confronto fra le percentuali atomiche di azoto sulla superficie delle membrane e quella teorica, calcolata a partire da un campione di polvere di chitosano e un film di r-PET.

Campione	%at N	
	membrana	teorico
r-PET@Chit1	1.21	0.67
r-PET@Chit1.5	1.53	0.97
r-PET@Chit2	1.95	1.23
r-PET@Chit2.5	1.92	1.49
r-PET@Chit3	1.94	1.67
r-PET@Chit3.5	1.91	1.87
r-PET@Chit4	3.12	2.05

Proprietà meccaniche

Le membrane sono state studiate anche nelle loro proprietà meccaniche. I diagrammi sforzo-deformazione riportati in Fig. 5.8 mostrano la tendenza del filato di rompersi con un meccanismo in due stadi: inizialmente l'incremento di carico applicato alla membrana genera solamente una piccola deformazione, che da un certo punto in poi incrementa sensibilmente fino alla rottura del campione. La diminuzione della pendenza della curva di sforzo-deformazione può essere spiegata dalla presenza, all'interno della membrana, di zone in cui le fibre si intrecciano fra loro [44]. Infatti, durante il primo step, i segmenti di fibra compresi fra due punti di intreccio consecutivi vengono allineati e allungate dallo sforzo applicato. Una volta raggiunto un certo livello di stress avviene la rottura di alcuni di questi legami fra le fibre, causando una diminuzione della rigidità complessiva delle membrane. Dal momento che l'allineamento delle fibre nelle membrane non è ordinato e che può essere modificato dalla riorganizzazione spaziale delle fibre durante il processo di neutralizzazione, le caratteristiche meccaniche dei filati risultano essere poco controllabili e non seguire un andamento preciso con l'incremento del chitosano nella composizione delle fibre.

Bagnabilità

L'effetto della concentrazione di chitosano sulla bagnabilità delle membrane in diverse condizioni ambientali è stata studiata tramite la misurazione dell'angolo di contatto dell'acqua e di diversi tipi di oli. Come è stato osservato già in un lavoro precedente [33], le membrane fibrose di r-PET mostrano valori di WCA circa uguali a 134.0°, grazie agli alti valori di rugosità superficiale mostrati da tali prodotti. Invece, con l'aggiunta di chitosano nelle fibre, le membrane hanno mostrato un comportamento super idrofilo, senza modificare la super oleofilicità già presente con il solo r-PET (Figura 4a). Questo cambiamento nella bagnabilità della membrana è attribuibile alla presenza del biopolimero sulla superficie delle fibre. Infatti, il chitosano possiede molti gruppi idrofili che possono interagire con l'acqua [45]. Le proprietà anfifiliche delle membrane sono poi state studiate ulteriormente immergendo i filtri in acqua e nell'esano e misurando rispettivamente l'angolo di contatto di un olio e dell'acqua. In questo modo si è osservata la formazione di un sistema trifase solido/acqua/olio stabile [12], riconducibile ad una super oleofobicità in acqua e una super idrofobicità in olio (Figura 4b-e). Ad eccezione della membrana as-spun r-PET in acqua, quando il campione è stato immerso in un liquido, che fosse acqua o olio, questo si è legato alle fibre, formando uno strato attorno ad esse. Nel momento in cui un altro liquido immiscibile entra in contatto con un sistema simile, esso viene respinto dall'acqua/olio sulla superficie, assumendo una forma quasi sferica [9, 12, 38]. Si può quindi ritenere che l'aggiunta di chitosano conferisca alla membrana la capacità di respingere diverse categorie di solventi solamente bagnandola con il liquido opposto. Le osservazioni sperimentali hanno mostrato che l'UWOCA e UOWCA non viene modificato in maniera significativa all'aumentare del contenuto di chitosano, rimanendo sempre superiore ai 150° per ogni campione. In particolare, la coppia di valori di angoli di contatto più alta appartiene alla membrana r-PET@Chit2, che mostra valori di UWOCA pari a 168.0 ± 1.9° e di UOWCA pari a 168.1 ± 2.5°. L'influenza del tipo di solvente utilizzato sulla bagnabilità delle superfici è stata studiata ripetendo l'analisi degli CA utilizzando il kerosene, il CTC (CCl_4) e il TCE (C_2Cl_4). Come mostrato in Figura 4f, l'UWOCA e l'UOWCA non vengono modificati di molto, risultando in valori compresi fra 160° e 175° con tutti gli oli selezionati.

In aggiunta, l'altezza massima della colonna di liquido che la membrana può trattenere prima che una goccia riesca a passarle attraverso è stata misurata tramite la valutazione della pressione di intrusione per l'acqua e diversi oli. Nel caso delle membrane anfifiliche è necessario misurare sia la pressione di intrusione dell'acqua che quella dell'olio. Infatti, come spiegato in precedenza, quando le membrane vengono bagnate da un liquido (e.g., un olio) con un'ottima affinità (CA ≈ 0°), questo si lega alle fibre, respingendo altri liquidi immiscibili (e.g., l'acqua) depositati sulla membrana [9]. In un sistema del genere si raggiunge un equilibrio di forze che coinvolge la tensione superficiale del liquido a contatto con le pareti delle porosità che si formano fra le fibre (Sezione 2.2). La quantità di pressione che il liquido respinto deve applicare sul poro della membrana per superare la resistenza della tensione superficiale, la pressione di intrusione, può essere calcolata utilizzando la teoria di Young-Laplace [46, 47]:

$$\Delta P = \frac{2\gamma_L}{r} = -\frac{2\gamma_L \cos\theta}{R} \quad (5)$$

dove ΔP rappresenta la pressione di intrusione, γ_L la tensione superficiale del liquido depositato, r il raggio di curvatura del menisco, θ l'angolo di contatto del liquido con la superficie delle fibre e R è il raggio equivalente dei pori della membrana. Per ragioni pratiche le misurazioni sono state eseguite solamente sul campione di r-PET@Chit2 che aveva mostrato i valori di UWOCA and UOWCA più promettenti.

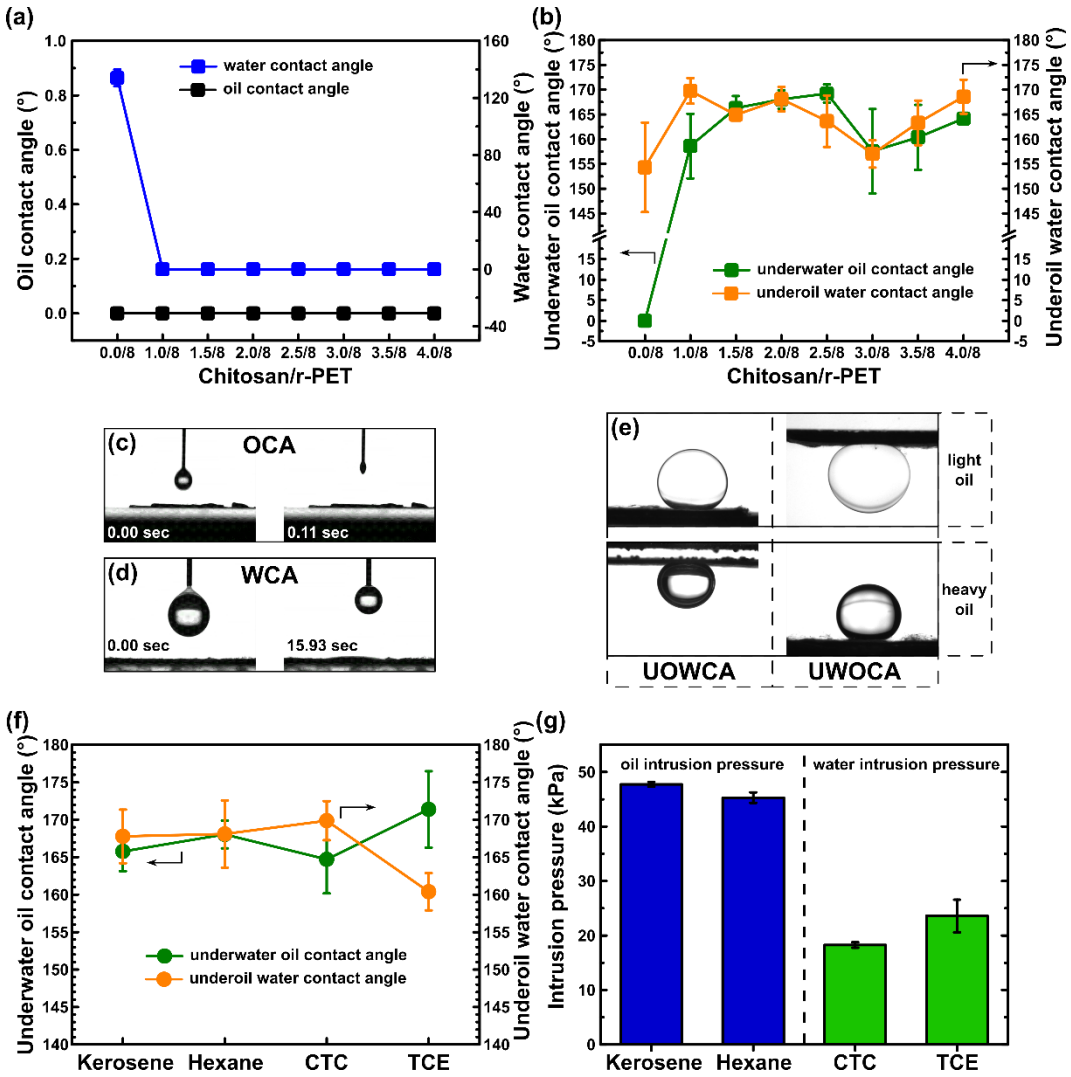

Figura 4. Sono qui riportati i valori di CA (a) di un olio (l'esano), dell'acqua, (b) dell'acqua in immersione nell'esano e dell'olio in immersione dell'acqua con le membrane a diverse concentrazioni di chitosano. (c) OCA e (d) WCA prima e dopo che la goccia di liquido sia stata completamente assorbita dalla membrana r-PET@Chit2. (e) UWOCA e UOWCA di un olio leggero (l'esano) e di uno pesante (il TCE) con il campione r-PET@Chit2. (f) UWOCA e UOWCA della membrana r-PET@Chit2 utilizzando differenti tipi di oli: kerosene, esano, CTC e TCE. (d) La membrana r-PET@Chit2 è stata usata anche per misurare le pressioni di intrusione dell'acqua e dell'olio per gli stessi tipi di solventi testati in precedenza.

Perciò la pressione di intrusione dell'acqua è stata misurata pre-bagnando le membrane con gli oli pesanti, mentre quella degli oli è stata misurata utilizzando oli leggeri con membrane pre-bagnate dall'acqua. Infatti, in un caso reale, il liquido più denso raggiunge la superficie del filtro prima di quello più leggero. In questo modo il primo verrà filtrato dalla membrana, mentre il secondo si accumulerà su di essa. Per questo motivo la quantità di fluido che il filtro può sostenere prima di perdere la sua capacità di filtraggio risulta essere un parametro molto importante da conoscere. Come mostrato in Figura 4g, la pressione di intrusione degli oli risulta essere circa costante per i due solventi utilizzati (47.7 ± 0.5 kPa per il kerosene e 45.3 ± 1.0 kPa per l'esano). Dall'altra parte, la pressione di intrusione dell'acqua risulta essere molto inferiore variando fra 18.3 ± 0.5 kPa per il CTC e 23.6 ± 3.0 kPa per il TCE. La grande differenza fra i valori di pressione di intrusione

di acqua e degli oli può essere spiegata dalla presenza dei molti gruppi idrofili sulla superficie, portati dal chitosano, che come visto in precedenza tende a concentrarsi maggiormente in questa zona. Infatti, la grande affinità con l'acqua delle membrane può favorire la sostituzione dell'olio legato alle fibre con l'acqua, causando il conseguente assorbimento del liquido e la perdita delle capacità di filtraggio.

Capacità di separazione

Infine, sono stati effettuati alcuni esperimenti di filtraggio sulla membrana r-PET@Chit2 utilizzando diversi tipi di miscele ed emulsioni di oli e acqua. In particolare, i solventi utilizzati sono il kerosene, l'esano, il CTC e il TCE. Il setup sperimentale utilizzato è raffigurato in Figura 5 e Figura 6. Il meccanismo di separazione può essere spiegato dalla stima della pressione di intrusione (ΔP) per mezzo dell'Equazione 5 [33] (Sezione 2.2). Quando l'olio o l'acqua entrano in contatto con la membrana in aria, entrambi mostrano un angolo di contatto vicino a 0°. Per cui $\Delta P < 0$ e i liquidi sono liberi di fluire attraverso la membrana. Dall'altra parte, quando la membrana è pre-bagnata con l'olio (o l'acqua) e viene depositata su di essa un po' d'acqua (oppure olio), $\theta > 90°$, il che determina un valore positivo di pressione di intrusione. In un simile sistema, il liquido depositato viene trattenuto dalla membrana. Questo meccanismo, mostrato dalla membrana progettata nel presente studio, permette di ottenere una separazione controllata dell'acqua dall'olio o viceversa solamente pre-bagnando il filtro con il liquido corrispondente.

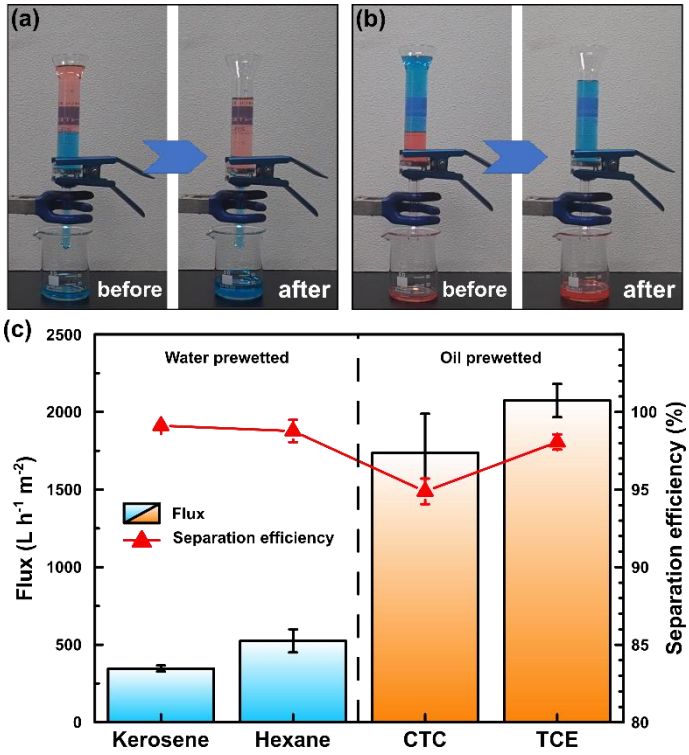

Figura 5. Foto dell'setup sperimentale utilizzato per il test di separazione delle miscele di acqua e (a) oli leggeri e (b) oli pesante. L'acqua è stata colorata con un colorante blu, mentre gli altri solventi con uno rosso. (c) Flusso ed efficienza di separazione misurate utilizzando la membrana r-PET@Chit2 e quattro diversi tipi di miscele.

Il test di separazione delle miscele è stato realizzato pre-bagnando le membrane e versando su di esse 20 ml della miscela di olio e acqua con un rapporto in volume di 1:1. I risultati hanno mostrato valori di efficienza relativamente alti, pari a 94.9% utilizzando il CTC, 98.1% con il TCE, 98.8% con l'esano e 99.1% con il kerosene (Figura 5c). I valori di flusso, invece, risultano essere compresi 346.2 e 524.5 L h^{-1} m^{-2} per le miscele con oli leggeri e fra 1737.1 e 2073.8 L h^{-1} m^{-2} per le miscele con coli più pesanti (Figura 5c). Comparando i risultati ottenuti con quelli relativi a soluzioni similari presenti in letteratura (Table 5.5), è possibile notare come i valori di flusso per la separazione di miscele di olio e acqua ad opera di membrane anfifiliche risultino mediamente inferiori a quelli ottenuti in questo studio, benché i valori di efficienza rimangano molto

competitivi. La grande differenza fra i flussi dell'acqua e quelli degli oli attraverso la membrana è probabilmente dovuta alla differenza fra la viscosità dei liquidi. Come mostrato in Table 5.7 l'acqua ha una viscosità maggiore rispetto a quella dei solventi più pesanti. In aggiunta la maggiore densità delle miscele olio pesante/acqua fa si che il flusso di queste miscele sia spinto con maggior forza attraverso i pori della membrana rispetto alle atre due miscele testate.

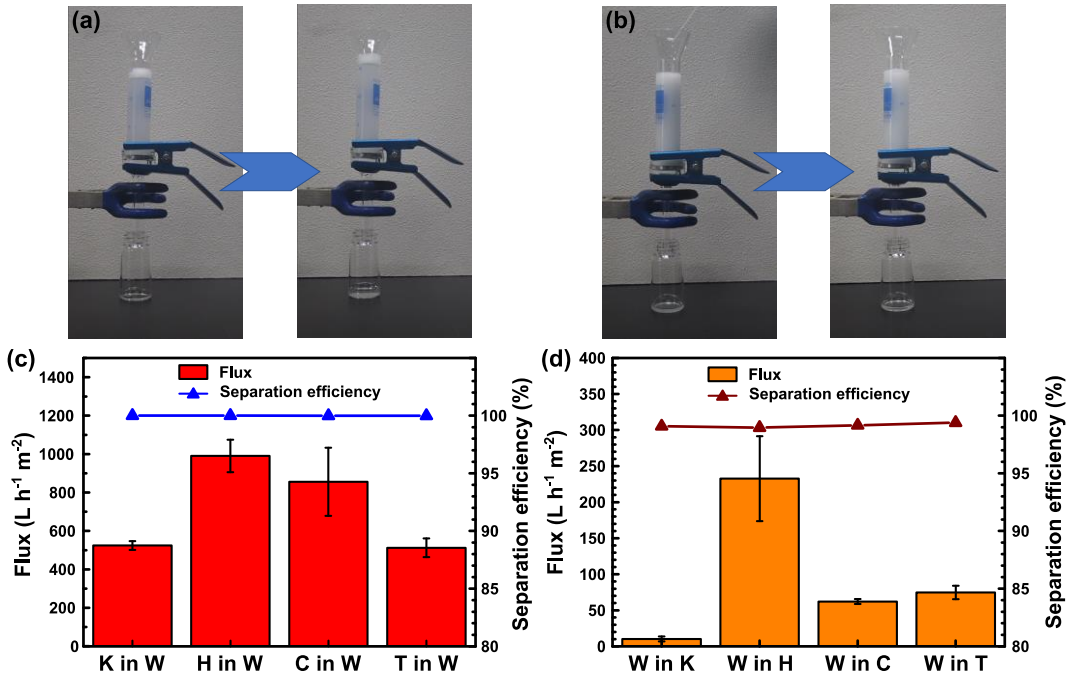

Figura 6. Il setup per la separazione di emulsioni (a) olio-in-acqua e (b) acqua-in-olio è mostrato dalle foto qui riportate. I valori di flusso e di efficienza di separazione per le emulsioni di (c) olio-in-acqua e di (d) acqua-in-olio sono rappresentati tramite questi grafici.

La membrana r-PET@Chit2 è stata anche testata per valutarne la capacità di purificare anche emulsioni stabilizzate di oli in acqua e viceversa. Per prima cosa, tramite un'analisi DLS, sono state valutate le dimensioni delle particelle del liquido disperso nelle emulsioni utilizzate. Come mostrato in Fig. 5.13 dalle immagini digitali, le emulsioni di partenza mostrano un aspetto lattiginoso, mentre il liquido risultate dalla filtrazione appare trasparente, suggerendo così che il processo di separazione sia avvenuto con successo. Le immagini al microscopio ottico (Fig. 5.13) confermano questi risultati, mostrando la presenza di piccole goccioline disperse all'interno del liquido di partenza, che poi non vengono più rilevate successivamente nel prodotto filtrato. Infine, l'analisi DLS (Fig. 5.13) non mostra alcun segnale sul campione di liquido filtrato, il che può essere dovuto ad una concentrazione di fase dispersa inferiore alla sensibilità dello strumento. Infatti, dalle analisi di cromatografia a gas e del Karl Fisher, sono state misurate concentrazioni rispettivamente di olio in acqua e di acqua in olio più basse di 104 ppm. Le efficienze di separazione quindi calcolate tramite l'Equazione 4 risultano essere > 99% per tutti i diversi tipi di emulsioni testate (Figura 6c e d). I valori di flusso misurati variano fra i 512 e i 991 L h^{-1} m^{-2} per le emulsioni di olio in acqua e fra 10 e 233 L h^{-1} m^{-2} per quelle dell'acqua dispersa negli oli (Figura 6c e d). La differenza fra i flussi dei vari oli attraverso la membrana (nel caso delle emulsioni di acqua negli altri solventi) è probabilmente dovuta alla differenza nella viscosità dei liquidi utilizzati. Infatti, l'esano è il solvente con la viscosità più bassa, per cui risulta essere anche il fluido con un flusso maggiore, mentre il kerosene, che ha una viscosità di circa sei volte superiore all'esano, incontra una resistenza maggiore nello scorrimento attraverso le porosità del filtro (Table 5.7). Rispetto ad altre membrane per la separazione controllata di emulsioni di solventi immiscibili (Table 5.6), il filtro qui progettato presenta valori di flusso relativamente bassi, mentre le efficienze di separazione ottenute possono considerarsi fra le più alte. In questo caso, il vantaggio principale della soluzione qui descritta può essere identificato nella scelta di materiali sostenibili a livello ambientale che permettano di ottenere ottimi risultati sia nella separazione di semplici miscele che nel caso di emulsioni stabili di olio e acqua.

Conclusioni

Per concludere, in questo lavoro è stata realizzata con successo una membrana sostenibile e a basso costo per il filtraggio controllato di miscele ed emulsioni di acqua e oli. Le fibre di PET riciclato funzionalizzato con il chitosano e prodotte tramite elettrofilatura hanno mostrato proprietà anfifiliche, essenziali per controllare il tipo di liquido filtrato pre-bagnando la membrana del filtro. Il presente studio ha dimostrato la possibilità di controllare la morfologia, la composizione chimica e le proprietà di bagnabilità modificando la concentrazione di chitosano nella soluzione di partenza. I filtri così progettati hanno mostrato alti valori di efficienza di separazione e di pressione di intrusione, a cui sono però associate velocità di processo di separazione relativamente basse.

Acknowledgments

First of all, I would like to thank all those people without whose precious help this work would not have been possible. Thanks to Professor Kenji Kinashi, for his constant support in providing all the necessary equipment to complete the research and for the valuable advice given to me along the way. Thanks to Professor Naoto Tsutsumi and Professor Wataru Sakai, for hosting me in their laboratories this year and always making me feel welcome. Thank you to Professor Sangermano for following me and helping me from afar. I would also like to thank Professor Sono Sasaki very much for allowing me to use the equipment for the contact angle analysis any time I needed it. Thanks to Professor Yasuro Fuse for the precious help with the gas chromatography analysis and to the Kyoto Electronics Manufacturing Co. (Kyoto) for providing the Karl Fisher instrumentation. A special thanks goes to Hoan and Phu, for all the support they have given me since the beginning, and for having taught me a lot of fundamental things related to the world of research and not only. Finally, I would like to thank all of my laboratory mates, which kindly welcomed me to the university and in Japan.

Abstract

The preservation of marine ecosystems from human activity is one of the most severe challenges of our days. In particular, the oil/water separation from oil spills and oily wastewater is particularly important. For this reason, a low-cost, effective, and sustainable solution is highly demanded. In this work, a controlled-wettability membrane for selective oil-water mixtures and emulsions was developed. The nanofibrous membrane was prepared via the facile and cost-effective electrospinning technique, using environmentally sustainable materials such as recycled polyethylene terephthalate (r-PET) and chitosan. The effect of different concentrations of chitosan on the morphology, chemical composition, mechanical properties, wettability, and separation performance of the membrane was evaluated. The membranes exhibited an underoil superhydrophobic and underwater superoleophobic behavior, which is essential to perform the selective separation. In fact, the designed filter was found to have a really competitive anti-fouling property and high efficiency (> 95%) in heavy- and light-oil/water separation both for emulsion and immiscible mixtures.

Index

Index of figures

Index of Table

1 Introduction

1.1 Aim of the study

Although there are many pieces of evidence regarding the use of petroleum since ancient times [48, 49], it is common to consider the beginning of the modern history of the *black gold* in the 19th century with the first byproducts distilled by the row material. In a few decades, petroleum became the fundamental resource of energy that contributed crucially to the second industrial revolution. In addition, from 1907 – when the bakelite was synthesized for the first time [50] – onwards, petroleum became increasingly more important also for the production of polymeric materials, which, today, represent a fundamental class of materials many different applications.

The growth of this new market also implied negative externalities, among which the environmental impact represents undoubtedly one of the most evident [51–53]. In particular, the oil spill in oceans is still considered a problem in our days [1, 2, 54–56]. The big spills that occurred in ship accidents – which commonly attract media attention mostly – certainly have an essential contribution to ocean pollution, but the phenomenon is more significant than this. In fact, most spills occur daily with small amounts from different sources such as regular shipping operations, municipal and industrial effluents, and oil rig operation [3, 4, 57, 58], and it is crucial to detect and manage them. Because of the difficulty in control every source of oil, in addition to a different method to collect data or lack of data itself, it is not easy to calculate the real amount of petrol spills worldwide. Still, it was estimated that around 5.86 Mtons oil entered the marine environment since 1970 form the tanker incidents that released more than 7 tons of oil [59].

Therefore, it is essential to develop effective methods to reduce, contain, and collect released oil. Over the years, various solutions have been developed, such as API oil-water separators [5], centrifugal separation [6], hydrocyclones [7], and so on [8]. All these techniques require time and a large amount of energy to be used; for this reason, in the last few years, many studies focused on developing different types of membranes that allow the enhancement of mechanical filtration of water-in-oil and oil-in-water emulsions [9–15]. Among these, the fibrous mats made by electrospinning represent an attractive alternative thanks to their high flexibility and high separation performances [16–18]. These membranes for the oil-water separation are realized using many different polymers, such as polysulfone [19], polyimide [20], polystyrene [21], polyvinylidene fluoride [22], and polyurethane [23]. In order to respond to the increasing demand for sustainable and cost-effective methods to produce fibrous membranes, some studies have explored the use of waste polymers to achieve the oil-water separation. For example, W. Liu et al. have designed an electrospun membrane for the separation of oil-water mixtures and emulsions by coating a stainless mesh using the waste cigarette filters as raw material [24]. Waste polystyrene (PS) was also used by P. Sow et al. to fabricate via blow spinning superoleophilic fiber-coated membranes for oil recovery, which showed separation efficiency up to 97% [25].

Electrospinning is a straightforward, cheap, and easy controlled process, and for these reasons is one of the most used techniques to realize polymeric nanofibers [60]. It consists of a pump connected with a syringe that feeds the flow of the polymer solution through a needle. An electric field is applied between the needle and the collector. So, the liquid droplets are deformed into a cone-shape and accelerated to the target. During the path, the solvent evaporates, and the solid fiber is formed. In this scenario, many parameters can affect final morphology: applied voltage, tip to collector distance, solution flow rate, solution conductivity, solution viscosity, solvent volatility, humidity, and temperature [61, 62].

Polyethylene terephthalate (PET) is a low-cost, thermoplastic polyester, widely used in packaging, automotive, electrical, electronic, and, in particular, in the textile industry [26], which represents the primary PET market [27]. Its increasing use, especially for bottles, has made end-of-life management a more and more crucial issue, and, over the years, many different solutions have been developed to manage the waste PET [28] and, in some cases, reuse the recycled material [29–31]. However, the recycled PET (r-PET) bottles are usually adopted to fabricate low-cost products, so that the profits involved in its market are relatively low. Using the

r-PET as a base to make fibrous membranes for the oil-water separation could result in a reduction of the cost of that resource respect to the virgin materials and also in environmental benefits. The increase in the added-value of r-PET products, in fact, can encourage its collection and recycling and reduce the amount of released plastic in the environment. Some studies have already been conducted on the use of r-PET in fibrous filters. N. Zander and her group have successfully develop recycled PET nanofibers for the filtration of particles from 30 to 2000 nm dispersed in water [32]. In another work, the oil-water separation performance of functionalized r-PET has also been tested, reaching separation efficiencies higher than 98.5% [33].

Recently, smart nanofibrous membranes were fabricated to control the oil-water separation process. Smart materials that can respond to temperature [34], pH [35], UV light [36], ion [37], electric field [14], and prewetting [10, 38], are considered as an emerging candidate for on-demand oil-water separation. Among them, prewetting is the most potential approach because of their facile fabrication and operation. The membrane used for the prewetting process should exhibit amphiphilic property, while underwater superoleophobic and underoil superhydrophobic. When the membrane was prewetted with the oil, the membrane allows oil to pass through while they prevent the water from penetrating. In contrast, while the membrane was wetted by water, it will enable the water to go through the membrane while keeping the oil above the membrane.

According to previous studies [33], the r-PET nanofibrous membrane exhibited hydrophobicity and oleophilicity. Therefore, a modification is required to obtain an amphiphilic membrane from r-PET. A simple and sustainable approach is modifying the r-PET with chitosan, a hydrophilic and biodegradable polymer. The nanofibrous membrane fabricated from the blend of r-PET and chitosan is expected to show the amphiphilic properties due to the presence of hydrophobic groups of r-PET and hydrophilic groups of chitosan. By prewetting the membrane with oil or water, the oil-water separation could be controlled. A schematic representation of the overview of this study is provided below in **Errore. L'origine riferimento non è stata t rovata.**.

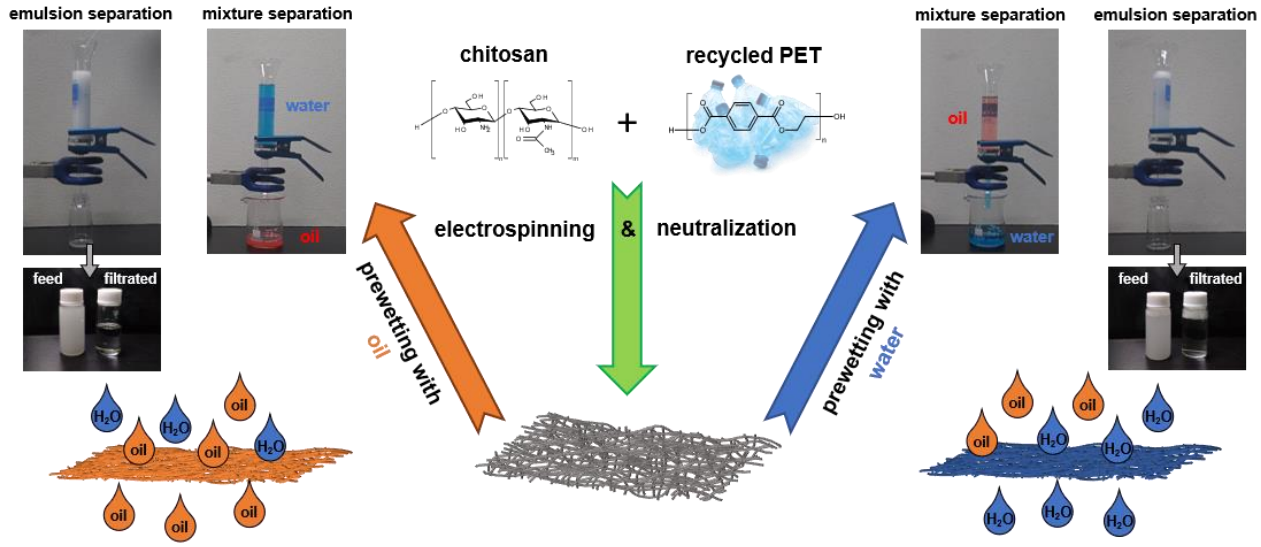

Fig. 1.1. Schematic representation of the overview of this study. Chitosan and r-PET were used to realize a membrane for oil water separation. By prewetting this membrane with different type of liquid the separation of water from oil or oil from water can be performed

1.2 Oil spill treatments

This section presents an overview of the actions that are commonly adopted to prevent and contain the oil spread in the marine environment. This brief review is useful to better understand the context of the polluted water treatments and contextualize the application of the object of this research: the oil-water separation membranes. The leading solutions can be divided into spread containment, mechanical removal, use of sorbent devices, chemical treatment, and in-situ burning.

1.2.1 Containment

The first significant action that is usually carried out after a petrol leakage is the containment of the diffusion of the spilled oil thanks to the use of containment booms. There are many different types of oil blooms, but, basically, they are constituted by floats along the central line, which guarantee to maintain the upper part of the object above the sea level, a freeboard member above the water, which prevents oil from washing over of the top of the boom, and the skirt, useful to contain the oil below the sea level. Many complications – usually related to natural forces like wind, water currents, and waves – can occur during the restrain, and they can even lead to boom failures [63–65]. An evolution of containment booms is represented by the sorbent booms, which are typically used in the case of thin slick to contain the spreading and absorb the oil, separating it from the water [66].

1.2.2 Mechanical removal

After the containment, the following operation is the better separation of oil and water as possible. Several types of skimmers can perform this task:

- **Oleophilic skimmers**: they are made up of oleophilic surfaces to which oil adheres; these components are set in motion by mechanical parts that allow the collection of oil in containers [67].
- **Weir skimmers**: they are big tanks with the edge on the water level, so that, thanks to gravity, the floating oil drop inside the container. The oil is then pumped outside the tub and stored. As is expected, this kind of machine is used most in calm water and for lighter oils [67].
- **Vacuum skimmers**: a vacuum pump is used to suck oil from the water surface, usually using an enlarged and floating head. This one is the cheapest type of skimmers, although it occurs in failure in choppy water and the presence of debris [67].
- **Elevating skimmers**: a conveyor belt equipped with paddles is placed on the oil/water interface and moves the oil to a collection tank. It is useful machinery in calm water and with middle to fairly heavy oils [67].
- **Submersion skimmers**: a belt or an inclined plane forces a downward flux of shallow water, together with the floating oil, to a well; oil is then separated from the plane by gravity o a scraper and finally aspired by a pump and stored. This kind of skimmers is typically used in the case of large spills of light and low viscosity oils [67].

1.2.3 Sorbents

Natural [68–71] or synthetic [72–74] materials can be used to adsorb or absorb dispersed oil and contribute to oil/water separation. Typically, sorbents cannot be used as primary recovery systems in big spills because of their reduced capacity. Otherwise, they are used to collect the final traces of oil, in sorbents booms, as passive systems of cleanup, or as the primary system in small spills. Recyclability, sorption capacity, and sorption rate are key factors to evaluate the effectiveness of the used sorbent. These materials are available in different forms (granules, powder, fibrous membranes, rolls, etc.) and with varying surfaces to can adapt better to the specific type of oil they are projected to collect.

1.2.4 Chemical response

Different types of chemical products can be used to reduce the spill's environmental impact. *Dispersants* are basically surfactants that are used to disperse small oil drops into the water; the use of these chemicals is often limited by regulations [75], but in some cases, their use is necessary [76]. *Surface-washing agents* are chemically similar to dispersants, but they are more effective when used to release the oil from the surface thanks to their cleansing effect [77]. Instead, *emulsion breakers* are used to prevent water-in-oil emulsion, which can adversely affect oil collection by increasing the volume of recovered material and its viscosity to such an extent as to make skimmers and pump ineffective [78]. *Solidifiers* are cross-linkers which promote oil phase transaction from liquid to solid state so that it is easier to collect oil using mechanical means [79].

Finally, *biodegradation agents* enhance biodegradation of oil by exploiting native species like bacteria and fungi that degrade some components of fuel; this solution is mostly adopted on land or shorelines because in open sea occurs high dissolution of chemicals and the oil moves rapidly [80].

1.2.5 In-situ burning

The oldest technique used in oil spills consists of burning the slick to consume most of the fluid. Basically, oil vaporization provides fuel for burning, and its rate controls all the processes. So, it is fundamental to reach a steady-state to avoid fire consumption or fuel loss, and for this purpose are crucial both weather conditions [81] and slick thickness [82]. In particular, to control the thickness – but also fire extinction –, fireproof booms are used. Usually, booms are anchored to tows, which can move upwind to concentrate oil and increase the slick thickness (in case the fire was going out) or release one end of the boom to spread oil and switch off the flame [83]. Principal advantages of this technique are the rapid removal of large amounts of fuel with high efficiency (usually more than 90%), a small quantity of disposed of oil, only cleanup option in some cases, and little labor and equipment required compared with the other alternatives. In contrast, in-situ burning generates big black smoke and toxic emissions (particulate matter, polyaromatic hydrocarbons, volatile organic compounds, dioxins and dibenzofurans, carbonyls, and so on [84, 85]). Besides, some other disadvantages must be considered as the necessity of oil containment, the difficulty in the ignition, and the risk of flame spreading due to other combustible material [85].

1.3 Water-oil separation

After the oil has been collected, it has to be separated from water and debris. In the following part, some of the most commonly used techniques are presented and briefly described. In **Errore. L'origine riferimento n on è stata trovata.**, for instance, some of these techniques are reported together with the minimum size of the oil droplet that they can successfully separate. The same methods shown below can also be used in treating industrial wastewater, which also contributes significantly to the pollution of oil in seawater.

1.3.1 Gravity separator

Liquids with different densities, collected in a big tank, tend to separate after a time called *residence time*. The driving force of the process is gravity, and it is possible to predict the rate of the lighter liquid bubbles using Stokes's law [5]:

$$v = \frac{gD^2(\delta_\omega - \delta_0)}{18\mu} \tag{1.1}$$

v = rate of rising of an oil globule
g = gravity acceleration
D = diameter of a globule
δ_ω, δ_0 = density of water and oil respectively
μ = absolute viscosity of the aqueous phase

It is clear that this system is the more effective, the higher the difference in density between the two liquids. API oil/water separator is the basic model of gravity separator. Still, other configurations are also possible: circular separator, plate separator, Shell parallel-plate interceptor (PPI) separator, Shell corrugated-plate interceptor (CPI) separator, and curved-plate finger separator [86]. Baffles or similar devices allow to decrease residence time and increase the degree of separation [87]. Unfortunately, despite all these enhancements, gravity separators cannot be used to separate emulsions, dissolved oil, and oil coating solids; in these cases, chemicals should be applied. Gravity separators can be considered a good solution because of their low cost, low power consumption, high flow rate, and little labor required. However, operational time is long, and big spaces are needed.

Table 1.1. The minimum size of oil particles that can be removed by each removal technology takes into account [88]

Oil removal technology	The minimum size of particles removed (µm)
API gravity separator	150
Corrugated plate separator	40
Induced gas flotation (no flocculant)	25
Induced gas flotation (with flocculants)	2-5
Hydrocyclone	10-15
Mesh coalesce	5
Media filter	5
Centrifuge	2
Membrane filter	0.01

1.3.2 Rotational separator

Compared to the previous method, rotational separator uses centrifugal force to carry out the separation. Stokes's law is still valid to describe the ascent rate, but centrifugal force can be 1000 or 5000 times higher than gravity one. This fact makes it possible to remove efficiently oil- and non-oil-coated suspended solids, free oil, and primary dispersion with globule size greater than a critical size [86]. Rotational separation turns out to be economical and practical only with high concentrations of oil and solid residuals, however ineffective with stable emulsions and solubilized and dissolved oil. Two different types of separators were developed:

- **Centrifugal separator**: the liquid mixture flows into a chamber, where a spinning rotor forces a rotational motion. Because of the difference in density of the liquids, centrifugal force leads to phase separation so that a higher dense phase moves toward the outer part of the flow and can be collected separately. As expected, the higher the difference in densities of the two phases, the faster the separation and the less the energy requirement (at least 5%) [86]. This type of configuration results in more efficient respect to gravity separators, having shorter residence time and high volumetric throughput, but it does not reveal suitable in the presence of big debris [89, 90].
- **Hydrocyclones**: the principle of separation is similar to the one just described, but, compared to centrifugal machines, hydrocyclones have no moving parts. Two parts compose the structure of the instrument: the liquid mixture is injected through the upper cylindrical part in a tangential direction to develop a steady swirling motion. Liquids with a higher density are forced against the walls and fall through the conical part of the machine. Instead, the lighter fluids follow an inner spiral flow, which moves upwards. Short residence time, small separated droplet size, high centrifugal forces, relatively small machine size, low cost, and seldom need to chemicals make hydrocyclones very competitive compared to other solutions [91].

1.3.3 Gas flotation

The working principle is very similar to the gravity separation, but in this case, gas bubbles are used to enhance the ascent rate of the oil. In fact, after stable bubbles were generated, collisions between them and the oil droplets cause a strong adhesion between the two media. This complex rises quickly to the surface so that it is possible to remove the oil by skimming [92]. The low that governs this phenomenon is still Stokes's low, being careful of considering density and diameter of oil-air agglomerates. Depending on how the air bubbles are provided, it is possible to distinguish from dispersed air, dissolved air, electrochemical, and vacuum devices [86].

1.3.4 Sand filtration

An alternative of flotation is represented by sand or multimedia filtration [93]. It consists of the use of sand, crushed anthracite coal, perlite, diatomaceous earth, garnet sand, or granular carbon to remove oil. Usually, the filter media thickness varies from 0.35 to 1.0 mm [86], and typically they can remove oil particles down to 2-5 μm [94]. In multimedia filtration, at least two different materials are used, and, by the control of the density and the size of the grains, it is possible to obtain a distribution that consists of light and coarse material at the top and the fine part at the bottom. The main advantage, in this case, is the pressure-drop reduction at high flow rates [86].

1.3.5 Filtration-Coalescence

This process was initially developed to remove the water from the oil, but successively it was also introduced in the water purification treatments [95]. It involves porous media – usually fibrous membranes [95–97] – which favors the dispersed oil droplet to coalesce so that, reached a specific dimension, they flow over the filter and can be removed more easily, for example by gravity separation. Although the coalescence phenomenon is not entirely understood, some theories have been developed to explain the mechanism [86]. Basically, the main steps that provide to the coalescence of the oil (or the water) drop involved the collision of the droplets with the filter surface and the consequent adhesion to that. After that, other globules reach the previous one, collide and collapse. The coalesced drops, ones they have reached the right dimension, migrate though the dept of the media and continue to grow. Finally, when the drops are mature enough, they are released by the filter and separate from the water by gravitational separation [98].

1.3.6 Membrane separation

The membrane separation is a simple, efficient, and low-cost solution that exploits microporous sheets to complete selective physical separation of the oil or the water in oil-water mixtures [99, 100]. A pressure gradient drives this process, and it is generally classified into microfiltration, ultrafiltration, and reverse osmosis based on the dimension of the pore of the membrane [101]. The high selectivity of the separation membranes is usually achieved by controlling the wettability of the layer. In fact, this surface property controls the affinity of the material that composes the membrane with a specific liquid and can define the functionality of the product: in order to design a device which retains the oil and lets water to flow, it is necessary to confer superhydrophilicity and superoleophobicity properties to the membrane, while obtaining superoleophilicity and superhydrophobicity it is possible to separate the water from the oil [102]. The main advantages of this technique are the high efficiency of the separation performance, the high level of automation, no use of chemicals, a low energy input, a small footprint, and the possibility to design membrane which also has the capacity to reject other pollutants contained into the feed [99].

Many different materials can be used to fabricate this kind of membranes, and they can be basically divided into three big groups: metal meshes functionalized by a wide range of inorganic or organic materials, fabric-based material, and electrospun nanofibers. Gupta and his group [102] elaborated a good review on the recent progress of the filtration and adsorption methods for the oil/water separation, which comprehends many examples of differently designed membranes. Furthermore, one of the most recent overview about the fibrous polymer membranes – both by electrospinning and solution casting on metal meshes – and their alternatives have been published this year by El-Samak and co-workers [103].

2 Fundamentals of liquid separation

In this chapter, the principle phenomena related to membrane separation are explained. In particular, the basics of the contact angle theories are presented, both for substrates in-air or immersed into a liquid. Furthermore, it is shown how the presence of the irregularities on the sample surface, especially the morphological one, can affect the contact angle. Finally, the correlation between the contact angle and the filtration performance of a fibrous membrane is investigated.

2.1 Wettability

Wettability is an important property of solid surfaces, which gives information about the intermolecular interactions between liquids and solids at their interface. As presented below, these interactions play a crucial role in the separation process. Here the basics of the wettability properties are summarized.

2.1.1 Contact angle in air

The separation performances of a membrane are closely related to the surface interactions between the filtred liquid and the surface. One of the most common measurements that give some information about these interactions is the contact angle (CA). The Young's equation [104] is the well-known relation that describes how the changing in the surface properties can affect the CA, defined as the angle between a smooth surface and the tangent to the drop of liquid at the point where it touches the surface on which it rests (Fig. 2.1a). It can be written as:

$$\cos\theta = \frac{\gamma_{SV} - \gamma_{SL}}{\gamma_{LV}} \tag{2.1}$$

where θ is the contact angle, and γ_{SV}, γ_{SL}, and γ_{LV} are respectively the interfacial tension of the solid-vapor, solid-liquid, and liquid-vapor interfaces. In case of water, for example, if $\theta < 90°$ the surface is classified as *hydrophilic*, while when $\theta > 90°$ it is defined *hydrophobic*.

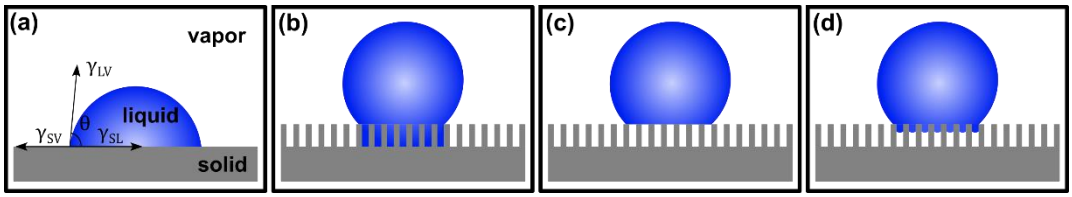

Fig. 2.1. Representation of a drop of a generic liquid in-air on (a) a smooth surface, a rough surface following (b) the Wenzel model, (c) the Cassie-Baxter model, and (d) a unification of the previous two models.

Moreover, when the contact angle of the droplet on the surface is equal to 0°, the surface is classified as *superhydrophilic*, while when $\theta > 150°$, the surface is called *superhydrophobic* [105]. In order to obtain the last-mentioned state, it is necessary to introduce roughness on the substrate. In this case, the Young equation is not more useful to describe the system [106], so the wetting behavior is commonly described by the Wenzel and the Cassie-Baxter theories [107, 108]. The first one is based on the assumption that the liquid flows into the rough structure filling them (Fig. 2.1b). It results in a modification in the CA, which can be calculated by the Wenzel equation:

$$\cos\theta_w^* = r\cos\theta \tag{2.2}$$

where θ_w^* is the apparent contact angle at the stable equilibrium state, and r the roughness factor, equal to the ratio between the real surface area and a completely smooth one. It is easy to understand that r is always bigger than 1. For this reason, the increase in the surface rugosity leads to an amplification of the wettability of the

surface. When $r \gg 1$, it is possible to obtain the extreme condition of superwettability ($\theta > 150°$ and $\theta \sim 0°$) [109].

However, in the case of heterogeneous surfaces, the Wenzel equation cannot correctly describe the apparent CA, so the Cassie-Baxter model is introduced. In this case, some air is trapped through the interstices of the support by the liquid droplet deposited over them (Fig. 2.1c). So, the liquid-solid interface is reduced and substituted by the air-liquid one, which favors the liquid repulsion. The contact angle is measurable by the following equation:

$$\cos\theta^*_{CB} = \varphi_s \cos\theta + \varphi_s - 1 \tag{2.3}$$

where θ^*_{CB} is the apparent contact angle of the surface, and φ_s is the fraction of the solid-liquid interface. In the real samples, however, there is not a clear separation between the Wenzel and the Cassie model, but it is common to observe a transitional state between the two situations [105] (Fig. 2.1d).

2.1.2 Contact angle in water or oil

Similar considerations can also be done to define the contact angle of one liquid (for example, water, W) in the case of a sample immersed in a different liquid (for example, oil, O). For a smooth surface, an oil/water/solid interface is formed (Fig. 2.2a), so that the underoil water contact angle (θ_{OW}) is defined by the modified Young equation:

$$\cos\theta_{OW} = \frac{\gamma_{SO} - \gamma_{SW}}{\gamma_{OW}} \tag{2.4}$$

where γ_{SO}, γ_{SW}, and γ_{OW} are the surface tension at solid-oil, solid-water, and oil-water interface. Furthermore, γ_{SO} and γ_{SW} can also be calculated using the Young equation for water and oil in the air. In particular, it is easy to derive from Equation 2.1 the following definitions:

$$\gamma_{SW} = \gamma_{SA} - \gamma_{WA}\cos\theta_W \tag{2.5}$$

$$\gamma_{SO} = \gamma_{SA} - \gamma_{OA}\cos\theta_O \tag{2.6}$$

θ_W and θ_O represent the water and the oil contact angles in-air respectively, while γ_{SA}, γ_{WA}, and γ_{OA} are the interfacial tension at solid-air, water-air, and oil-air interface. So, introducing Equation 2.5 and 2.6 in Equation 2.4, it possible to obtain:

$$\cos\theta_{OW} = \frac{\gamma_{WA}\cos\theta_W - \gamma_{OA}\cos\theta_O}{\gamma_{OW}} \tag{2.7}$$

A similar equation is available also in case of underwater oil contact angle (θ_{WO}), basically changing the sign at the numerator. So, in the more straightforward case, it is possible to distinguish between two opposite configurations: if the sample is in-air hydrophilic, it turns out that $\gamma_{WA}\cos\theta_W > \gamma_{OA}\cos\theta_O$ and consequently

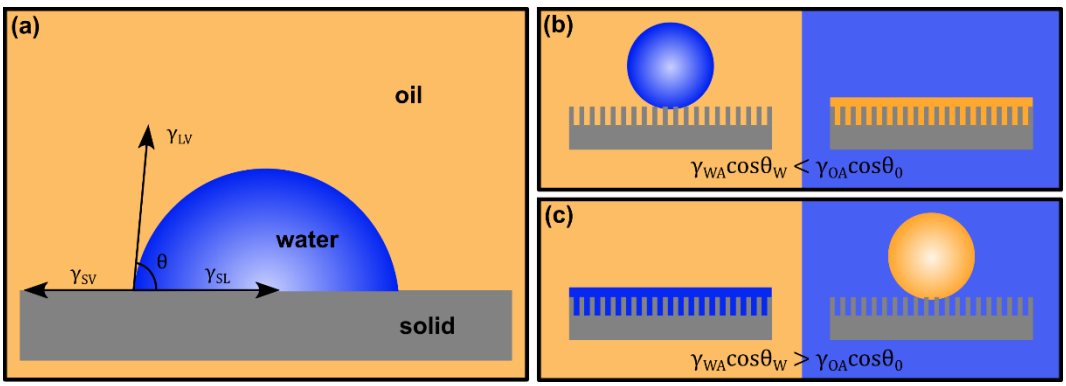

Fig. 2.2. (a) Schematic representation of the underoil water contact angle for a smooth surface. (b) Underoil superhydrophobic and underwater superoleophilic sample. (c) Underoil superhydrophilic and underwater superoleophobic sample.

$\cos\theta_{OW} > 0$ and $\cos\theta_{WO} < 0$, which means underwater superoleophobicity and underoil superhydrophilicity (Fig. 2.2c). On the other hand, if the solid is in-air oleophilic, $\gamma_{WA}\cos\theta_W < \gamma_{OA}\cos\theta_O$, and consequently, the surface is considered underoil superhydrophobic and underwater superoleophilic (Fig. 2.2b).

In the case of rough membranes immersed in a liquid, the Cassie-Baxter equation is also valid [106]:

$$\cos\theta_{OW}^{CB} = \varphi_s \cos\theta_{OW} + \varphi_s - 1 \tag{2.8}$$

In this study, an amphiphilic membrane has been designed, which means that it exhibits both superhydro- and superoleophilicity. In this situation, the wettability is influenced differently by the immersion in one liquid. It has been reported that usually, this kind of substrates display underwater superoleophobicity and underoil superhydrophobicity [9, 10, 14, 38]. In fact, the liquid in which the sample is immersed completely enter the microstructure of the membrane and stick to it. Consequently, when another fluid is deposited on the surface, it forms an interface with the attached liquid and not with the solid, resulting in a strong repulsion [9] (Fig. 2.3)

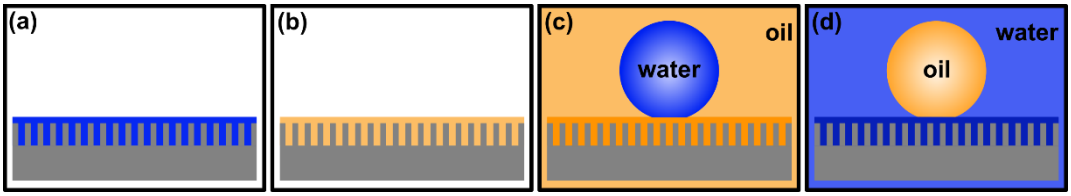

Fig. 2.3. Schematic representation of (a) the water, (b) the oil, (c) the underoil water, and (d) the underwater oil contact angles in case of an amphiphilic membrane.

2.2 Separation mechanisms

One of the main drawbacks of the oil-water membrane separation is considered the easy failure of the device [99, 102]. Usually, the retained liquid accumulates on the filter surface and increase the pressure that pushes on the membrane. When this pressure overcome a specific limit, the liquid is free to go through the porosity, resulting in a sudden drop in the separation efficiency.

To better understand this phenomenon, it is important to apply some of the notions described above. Considering a fibrous membrane, when it is immersed in a fluid with a good affinity (e.g., oil), the fibers are surrounded by the liquid [9]. If a drop of a different liquid (e.g., water) is deposited on this system, a configuration similar to the one reported in Fig. 2.4a is formed. Thus, an equilibrium of forces is established: the vertical component of the force related to the surface tension opposes the pressure applied by the column of water. Assuming A as the pore area and L as the pore circumference, it is possible to define the force applied by the overlying liquid as:

$$F_P = \rho\, g\, h\, A \tag{2.9}$$

where ρ is the density on the liquid, g is the acceleration of gravity, h is the high of the oil column, and A is the area of the pore. On the other hand, the surface tension at the liquid-liquid interface develop a force F_γ, which has a vertical component equal to:

$$F_\gamma^\perp = L\,\gamma_{OW}\cos\alpha \tag{2.10}$$

where α is the angle between the interfacial force and its vertical component, and it easy to understand form Fig. 2.4a that $\alpha = 180 - \theta_{OW}$. Equalizing Equation 2.9 and 2.10 is so possible to calculate the maximum high that the water column can reach before the applied pressure pushes the liquid through the pore [110–112]:

$$h = -\frac{l\,\gamma_{OW}\cos\theta_{OW}}{\rho\, g\, A} \tag{2.11}$$

From this relation, it appears clear that the underoil water CA influences a lot the performances of the membrane. The higher the angle, the bigger is the pressure that the filter can support before the failure

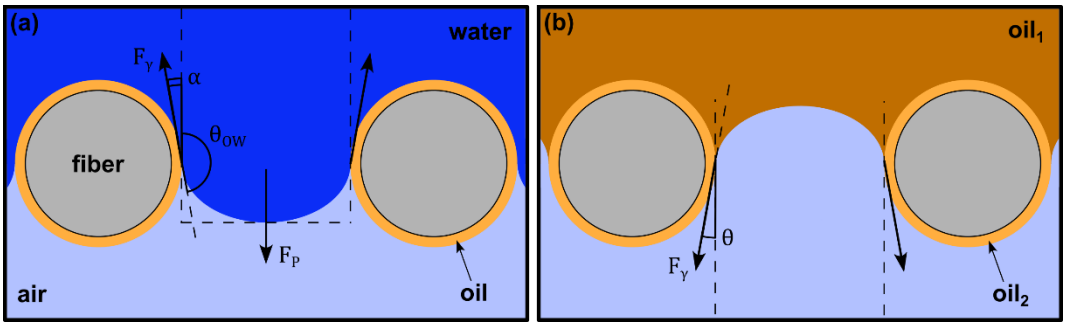

Fig. 2.4. (a) Schematic representation of the section of a superoleophilic fibrous membrane for water-oil separation during the underoil water. (b) When a different type of oil is used the liquid-liquid affinity is greater, so the CA is < 90° and the oil is not retained.

Furthermore, from Fig. 2.4b, it is possible to understand that when the underoil contact angle is smaller than 90°, the membrane cannot retain the liquid. In fact, in this case, the interfacial force drives, together with the fluid pressure, trough the pores, instead of opposes. This different behavior in retaining different types of liquid is at the base of the mechanism that allows to separate the water and the oil. In fact, when the membrane is prewetted by the oil, the system forms with the water a positive intrusion pressure, so that the liquid is retained if a high pressure is not exerted. On the other hand, the same apparatus develops a contact angle smaller than 90° with oils, so that this type of liquid is free to go through the pores. If the membrane is prewetted with the water, an opposite behavior is observed.

3 Electrospinning

Electrospinning is a widely used process to produce nano- and microscale fibers from solutions or melt. The electrostatic force plays a key role during the fabrication, stretching the fluid so that it forms a continuous and homogeneous filament.

3.1 Historical overview

The first studies about the influence of electrostatic force on liquids were carried out by William Gilbert in the 17th century. He observed that a rubbed amber, held close to a drop of water, can deform the shape of that droplet, attracting the liquid which forms a cone shape.
In the following centuries, many academics such as G.M. Bose (1745), G.B. Beccaria (1753), Lord Rayleigh (1879), Boys (1888) contributed with their studies to the understanding of electrostatic phenomenon applied to liquids [113]. In 1900 Cooley filed the first patent about an electrospinning apparatus [114], and over the years, he produced two others. His equipment did not provide the charge to the fluid by direct contact, but it used an external electric field generated between two pointed electrodes (Fig. 3.1). Cooley also presented four different types of indirectly charged spinnerets, with different characteristics each [115].

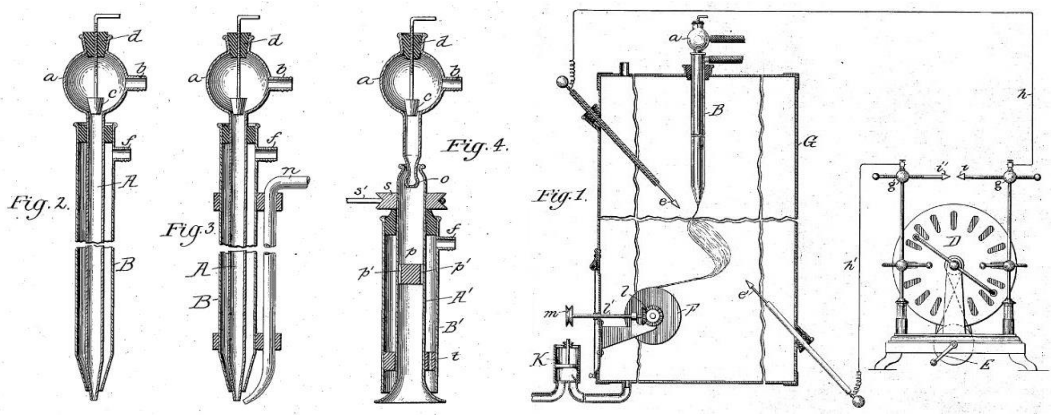

Fig. 3.1 Cooley electrospinning apparatus [114]

In a few years, more developments were carried out. For example, in 1902, William James Morton also issued a patent for his electrospinning machine [116]. Furthermore, between 1914 [117] and 1917 [118], John Zeleny conducted detailed studies on the effect of electric potential on the formation of the liquid meniscus at the conductor. He photographed for the first time the shape of the sprayed drop at the end of the capillary. An essential impulse to electrospinning development arrived from Anton Formhals' patents released between 1931 and 1944. In one of them [119], Formhals described a particular setup (Fig. 3.2) where an electric field was generated between a gear wheel and a metal ring; by rotating the wheel, it was possible to spin the solution from a receptacle to the ring forming fine fibers. This machine was completed by a washing device and a heater suitable for continuous production.
Between 1964 and 1969, Sir Geoffrey Ingram Taylor produced a series of studies on the mathematical modeling of the cone shape of the droplet that is formed during electrospinning [120]. Taylor's findings were so important that the characteristic drop shape is still called Taylor cone [113].
Despite all the progress made, electrospinning received significant attention both in academia and industry only from the 1990s when the renewed interest of the researchers and the development of nanotechnology and nanoscience gave the right impulse for the definitive consecration of this technique. D.H. Reneker and his group represent a great example of this renovated impulse thanks to their studies conducted between 1995-1996.

Nowadays, electrospinning is a popular method to produce fibers for many different applications such as filter [121–123], thermal insulation [124], sensors [125, 126], conductive devices [127–129], and biomedicals [130–132].

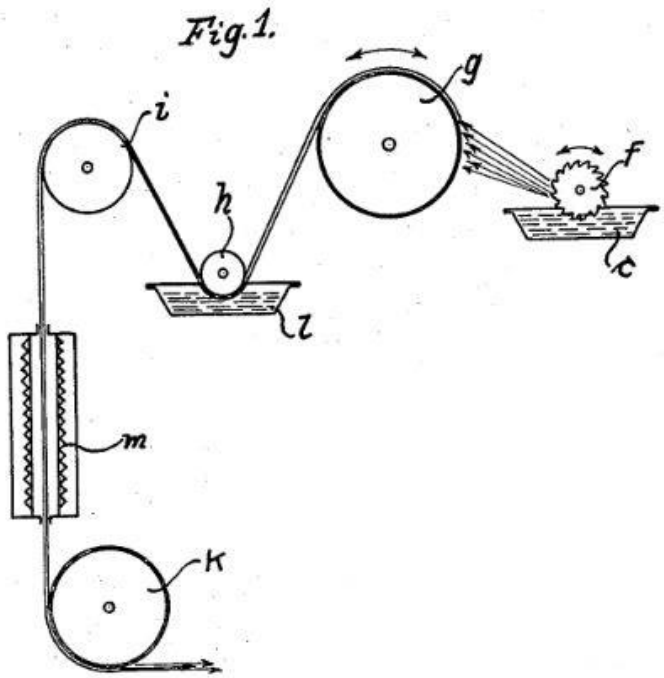

Fig. 3.2 Formhals electrospinning apparatus [119]

3.2 Process in detail

Usually, the electrospinning apparatus is composed by four fundamental elements: a syringe, for providing a constant flux of solvent, a needle, through which the solution or melt is ejected, a collector, that pick up the spun fibers, and a high voltage power supply, to generate an electric field between the needle and the collector (Fig. 3.3a). The high voltage applied generates static charges on the droplet of solution or melt at the needle tip, and the related electrostatic force produces the deformation of the initial spherical shape that elongates in the direction of the collector. In this way, the fluid acquires a conical shape properly named *Taylor cone* (Fig. 3.3b). When the electric field is strong enough, the electrostatic force overcomes the surface tension, and the fluid is ejected in the direction of the collector generating a filament. Along the path to the collector, the solvent evaporates – or the melt cools down – and a stable fiber is formed. During the ejection, the filament takes a particular trajectory schematically represented in Fig. 3.3c. In order to better understand the phenomena that control electrospinning, all aspects of this process will be analyzed in detail.

3.2.1 Excess charge formation

It is common to find in polymeric solutions ionic species like dissolved salts, solvent impurities, and residues of synthesis, which, together, contribute to determine the solution conductivity. When such a fluid is placed into an electric field, charged species migrate towards the opposite surfaces moved by electrostatic forces, and the solution consequently polarizes, generating some non-zero charged areas. Because of the low mobility of the ions (on the order of 10^{-6}-10^{-7} m^2 V s^{-1} []), their drift motion also results quite slow. Using the Stokes law, it is possible to estimate v_d, the velocity of ions motion:

$$v_d = \frac{qE}{\xi} = \frac{qE}{6\pi R\eta} \tag{3.1}$$

where ξ is the friction coefficient, R and q are respective the particle hydrodynamic radius and charge, η is the dynamic viscosity, and E is the electric field.

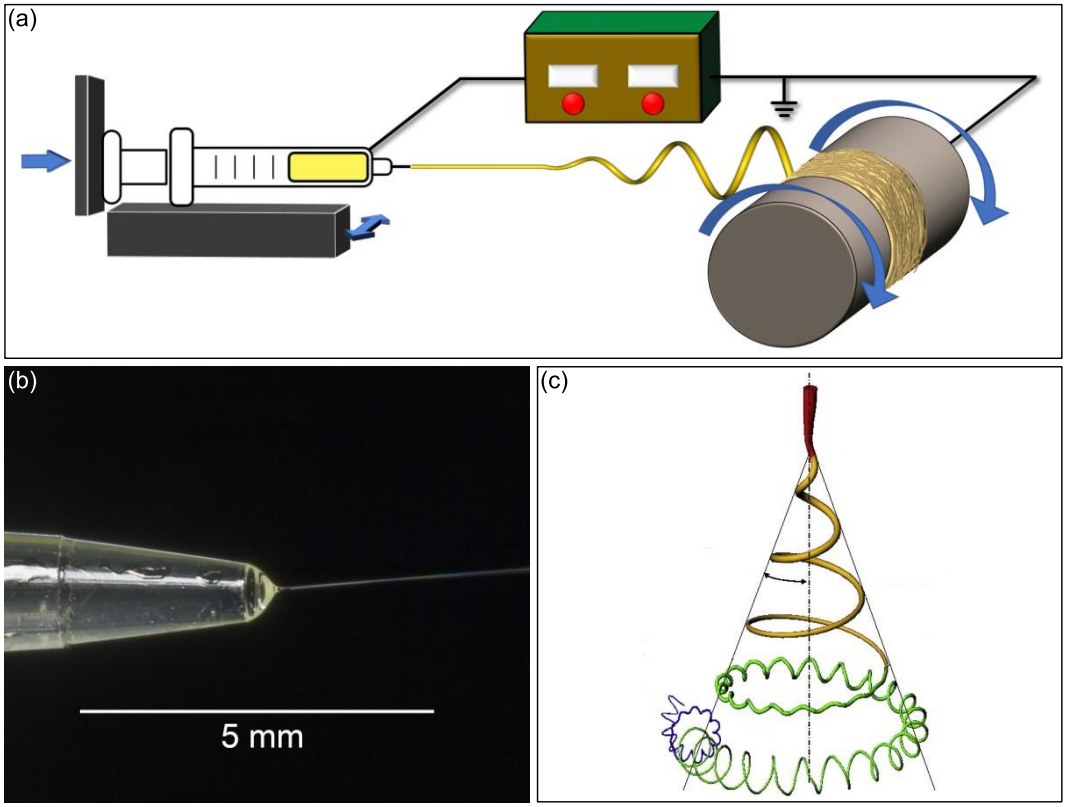

Fig. 3.3 (a) Schematic representation of an electrospinning device. (b) An image which shows the Taylor cone on the tip of a spinneret (Robert Lamberts - The New Zealand Institute for Plant and Food Research Ltd). (c) A schematic representation of the jet instabilities which can occur during the electrospinning process [189].

3.2.2 Jet formation

As already reported, two forces play a key role in jet formation during the electrospinning process: electrostatic force and surface tension [133]. By the use of the fundamental laws of electrostatic, it is easy to demonstrate that the electric field E on the surface of a sphere is:

$$E = \frac{1}{4\pi}\frac{4\pi R_T^2 \sigma_c}{\varepsilon_0 R_T^2} = \frac{\sigma_c}{\varepsilon_0} \tag{3.2}$$

R_T is the sphere radius, ε_0 is the dielectric constant, and σ_c is the surface charge density. So that it is possible to calculate the electrostatic pressure as:

$$p_e = \frac{\sigma_c^2}{2\varepsilon_0} = \frac{\varepsilon_0 E^2}{2} \tag{3.3}$$

The *Young-Laplace equation*, instead, can be used to calculate the pressure derived by the surface tension (the *Laplace pressure*). So:

$$p_l = \frac{2\gamma}{R_T} \tag{3.4}$$

where p_l is the *Laplace pressure*, and γ is the surface tension. Equaling the two forces, the threshold value of the electric field to have the generation of the liquid jet is calculated:

$$E = \left(\frac{4\gamma}{\varepsilon_0 R_T}\right)^{1/2} \tag{3.5}$$

Moreover, G.I. Taylor, in one of his works [134], calculated the expression to evaluate the critical value of potential (V_k) at which the jet formation occurs:

$$V_k^2 = 4\frac{H^2}{L^2}\left(\ln\left(\frac{2L}{R}\right) - 1.5\right)(1.3\pi R\gamma)(0.09) \tag{3.6}$$

where H is the distance between the needle and the collector, L the length of the liquid column, R is the outer needle radius, and 0.09 is a factor to express the voltage in kilovolts.
As it is written previously, as the applied electric field increases, the drop deforms gradually. G.I. Taylor has been the first who determined that, at the threshold point just before the jet formation, the droplet forms a cone shape with a semi-vertical angle of 49.3° [120]. Years after, Yarin et al. shown experimentally and theoretically that the inviscid, Newtonian, viscoelastic, and purely elastic fluids form a Taylor cone with a half angle of 33.5° [135].

3.2.3 Jet instability

Jet evolution plays a key role in the final morphology of the fibers. In particular, the influence of several instabilities that occurs during the path from the tip of the needle and the collector contributes to reducing the jet diameter of several orders of magnitude [133].
Commonly the jet can be divided into two parts: the first one, immediately after the *Taylor cone*, is not subjected to the instabilities, and it results in a straight path, while the following section assumes a spiral appearance under the influence of fluctuations. J. He et al. have developed a mathematical analysis to predict the length of the stable part of the jet [136]. They assumed that, during the initial stage of jet formation, the electric force is dominant over the surface tension and the viscous force, causing the jet acceleration. The viscous resistance, however, opposes the motion of the fluid, and it results in an acceleration decreasing. When the acceleration reaches a constant value of zero, the jet becomes susceptible to any small perturbation, which causes the loss of the straight direction.
At this point, the *bending instability* begins. Because of the presence of accumulated charges on the fluid surface, a small perturbation in the jet can be irreversibly degenerate under the action of repulsive forces. In Fig. 3.4, a schematic representation of this phenomenon is provided. A little initial bending so evolves rapidly in a conical shape coil, while the jet continues to elongate under the influence of Coulomb repulsion of accumulated charges. The diameter decrease so much that the stream can become unstable for a second and even a third time generating other bending instabilities and, consequently, other smaller coils [137]. This hierarchical structure terminates together with the solidification of the polymer filament.

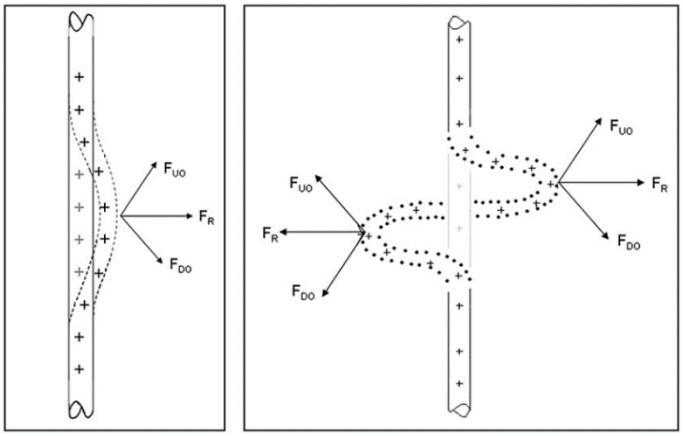

Fig. 3.4. Evolution of a bending instability from a small perturbation in the electrospun jet [137]

Contemporary, another class of instabilities, so-called *varicose instability*, influences the jet shape. Differently, from the bending instability, this class generates perturbations on the cross-section area, so that it is possible to define the fluctuations as *axisymmetric* [133]. It is possible to distinguish between two different effects, caused by two separate phenomena, which lead to the formation of branches and beads through the flux. The filament can be approximate to a smooth circular cylinder, but it is subjected to some undulating shape quasi-stable perturbation. When some charges accumulate on the surface of the jet, the ripple can lug these electrical charges to a lower potential, so that the portion of the stream involved acquires enough energy to create a new surface [137]. From the studies carried on by Plateau and Rayleigh, it is well known that the surface tension is a driving force that drives a fluid cylindrical flux to be broken to form spherical droplets, which minimize the energy content of the system. In electrospinning, it is possible to observe the same type of instability [138, 139], but the presence of an external electric field influences this phenomenon. In particular, higher charge density on the jet surface helps to stabilize the flux, and beads-free fibers can be formed [137].
Finally, when the jet reaches the collector before it is completely solidified, the *buckling* phenomenon can occur, forming a coil structure. This instability is related to the longitudinal compression acting on the jet when the collector decelerates it. Usually, the buckling coil presents quasi-constant value respect to the distance from the collector and the tip, so that it is possible to distinguish the distance-dependent bending coils by a simple analysis [137].

3.2.4 Solvent evaporation

From the instant the solution comes out from the spinneret, the solvent starts to evaporate, and it last until all the liquid will be all consumed. This process, of course, can affect the final morphology of the fiber. For this reason, it is necessary to choose the solvent carefully: if the evaporation rate is too high, the jet may solidify at the spinneret, blocking the solution flux; on the other hand, if the solvent boiling point is too high, non-dried fibers reach the collectors producing some defects such as *conglutination* [140]. Moreover, using two different solvents, one of which acts as non-solvent, it is possible to project highly porous nanofibers [62].
The formation of a rigid external skin is often caused by the high evaporation rates that are involved during electrospinning. At the same time, the inner part of the jet still presents a high amount of solvent. The subsequent evaporation, added with the volumetric shrinkage, permits the formation of fiber with the void in the interior. At this condition, the atmospheric pressure makes the fiber collapse, modifying the typical cylindrical shape into more complex forms (Fig. 3.5) [141].

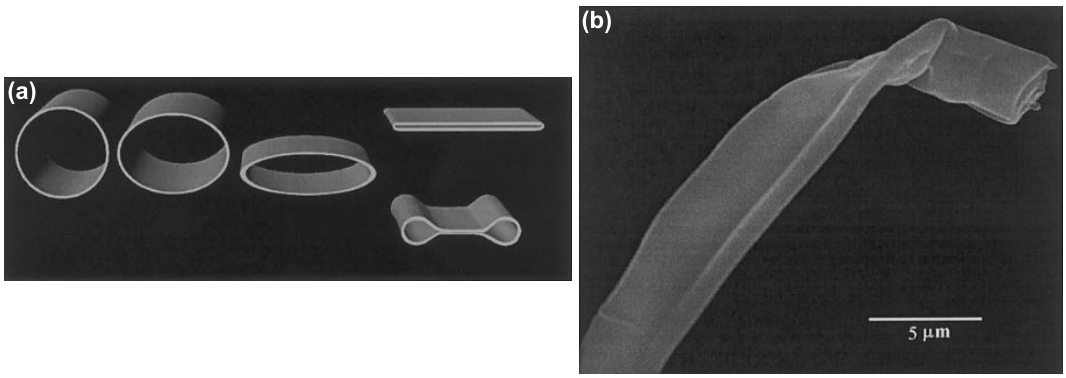

Fig. 3.5. (a) Representation of the collapsed modes of the skin on an electrospinning jet. (b) SEM image of a collapsed fiber of poly(ether imide) [141].

3.3 Influence of parameter

As it was just presented, the electrospinning process appears to be the result of quite complex interactions between different parameters, and many other of them were not introduced yet. It is possible to classify these parameters in three leading families: processing, solution, and environmental parameters. The processing

parameters depend form the electrospinning apparatus setup, so the applied voltage, the jet flowrate, the tip-to-collector distance, and the inner diameter of the needle. The principal solution properties include the initial polymer concentration, the polymer molecular weight, and the solvent properties; these can be considered primary parameters as they influence the so-called secondary parameters such as viscosity, surface tension, conductivity, dielectric constant, and volatility. Finally, environmental parameters comprehend temperature and relativity humidity. Many studies were carried out in order to understand how all these parameters can affect the final morphology of the fiber, and the findings are summarized below.

3.3.1 Applied voltage

The importance of the applied voltage in jet formation has been previously explained, and it is clear that it is necessary to overcome a threshold value to start the electrospinning process. What is not so clearly evidenced by the researcher is how an increase in applied voltage affects fiber morphology [140, 142]. In fact, some studies evidenced that higher applied voltage leads to a more significant polymer ejection and so larger fibers diameters [143–145]. Still, some others reported an increase in electrostatic repulsive forces with an increase in applied voltage, and this cause the formation of thinner fibers [146, 147]. On the other hand, many studies had reported that the increase in applied voltage generates a high probability of electrical instabilities in the liquid jet, which can bring to the formation of a beaded structure [142], following the mechanisms presented previously.

3.3.2 Solution flow rate

Using a syringe pump or similar devices is possible to control the amount of solution that flows through the spinneret and feeds the cone jet, but the overall rate at which the solution flows to the collector also depends from the applied voltage (which provides the force that pulls the solution out of the needle) and the internal size of the spinneret [140]. For this reason, the right balance of applied voltage and flow rate is crucial to realize homogeneous fibers in a short time. In fact, under the same conditions, an optimum range of flow rate exists, which allows us to produce uniform bead-free fibers. So, varying the flow rate is possible di modify the fiber morphology. In particular, at values lower than the optimum range, the material provided to the flux is not enough to feed it, so discontinuous fibers are generated. On the other hand, when the flow rate becomes too high, the solvent has no enough time to evaporate entirely before the jet has reached the collector so that morphological defects – such as beads and wrinkles – are generated. Moreover, increasing the amount of provided solution by increasing the flow rate produces a consequent increase in average diameter and pore dimension [62, 142, 148].

3.3.3 Tip-to-collector distance

This parameter can affect the fiber morphology basically in two ways: shorter distance means shorter time for the solvent to evaporate and to the jet to be stretched, longer distances, however, cause a decrease in the electric field. For this reason, when the distance is too short, the solvent cannot fully evaporate, and a flattened structure is formed [142, 148]. Usually, a minimum distance has to be found to reach the condition of dry fibers. Although, increasing this parameter results in a decrease in mean fiber diameter, due to the larger stretching time, and an increase in corona discharge and Rayleigh instabilities, which are responsible for the presence of defects such as fused or beaded fibers [140].

3.3.4 Polymer concentration and viscosity

Many studies were conducted about the influence of the polymer concentration on the final morphology of the fibers [142, 148–150]. This parameter resulted in one of the most important in controlling the electrospinning process because it affects many other crucial variables of the solution, such as the solution conductivity, the viscosity, and the surface tension. We know from Section 3.2 that these parameters play a crucial role in the process. So, it has been found that when the polymer concentration is so low that there are no entanglements

in solution, the viscosity is not high enough to compete with surface tension. A beaded structure is thus formed, sometimes the concentration could be so low that the structure results in discontinuous droplets. Increasing the solution concentration, the bead morphology changes, and conical shape is reached until a uniform fiber can be obtained.
Moreover, together with the concentration, also the fiber diameter grows. Usually, it is possible to identify four different concentration regimes: the dilute, the semidilute unentangled, the semidilute entangled, and the concentrated regimes [151]. At the overlap concentration (C^*), the first interactions between the separate polymeric chain appear, but there are not proper entanglements. They start to form only above the entanglements concentration (C_e), in the range of semidilute entangled solution [152]. In this region, bead-less fibers are generated, and the dependence of the diameter of the fibers from the concentration is more reliable [149]. On the other hand, when the polymer content, so the viscosity, is too high, the liquid is ejected by the tip with difficulty or worse it solidifies inside the spinneret, interrupting the jet.

3.3.5 Polymer molecular weight

The higher the polymer molecular weight, the longer and more branched are the polymeric chains, and the higher is the possibility that these chains crosslink among themselves [140]. This fact contributes to a decrease in the minimum concentration for a uniform fiber spinning, C_e. For this reason, generally, it is preferable to use polymer with a molecular weight above 3000 g mol^{-1}, or better 50,000 g mol^{-1} [140]. However, in some case, the intermolecular interactions are strong enough to substitute the interchain connections, and so lower molecular weight are also suitable for a stable electrospinning process.

3.3.6 Solvent properties

The two main characteristics that are used to evaluate the effectiveness of a solvent in the electrospinning process are the solubility of the polymer and the boiling point, which is indicative of the solvent volatility. These are not the only parameter affected by the nature of the selected solvent, but it can also strongly affect the solution viscosity, surface tension, dielectric constant, and electrical conductivity. In particular, it is essential to balance the solvent volatility to obtain the complete dehydration of the jet before the filament reaches the collector (avoiding the occurrence of some defects), but not too soon so that the fiber can be stretched during its path. The solvent volatility also influences the appearance of the fiber skin; in fact, it is studied that high volatile solvents quickly form high porous fibers, while for chemicals with a higher boiling point, the fiber surface results much smoother. Using a mixture of two solvents and varying their ratio in solution is also possible to control the pore density on the fiber [148].

3.3.7 Surface tension

Equation 3.6 already showed that varying the surface tension of the solution is possible to control the value of the applied voltage necessary to electrospun the fibers. For this reason, low surface tension solutions are preferable to the others, because they result in smoother filaments and also, in case of high voltage, the instability of the jet is greater, and the presence of non-uniformities is more likely. Moreover, the surface tension opposes the stretching of the stream favoring the formation of bead-on-string structures [140].

3.3.8 Conductivity

During the electrospinning, the conductivity of the system controls the capacity of the solution of forming ions [153]. Higher values of conductivity provide a greater number of ions, and so an increase of superficial electric charge. This phenomenon leads to a stronger electrostatic repulsion in the spun jet. Consequently, thinner fibers can be obtained [140, 142, 153], with the radius of the thread that is inversely related to the cube root of the electrical conductivity of the solution [154]. Although when the conductivity is too high, the jet becomes extremely unstable due to the presence of strong electric fields, so that an electrical discharge into the surrounding air can occur [140]. The nature of the polymer mainly determines the solution conductivity and

the solvent used. Still, it is eventually possible to modify the number of ions in solution by adding ionizable salts or surfactants, which can provide a better spinnability of the selected system [148].

3.3.9 Temperature

Many of the mentioned properties are closely related to temperature; for this reason, this environmental condition can play an important role in affecting the electrospinning process, but it is also difficult to isolate the effect which the only temperature has on the whole process [153]. In general, the increase in temperature causes an increase in solution electrical conductivity and a reduction in viscosity and surface tension. These modifications contribute to the growth of those forces that govern the jet stretching, resulting in fibers with a smaller diameter. On the other hand, at high temperatures, the solvent evaporates at higher speeds so that the jet dries sooner, and the filament cannot be stretched for a long time favoring the production of thicker fibers [140].

3.3.10 Humidity

The relative humidity (RH) mainly affects the solvent evaporation rate, which is proportional to the difference between the vapor pressure of the solvent and the vapor pressure in the surrounding air [140]. For this reason, at the high value of RH the evaporation rate of the solvent decrease. It follows that the jet can be stretched for a longer time resulting in thinner fibers. Besides, the RH has a significant influence also on surface roughness; it was observed that increasing the RH, a consequent increase in the pore size, the pore size distribution, and the number of pores is obtained [155]. This phenomenon can be explained by the fact that the evaporation of the solvent absorbs heat energy from the jet surface so that that temperature locally decreases. When the humidity is particularly high, some drop of moisture can solidify on the filament surface and then evaporate after the fibers solidification, resulting in the pore formation [155]. Finally, Huang et al. have also observed an influence of RH on the mechanical properties of the fibrous mats. In this work, PAN and PSU solutions were electrospun at different values of humidity (from 0% to 40%), and its effect on the tensile strength and the Young modulus were studied. In both cases, it was observed that after an initial increase in each property, when the humidity overcome a specific threshold value (20% for PAN fibers and 10% for PSU), the mechanical performances drop suddenly. The authors had observed that at high RH, the presence of water favors the phase separation: a skin layer forms when the jet comes in contact with the air, and this reduces the amount of solvent on the surface, which is a crucial element in the formation of fiber-to-fiber junctions. Fewer connections mean that the fibers do not interact with each other under applied stress, which brings a much lower mechanical performance [156].

3.4 Process innovations

During the years, the "classical" setup used in electrospinning has been developed to have the possibility to design new products and undergo the principal drawbacks of the process. Below the main engineering improvements are reported and briefly described.

The *multi-jet electrospinning* consists of the use of two or more extrusion flow at the same time that can ensure higher productivities. Still, this technique has an overwhelming advantage to deposit polymers with different characteristics at the same time, producing multicomponent membranes. In this way, it is possible to realize the matrices of fibers that show together functional properties challenging to obtain with a single species of polymer nanofiber [133]. The main challenge related to this development is represented by the electrical interaction between the jets [157], which causes the mutual repulsion of the streams. Increasing the distance of the needles and increasing the number of them, it is possible to reduce this undesirable effect [158]. Recently, another multi-jet technology has been introduced, but in this case, the increase in streams is not achieved by increasing the number of spinnerets, but by modifying the operating conditions to generate several Taylor cones from the same needle [158–160]. It is reported that the number of jets developed from the same meniscus is proportional to the applied voltage [161]. Many other different solutions for multi-jet electrospinning has been established. For example, the air-jet electrospinning, which consists of using gas or

air jets to form a bubble on the tip of the nozzle from which one or more jets can form [162, 163], or various other needleless design [158].
The *electro-blowing* represents a possible alternative to the classical electrospinning since an air blow is guided to pass around the main spinneret [164, 165]. The additional air blast provides another force in the fabrication of the fiber, making possible the spinning of the solution with high values of viscosity [164]. It is also possible to heat the air stream so that two more advantages can be added: the reduction of the viscosity (which favors the spinnability), and the enhancement of the evaporation rate of the solvent, both for the heat and the blowing air [164].
In order to make crosslinked fibers, it is possible to use the so-called *reactive electrospinning*. Usually, it is achieved in two different ways: by using crosslinking radiation (mainly the UV light) along the jet path [166, 167] or leading the two reactive components separately to the same spinneret, so that the reaction can start in the Taylor cone or along with the jet [168]. The main aim of such as technique is to increase the rate of solidification of the polymer or to electrospun the desired compound starting from the other two, usually when the product of the polymerization would have a viscosity too high to be directly electrospun.
Another innovative setup is the *dual-opposite-spinneret electrospinning*, which has been described by L. Li and co-workers in some works [169–171]. The apparatus uses two needles placed one in front of the other and connected to different electric potentials. The so produced jets attract each other and collapse into a third neutral fiber, which is collected and elongated by a mechanical force by the rotating collector [169]. By this technique, it is possible to reach useful improvements in the alignment of the fibers – it is possible to produce crossed mats – and in the fabrication of individual electrospun fibers [170].
In the *biased-AC electrospinning*, instead, using an alternate voltage bias is possible to achieve better stability of the jet, and so a more controllable alignment of the fibers [172]. As already explained (Section 3.2.3), in the DC electrospinning, small jet deformations evolve to more significant instabilities under the effect of the repulsive Coulombic forces. However, when the AC potential is used, the net charge in the surface of the fibers decreases, resulting in a consequent decrease in the overall instabilities. On the other hand, a lower charged jet also means smaller attractive force between the solution and the collector, so that the collection of the fiber becomes more difficult [173].
Sun et al. [174] have introduced an innovative setup to fabricate nanofibers with a different composition between the core and the shell. The *coaxial electrospinning* is based on the use of a special nozzle composed of an inner tube, which provides the core solution, and a coaxial annular tube for the enveloping material. This technique allows the design of fibers, which can combine different properties such as excellent mechanical resistance and unique surface characteristics, e.g., hydrophobicity [175].

4 Materials and methods

This chapter describes how the membranes were prepared, starting from the production of the solutions, and then describing the electrospinning process. In addition, all the instruments used to characterize the designed material and its functionalities are briefly described.

4.1 Materials

Recycled PET pellets from postconsumer PET water bottles (CR-8816) were kindly provided by Dr. Kazushi Yamada (Advanced Fibro-Science, Kyoto Institute of Technology, Kyoto, Japan). Sigma-Aldric purchased chitosan and sodium dodecylbenzenesulfonate (75-85% deacetylated, low molecular weight: 50-190 kDa). Trifluoroacetic acid (TFA), carbon tetrachloride, tetrachloroethylene, and sorbitan monooleate were obtained from Wako Co., Osaka, Japan. Kerosene, hexane, and sodium hydrogen carbonite were provided by Nacalai Tesque, Kyoto, Japan. All the chemicals were used as received without further purification.

4.2 Preparation of solutions

For the electrospinning, the first thing to do is to prepare the polymer solution. The solvent used in this experiment was the TFA. Then, to study the effect of the chitosan on r-PET membranes (in Fig. 4.1 the chemical structures), seven solutions with a constant amount of the polyester and different content of the biopolymer were prepared. The first solution contained only r-PET at 8wt% and was used as a reference. It was made by weighing the right amount of the components and mixing them with a planetary centrifugal mixer (ARE-310, Thinky Co., Tokyo, Japan) at 2000 rpm for 28.5 minutes, followed by degassing at 2200 rpm for 1.5 minutes. The other solutions contained an increasing content of chitosan from 1wt% to 4wt%. In this case, the two polymers were added to the solution separately to provide a better mixing; at first, the chitosan was added to TFA and mixed with the same procedure seen before, then the r-PET pellets were merged, and the as-prepared solution was remixed. After this process, the compounds were left around 10 hours on a magnetic stirrer to obtain homogeneous solutions.

The solution properties that can influence the electrospinning process (as presented in Section 3.3) were also measured. So, the viscosity of the solutions was evaluated by using a vibro viscosimeter (SV-1 and SV-100, A&D, Tokyo, Japan) with different sensibility (from 0.3 to 1,000 mPa s one, and from 1 to 100 Pa s the other). The conductivity, instead, was measured by an Oakton PC700 pH/mV/Conductivity/°C bench meter (Oakton Instruments, Vernon Hills, IL, USA).

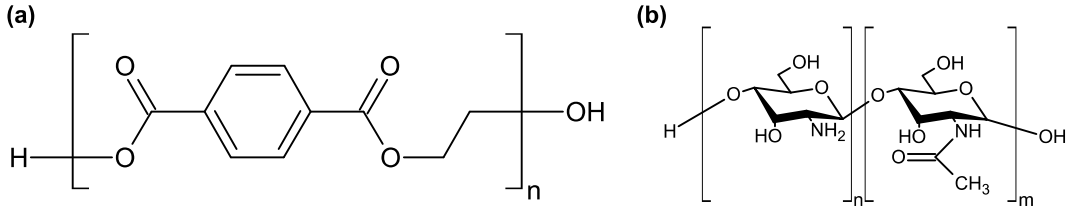

Fig. 4.1. Chemical structure of (a) polyethilene terephtalate and (b) chitosan

4.3 Electrospinning

The electrospinning process was carried out by using a build-up device of our design (Fig. 4.2) equipped with a syringe pump (KDS-100, KD Scientific Inc., Massachusetts, USA), a high voltage power supplier (HVU-30P100, MECC Co., Japan), and a cylinder steel collector covered, in this case, by a Nylon mesh No. 34. The main parameter which controls the process were set as follow and keep constant for all the different solutions:

- Flow rate: 0.5 mL·h^{-1}
- Applied voltage: 15 kV
- Tip-to-collector distance: 12.5 cm
- Collector rolling speed: 120 rpm
- Needle inner diameter: 30G
- Temperature: 22.5 ± 4 °C
- Humidity: 42.5 ± 8.5%

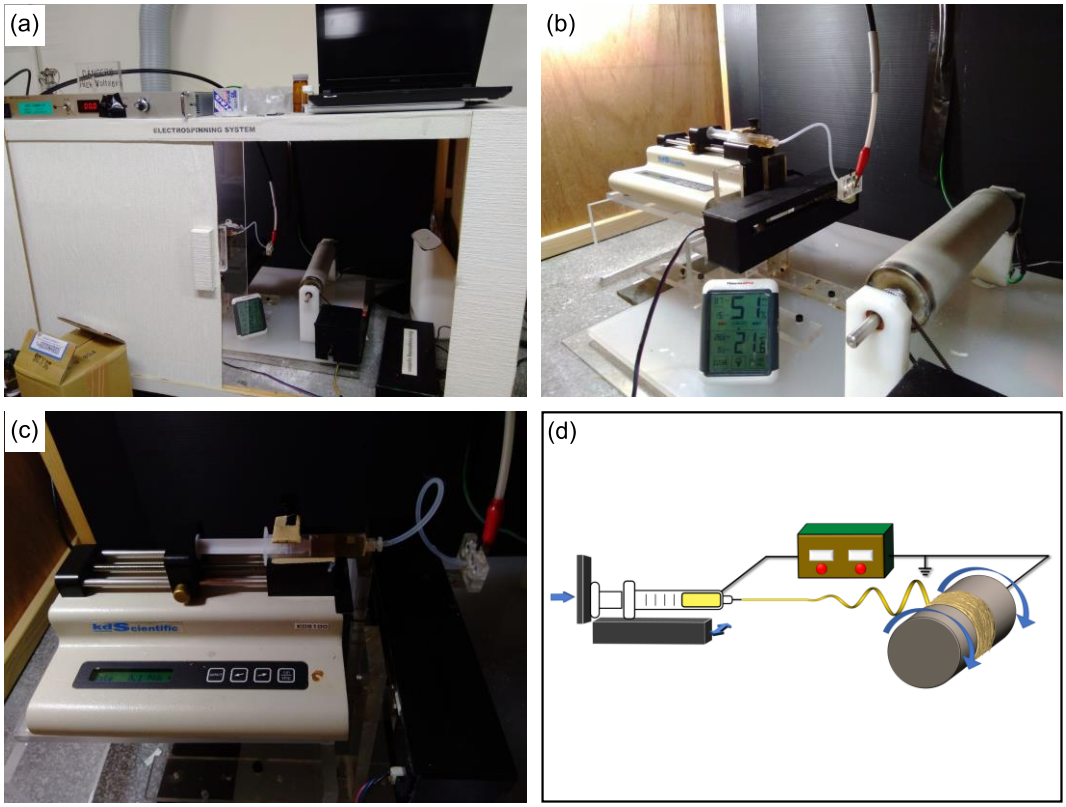

Fig. 4.2 From (a) to (c) are collected some pictures of the electrospinning apparatus used in this study. In (d) a chematic representation of the apparats is reported.

4.4 Membrane characterization

The as-prepared membranes were then analyzed in their main properties: morphological (mean diameter and roughness), chemical (surface composition), mechanical, and functional (the contact angle and filtration performance). A brief description of the used techniques follows.

4.4.1 Laser microscope

A 3D laser scanning microscope (VK-2000, Keyence Co., Japan) was used to collect and process some images and calculate the roughness of the membrane. The instrument, equipped with a lens with a magnification of 150X, was used to take the pictures. Nine of these pictures were then used to calculate the average roughness of the sample. This parameter can be measured using different methods, but in this case, the R_a values were chosen. In fact, R_a is one of the most common ways to measure roughness, and it represents the arithmetical mean roughness, which can be calculated as follows:

$$R_a = \frac{1}{l} \cdot \int_0^l |Z(x)|\, dx \tag{4.1}$$

where l is the length of the path along which the measurement is held and Z(x) is the coordinate of the surface of the membrane setting as zero the average high, as is possible to observe in Fig. 4.3.

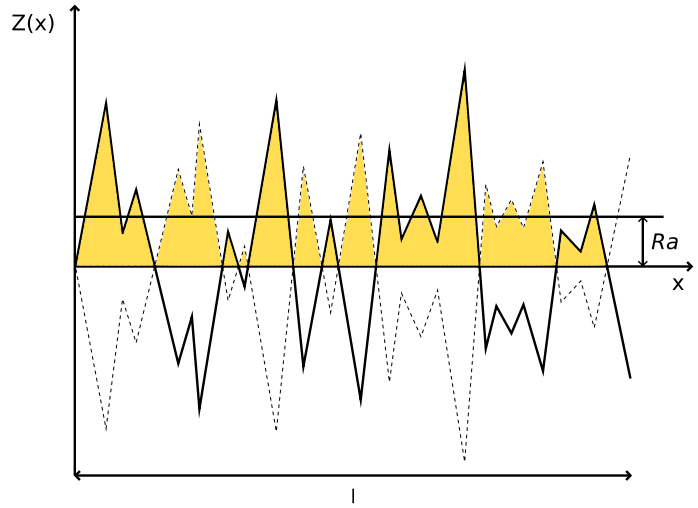

Fig. 4.3. Scheme for the calculation of the roughness Ra. The thick line represents the surface and the colored area the graph of $Z(x)$

4.4.2 FE-SEM

The Field Emission Scanning Electron Microscope (FE-SEM) (JEOL-7600, JEOL Ltd., Japan) was used to evaluate the morphology of the fibers and, in particular, to calculate the mean diameter of the filament. First of all, the non-conductive membranes were metalized with circa 20 μm of platinum. Then, ten pictures were collected from each sample using the secondary electrons signal, at 15.0 kV, and with a magnification of X10,000. The images were later elaborated by the ImageJ software to measure the diameter of 10 fibers for each picture.

4.4.3 FT-IR

The chemical composition of the fibers was studied by the Fourier-transform infrared spectroscopy (FT-IR). The instrument which was used is a FT/IR 4700 (JASCO International Co., Japan) equipped with a universal attenuated total reflectance accessory (ATR), and the measurement was performed in the range between 4000 and 400 cm^{-1}.

4.4.4 XPS

A further investigation of the chemical composition on the surface of the fiber was conducted using the X-ray Photoelectron Spectroscopy (XPS) (JEOL 9010, JEOL Ltd., Japan). In this case, the wide scan analysis in the range of 1,000 – 0 eV was used to find the elements contained on the fiber surface and to calculate the atomic percentage of each component by the software CasaXPS. In particular, the amount of nitrogen on the surface is indicative of the presence of chitosan, because both r-PET and chitosan are composed of oxygen and carbon atoms. In order to estimate the homogeneity of the distribution of the two polymers between the surface and the bulk of the fibers, a wide scan XPS analysis was also performed on pure chitosan powder and r-PET electrospun fibers.

The spectrograms showed a recognizable peak corresponding to the fluorine. This peak revealed the presence of residual TFA salt on the fiber surface [39, 41, 176], so the membranes were treated successively to eliminate this excess, which can pollute the filtrated liquid and enhance the acidity of the water during the filtration, at the risk of dissolving the chitosan. The XPS spectra were also collected after the neutralization process.

4.4.5 Neutralization

In order to eliminate the traces of fluorine on the fibers surface, the membranes were immersed in a supersaturated water solution of sodium hydrogen carbonate ($NaHCO_3$) [39] for at least 6 hours and then washed in pure water and dried at 50 °C for 4 hours. The solution was prepared to add more than 96 g/l (the solubility in water of the product) to pure water, mixing for around 1 hour, and filtering the as-prepared solution using a filter paper Advantec No.1 (Advantec, Tokyo, Japan). The chemical reaction involved in this process is schematically represented below (Fig. 4.4)

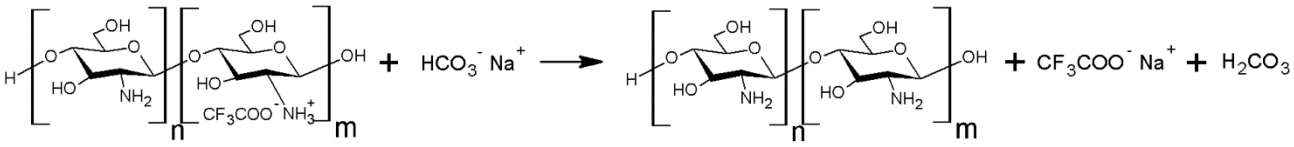

Fig. 4.4. The chemical reaction involved during the neutralization process is here reported

4.4.6 Mechanical test

The mechanical properties of the neutralized membranes were evaluated using a universal tensile testing machine (TENSILON RTF-1210, A&D Co., Japan), setting the crosshead speed at 1 $mm \cdot s^{-1}$ and the load cell at 100 N. The fibrous mat was so cut in dog bone-shaped specimens (type 5B in BS ISO 527: 2012) using a cutting blade. The as-prepared sample was then attached on a paper windows frame measuring 20x30 mm, with a window size of 4x25 mm, which functions as a tensile test stand. The measure was conducted on at least five samples from the same membrane. The instrument traced the force-displacement curves, but the typical strain-stress curves were obtained, and the maximum tensile stress and the elongation at break were calculated. In fact, the conversion of the values was done measuring the sample thickness using a micrometer screw gauge (Mitutoyo 406-250, Mitutoyo, Japan) and using the initial length of the sample and its width.

4.4.7 Contact angle

The contact angle of water and different types of oil – kerosene, hexane, carbon tetrachloride, and tetrachloroethylene – was measured using a Phoenix 300 contact angle system (Kromtek Co., Malaysia) and processing the collected images with ImageJ software. The water and the oil contact angle were measured depositing a drop of liquid with a syringe on the neutralized membranes and observing the following behavior. Because the samples showed an amphiphilic response, the membranes were also immersed in water, first, and then in oil to estimate the oil-in-water and the water-in-oil contact angle. In this case, a glass pool was built and filled with the liquid. The glass support with the attached membrane was so immersed in the bath and helped up by a thickness. When the drop of liquid was lighter than the one in the pool (e.g., kerosene in water), a curved needle was used to deposit the droplet under the sample (for more detail, see Fig. 4.5).

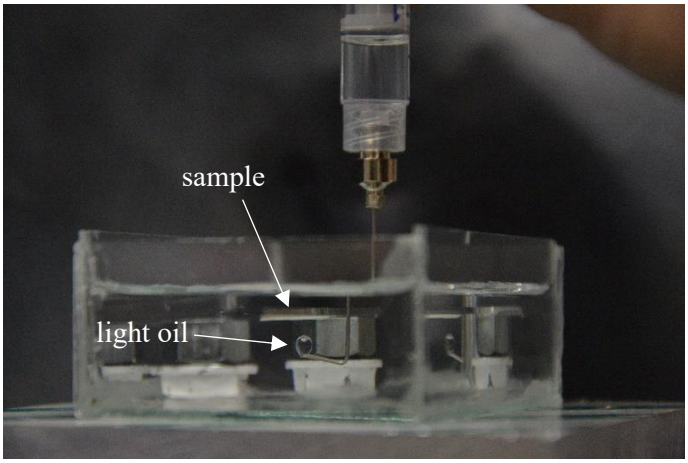

Fig. 4.5. The setup for underwater oil cantact angle measurement in case of light oil. The same configuration was used for underoil water contact angle analysis with heavy oils.

4.4.8 Intrusion pressure

The intrusion pressure of the membrane evaluates the amount of liquid that the membrane can accumulate over itself before the first droplet of the retained liquid passes through the fibrous mat. In order to measure this dimension, the membrane was cut in circles with a diameter of 25 mm that was placed between two filter holders KGS-25 (Advantec CO., Japan), with a stainless-steel supporter. The membrane is so prewetted by the denser liquid (water, in case of the test with kerosene and hexane, carbon tetrachloride or tetrachloroethylene, in the other cases) and the upper part of the filer holder is filled with 10 ml of the lighter liquid. Using a controlled flux of nitrogen, the pressure on the membrane is enhanced until the first droplet of the light liquid permeates through the membrane. At this point, the value of the pressure read on a manometer was used to calculate the amount of the intrusion pressure by the following equation:

$$p_i = (p_f - p_0) + \rho_l g h_l \tag{4.2}$$

where p_i is the intrusion pressure, p_f is the value of pressure read on the manometer, p_0 is the atmospheric pressure, ρ_l is the density of the liquid over the membrane, g is the gravitational acceleration, and h_l is the high of the column of liquid over the membrane. Fig. 4.6 shows a schematic of the apparatus used.

4.4.9 Filtration test

The filtration performance of r-PET@Chit2 was tested both in oil and water separation for a simple mixing solution and emulsion. The water-oil mixtures were prepared by weighing 10 ml of water and 10 ml of the oil and putting them in the same baker without further mixing so that the separation of phases occurs. After, the membrane was cut in a circle with a diameter of 25 mm, fixed with the filter holder, and prewetted with the heavier liquid (water in the case of light oils, the oil in the case of the heavy one). The solution was so poured inside the holder, and the separation of the denser solvent from the mixture was performed. The collected liquid was so weighted to measure the liquid flux and the filtration efficiency.

On the other hand, the emulsions ware prepared using two types of surfactants: sorbitan monooleate for the water in oil and sodium dodecylbenzenesulfonate for the oil in water emulsions. First of all, the continuous phase was weighted, and 0.1wt% of the surfactant is added. The so prepared solution was then mixed with a disperser Ultra Turrax IKA T-18 (IKA; Werke GmbH & Co. KG, Staufen, Germany) for 5 minutes at 18,000 rpm to homogenize the mixture and after the dispersed phase was added in a concentration of 1wt% and then mixed again for 5 min. The size of the emulsion was measured by a dynamic light scattering (DLS) analyzer (ELSZ-1000, Otsuka Electronics Co., Ltd., Osaka, Japan). After, the specimen with the same shape as before was prepared in the filter holder, which is then filled with 15 ml of emulsion – kept constant to not modify the

pressure applied on the membrane. After 1 minute, the filtrated liquid was weighted to calculate the flux, while the filtration efficiency was measured by a gas-liquid chromatography-mass spectrometry (GCMS-QP2010 Ultra, Shimadzu, Kyoto, Japan) for the oil in water emulsions and a Karl Fischer Moisture Tritator MKC-710 (Kyoto Electronics Manufacturing Co., Kyoto, Japan) for the water in oil emulsions.

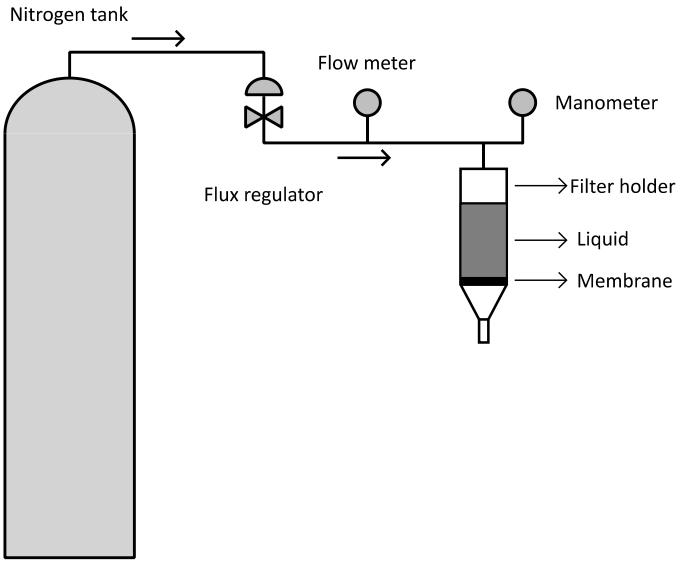

Fig. 4.6. Scheme of the apparatus used to measure the intrusion pressure values; it is formed by different components: the nitrogen tank, a flux regulator, a flow meter, a manometer, and the filter holder, where the membrane and the tested liquid were placed.

5 Results and discussion

In this section, all the obtained results are presented and explained. The data are divided according to the class of properties of which they provide information: morphological, chemical, mechanical, and functional. For the reason of time, the morphological, chemical, and mechanical properties were used to study the fibrous mats to choose the membrane, which showed the best characteristics and investigate its functionality.

5.1 Morphological characterization

The morphological characterization consists of evaluating the aspect of the electrospun fibers, the average diameter, the roughness, and the possible presence of beads. This study results significantly in the first phase of electrospun membranes design because, in this way, it is possible to adjust all the parameters discussed in Section 3.3 to obtain the fibrous mats with the desired properties.

5.1.1 Laser microscope and FE-SEM

The morphology of the membranes, especially the roughness, affects in a significant way wettability and the other surface properties [40]. For this reason, the mean fiber diameter and, in general, the morphology of the fibers were carefully studied. First of all, the appearance of the tissue was evaluated. As shown in Fig. 5.1, the as-spun r-PET fibers presented a beaded structure that is symptomatic of great instabilities during the electrospinning process (Section 3.2.3). With the increase of the chitosan concentration and, as shown below,

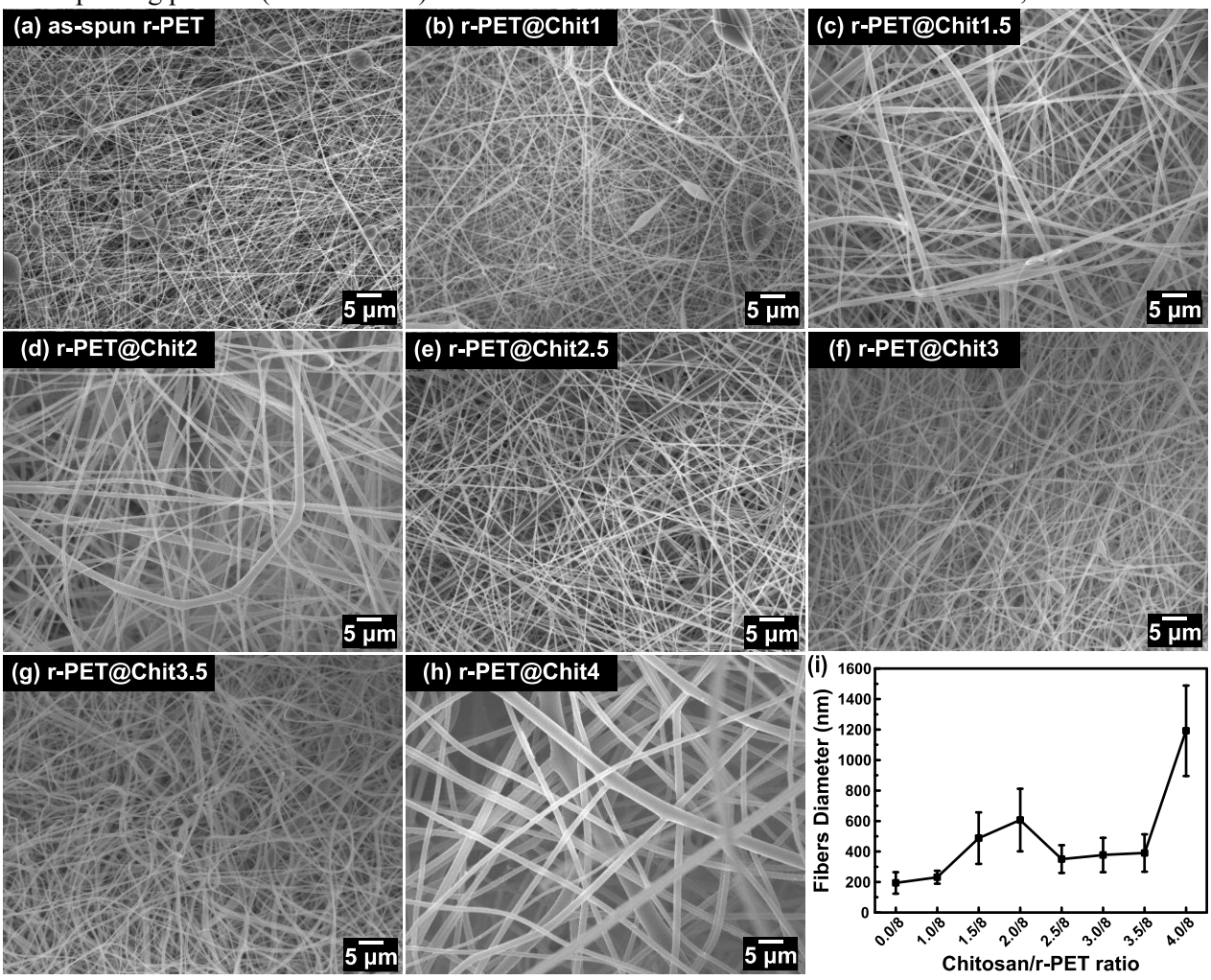

Fig. 5.1 Images collected the FE-SEM using the secondary electron signal of the membrane (a) as-spun r-PET, (b) r-PET@Chit1, (c) r-PET@Chit1.5, (d) r-PET@Chit2, (e) r-PET@Chit2.5, (f) r-PET@Chit3, (g) r-PET@Chit3.5, and (h) r-PET@Chit4, from which the morphology of the fibers is appreciable. (i) representation of fibers mean diameter for all the membrane

the solution viscosity, the fibers improve their stability. For amounts higher than 1.5wt%, the electrospun fibers presented a sufficiently uniform shape and a bead-less structure. This result implies that the parameters selected for the electrospinning process can be considered fairly satisfactory to obtain a fine yarn. Moreover, from the collected pictures, it is possible to appreciate the absence of porosity on the surface of the fibers, which also represents an important aspect that can affect the superficial properties of the membranes.

From the FE-SEM analysis, the values of the mean diameter of the electrospun mats were also measured. The data show how, as a result of the increase in the chitosan content in the solution, the diameter initially grew – from ca. 194 to 607 nm – since the chitosan content in the solution was lower than 2wt%. Still, for higher concentrations, the fiber size decreased for the r-PET@Chit2.5 membrane and then remained constant for the two higher amounts. Finally, when the solution contains 4wt% of chitosan, the mean diameter increased again and reached 1,191 ± 297 nm (Fig. 5.1i and

Table **5.1**).

The laser microscope also measured the roughness of the membrane. As reported in Fig. 5.2, this dimension seems to be closely related to the fiber diameter; in fact, it follows a similar trend. The fibrous mat composed only by r-PET, in fact, has a relatively smooth surface, with a *Ra* equal to 1.4 ± 0.2 μm, and it increases until it reaches the values of 8.3 ± 1.5 μm in the r-PET@Chit4 membrane.

Normally, as explained above in Section 3.3.4, an increase in polymer content corresponds in fibers with a bigger diameter, basically due to the rise in the solution viscosity. For this reason, it was necessary to study more thoroughly the two main solution parameter which affects the electrospinning process in order to try to explain this unexpected behavior.

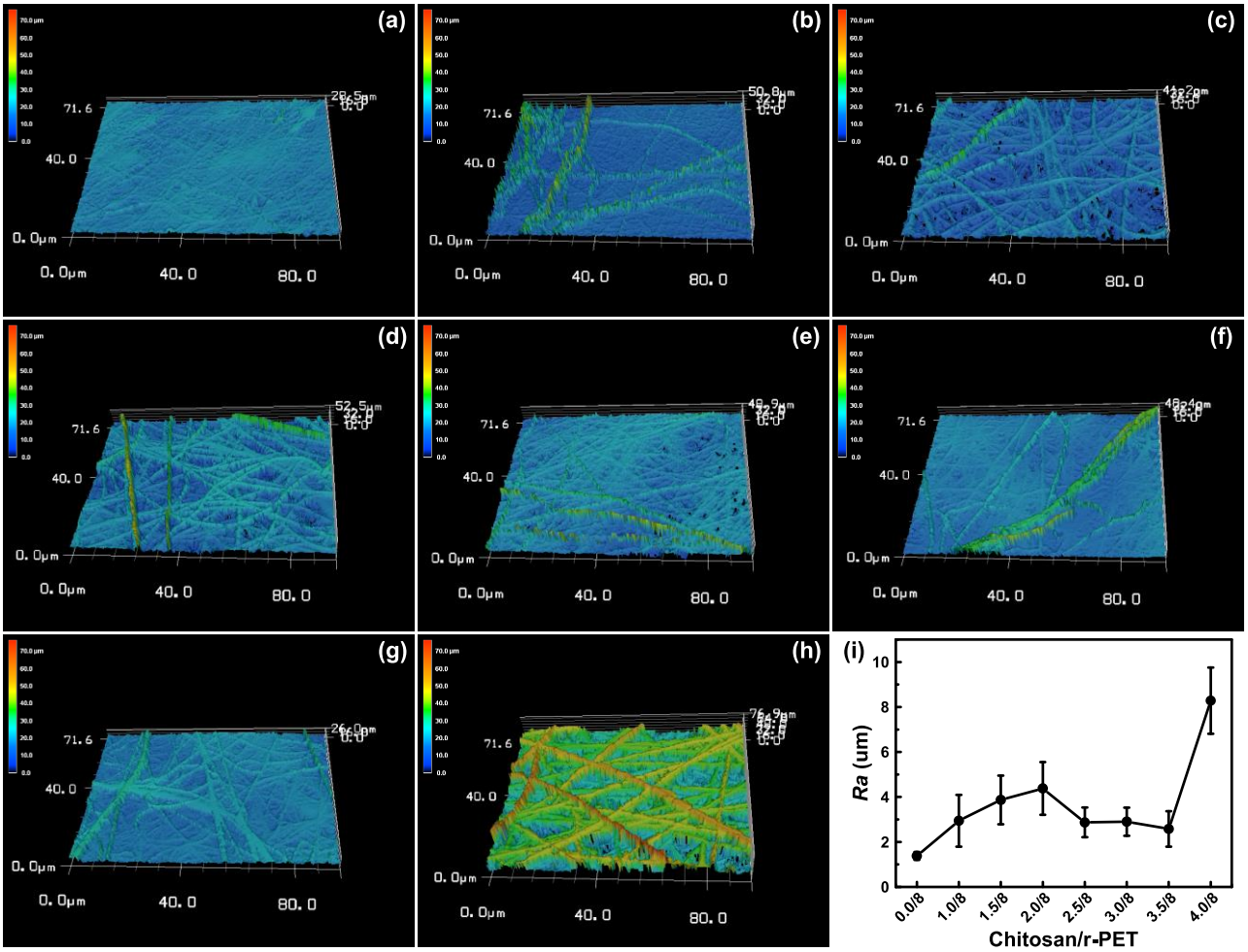

Fig. 5.2 The 3D elaboration of the laser microscope images of the membrane (a) as-spun r-PET, (b) r-PET@Chit1, (c) r-PET@Chit1.5, (d) r-PET@Chit2, (e) r-PET@Chit2.5, (f) r-PET@Chit3, (g) r-PET@Chit3.5, and (h) r-PET@Chit4. It is also reported the plot of the values of Ra over the polymers ratio

Table 5.1 For completeness the roughness and the diameter measured for each sample are here reported

Sample	*Ra* [µm]	Diameter [nm]
as-spun r-PET	1.4 ± 0.2	194 ± 70
r-PET@Chit1	2.9 ± 1.2	231 ± 42
r-PET@Chit1.5	3.9 ± 1.1	488 ± 169
r-PET@Chit2	4.4 ± 1.2	607 ± 205
r-PET@Chit2.5	2.9 ± 0.7	351 ± 91
r-PET@Chit3	2.9 ± 0.6	377 ± 113
r-PET@Chit3.5	2.6 ± 0.8	391 ± 123
r-PET@Chit4	8.2 ± 1.5	1,191 ± 297

5.1.2 Viscosity and conductivity

In order to understand further the response of the prepared solutions during the electrospinning, the viscosity and the conductivity were measured. From Section 3.3.4, it is known that an increase in solution viscosity implies a consequent increase in fiber diameter, while higher conductivity values facilitate the stretching of the jet. In Fig. 5.3, the experimental values of these two sizes are plotted. It is shown that the conductivity of the solution increased almost linearly with the chitosan concentration. On the other hand, the viscosity had the

typical bi-exponential trend [177]: until the level of chitosan was lower than 2wt%, the viscosity increased slowly, while for higher concentrations the growth was much more rapid. The threshold value around the chitosan concentration of 2.5wt% is attributable to the *entanglement concentration* (C_e) [178]. For this reason, the morphology of the fibers improved nearly by this concentration (Section 3.3.4).

The experimental evidence showed that for small concentrations, the increase in viscosity affected the electrospinning process strongly [4–6], while, for polymer concentrations higher than 2wt%, the conductivity becomes the more effective parameter. Finally, B. Cramariuc et al. [147] found experimentally that after a specific value of conductivity, a further increase provoked not the decreasing, but the growth in fibers diameter. This phenomenon can explain the last evident increase in the dimension of the r-PET@Chit4 fibers.

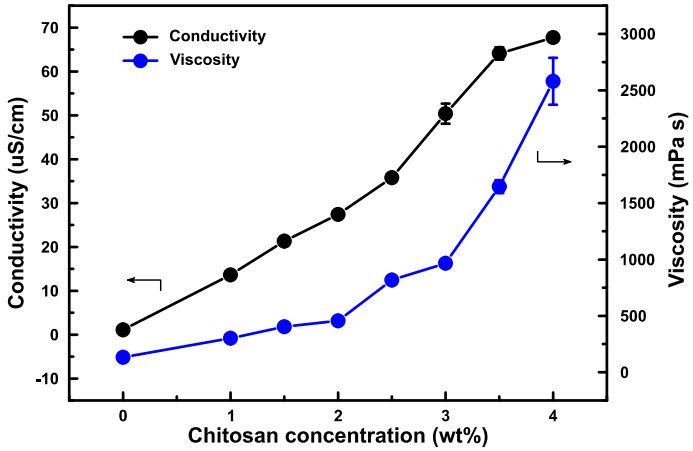

Fig. 5.3. Solution viscosity and conductivity dependence form the chitosan concentration

5.2 Chemical composition

The functional properties analyzed above are strictly related to the chemical composition of the material (Section 2), in particular, at its surface. For this reason, in this section, the chemical composition of the membranes was studied employing FT-IR and XPS analysis. Furthermore, from these data, an undesired content of residual TFA salt was evidenced, so the fibrous mats were treated as presented in Section 4.4.5 and analyzed again.

5.2.1 FT-IR and XPS

IR spectra of all membranes were detected by attenuated total reflectance Fourier transform infrared (ATR FT-IR) analysis. The main aim of this investigation was to detect the presence of the chitosan on the surface of the fiber. In Fig. 5.5a, the spectra of the as-spun r-PET and r-PET@Chit4 membranes are compared with the signal collected for the pure chitosan powder. The peaks related to the N-H and O-H stretching (3400 and 3300 cm^{-1}), the two associated with the C-H symmetric and asymmetric at 2921 and 2877 cm^{-1}, and the N-H bending at 1590 cm^{-1} [179, 180] are visible in the powder spectrum. However, the fibrous membrane does not present the same signals and, on the other hand, gives some unexpected peaks. At 1675 cm^{-1} and 1530 $cm^{-1,}$ there are two peaks, which correspond to the stretching of the protonated amino group (NH_3^+). At 1200 $cm^{-1,}$ the absorption of the carboxylate group is observable; in the range between 840-720 cm^{-1} other three peaks are observable. All this information, together, can be reconducted to the presence of trifluoroacetic acid in fibers as amine salts [39, 41, 176].

Moreover, form Fig. 5.5b is also possible to appreciate the increase in that signals related to the presence of TFA. This result highlights that the amount of chitosan in the fibers is effectively increased by the rise of the content of the bio-polymer in the solution.

For a further investigation of the surface composition, an XPS wide-scan analysis was also executed on the fibrous membranes. The first significant result concerned the presence of a peak corresponding to the presence

of nitrogen on the surface of the fibers, visible at 399 eV (Fig. 5.4), which means that chitosan is actually present in the membranes. Secondly, the analysis confirmed the presence of residual fluorine on the surface of the samples from the characteristic peaks at 686 eV, in the spectrum of the r-PET@Chit1 membrane.

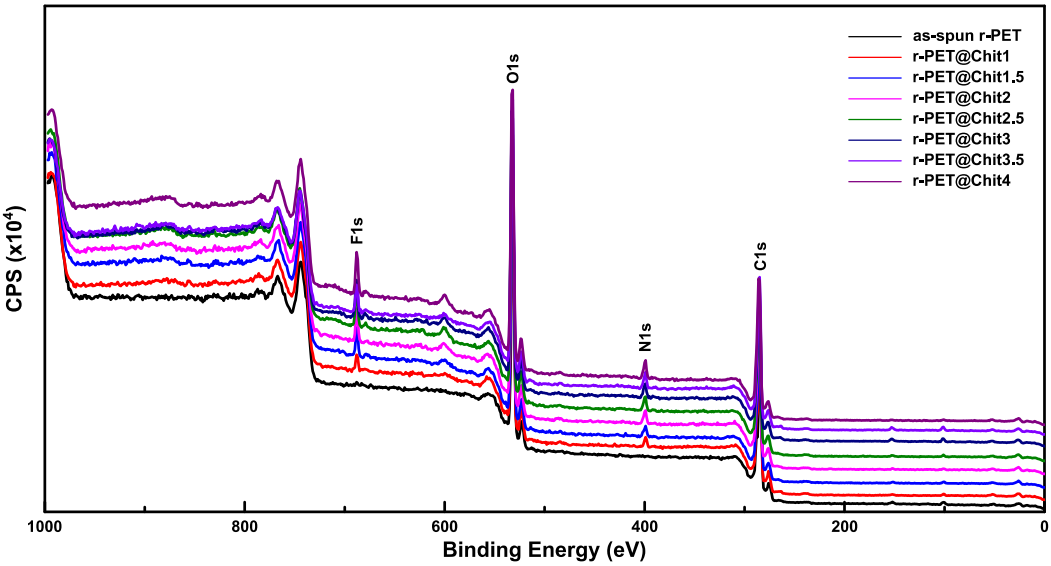

Fig. 5.4. XPS spectrum of the spun membranes. The peaks related to F1s, O1s, N1s, C1s are evidenced.

5.2.2 Neutralization

Because in case of contact between the membrane and the water the salt residues could dissolve, polluting the liquid with a toxic component and decreasing its pH (which can provide the chitosan dissolution [41]), it is necessary to neutralize the membrane eliminating the TFA traces as described in Section 4.4.5. After this chemical process, all the morphological and chemical analyses presented so far were repeated.

From FE-SEM analysis, it was found that neither the dimension of the fiber (

Table **5.2**) nor their external appearance (Fig. 5.6) was affected by the treatment. This aspect is particularly relevant because it means that, despite the procedure, it is still possible to control the membrane morphology. Although the laser microscope measurements showed that the chemical treatment modified the roughness of the membranes, homogeneously flattening the fibrous mats (Fig. 5.6)

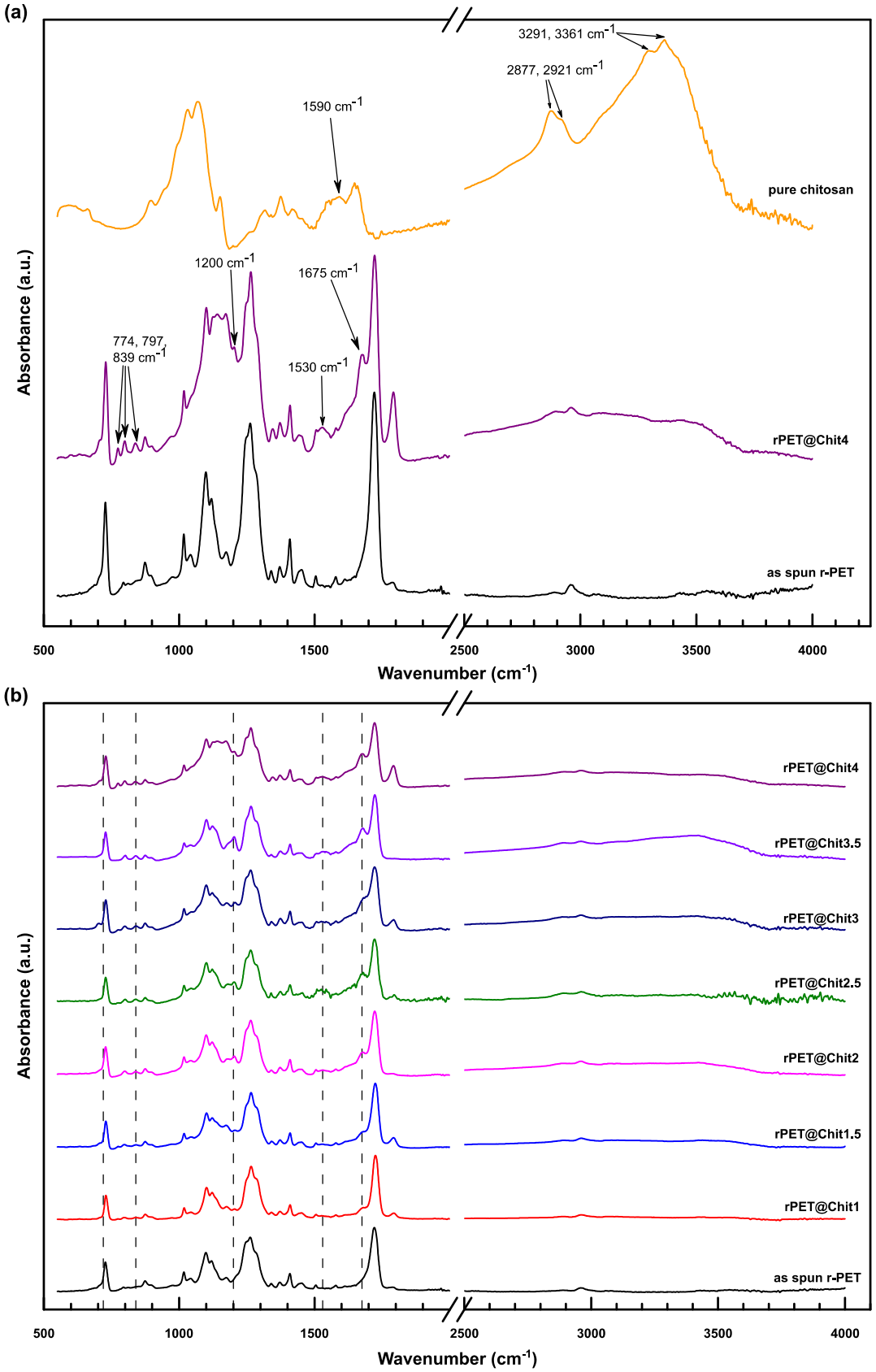

Fig. 5.5 (a) FT-IR spectra of as-spun r-PET, pure chitosan and r-PET@Chit4 as example. The evidenced peaks highlight the presence of residual TFA salt in the membrane. (b) The FT-IR spectra recorded for all the spun membranes are shown to compare them and see the increasing of the signals related the residual salt.

Table 5.2 Comparison between the mean diameter of the fibers before and after the neutralization process

Sample	Diameter [nm]	
	as-spun	neutralized
r-PET@Chit1	231 ± 42	239 ± 56
r-PET@Chit1.5	488 ± 169	484 ± 255
r-PET@Chit2	607 ± 205	614 ± 208
r-PET@Chit2.5	351 ± 91	341 ± 112
r-PET@Chit3	377 ± 113	315 ± 75
r-PET@Chit3.5	391 ± 123	357 ± 80
r-PET@Chit4	1,191 ± 297	958 ± 355

In addition, the IR spectra and the XPS analysis were collected, and the results were plotted in Fig. 5.7. As expected [39], the absorption peaks in IR spectra corresponding to the wavelength of 1675, 1530, 1200, and the range 840-720 cm^{-1} disappeared and, in contrast, the amino group stretching signal growth sensibly. This fact means that during the neutralization process, the protonated amino groups gradually react with the sodium hydrogen carbonate, and the number of neutral groups increases, and, consequently, the absorption at the corresponding IR wavelength.

The XPS analysis confirmed the findings of the previous measurement, in fact, both from the spectrum of the wide scan (Fig. 5.7c) and from the calculation of the atomic composition of the surface (Table 5.3), the fluorine content can be considered negligible. Moreover, K. Jung et al. [43] reported that the electrospun

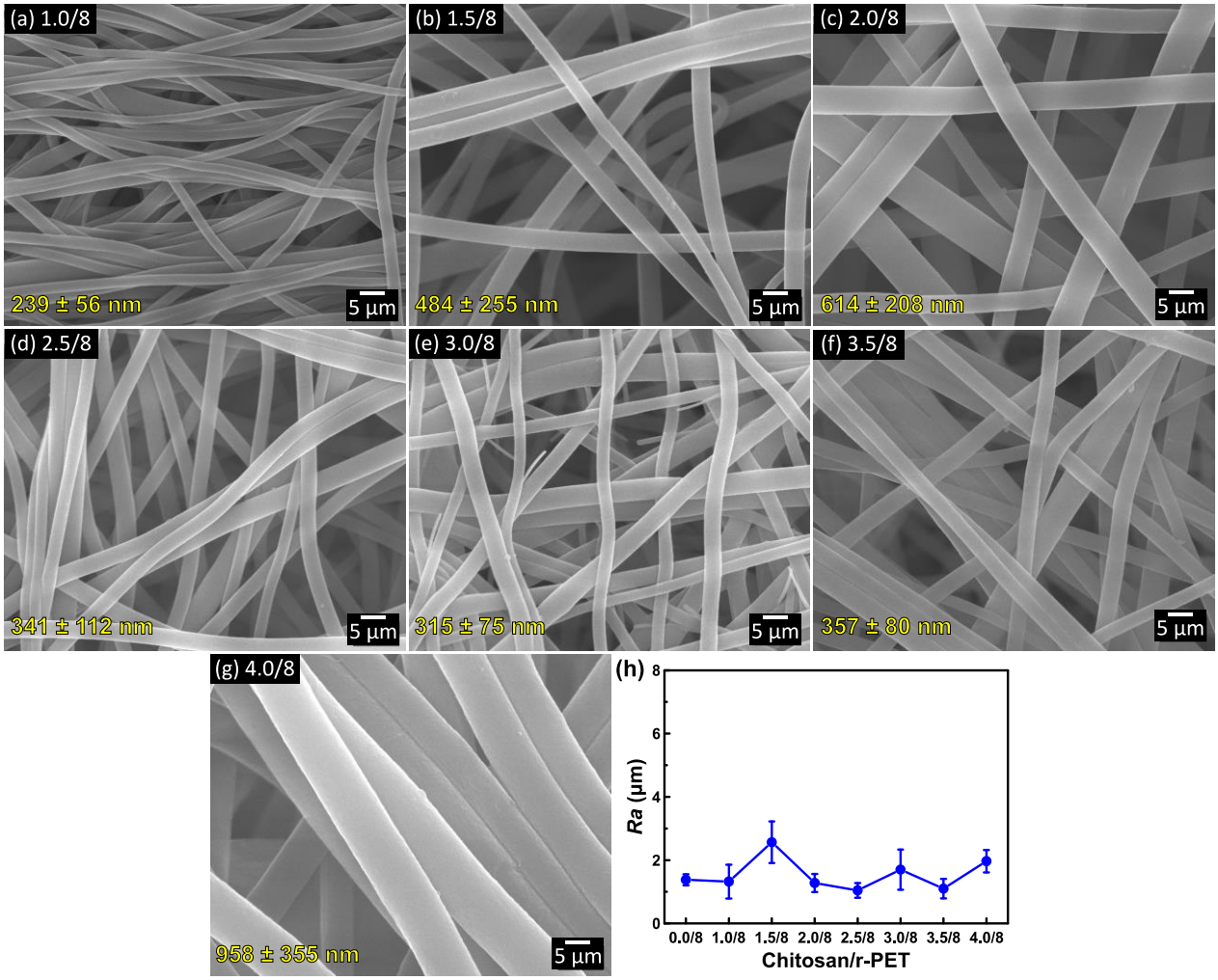

Fig. 5.6 Secondary electron signal from FE-SEM analysis of neutralized membranes at a magnification of X10,000. From a) to g) respectively the chitosan concentration growth from 1.0/8 to 4.0/8. (h) Roughness of the membranes after the neutralization.

chitosan in bled with the r-PET tends to concentrate more on the surface of the fibers than in their bulk. Because in this study, the external composition of the filaments is crucial for the membrane properties, this aspect was further investigated. In particular, the atomic percentage of the prepared membranes was compared with an expected composition, calculated from the XPS analysis of the pure chitosan powder and the r-PET fibers. In order to reach this purpose, the following equations were used:

$$\%\mathrm{at(N)_{chit}} = \frac{\mathrm{n^o\ atoms(N)_{chit}}}{\mathrm{n^o\ atoms_{tot_{chit}}}} = \frac{\mathrm{n(N)_{chit}}}{\mathrm{n_{tot_{chit}}}} \cdot \frac{\mathrm{N_A}}{\mathrm{N_A}} = \%\mathrm{mol(N)_{chit}} \tag{5.1}$$

where $\%\mathrm{at(N)_{chit}}$ is the atomic percentage of carbon in chitosan powder (measured by the XPS), $\mathrm{n(N)_{chit}}$ is the number of moles of carbon in chitosan and $\mathrm{n_{tot_{chit}}}$ is the total number of moles in chitosan, $\mathrm{N_A}$ is the Avogadro number, and $\%\mathrm{mol(N)_{chit}}$ is the molar percentage of carbon in chitosan powder;

$$\%\mathrm{mol(N)_{chit}} \cdot \mathrm{AM(N)} = \frac{\mathrm{m(N)_{chit}}}{\mathrm{n_{tot_{chit}}}} \tag{5.2}$$

where $\mathrm{AM(N)}$ is the atomic mass of carbon. Analogous calculations were performed also form the atomic percentage of oxygen and nitrogen in chitosan. After that, the weight percentage of each component was calculated by the following equations:

$$\frac{\mathrm{m(C)_{chit}}}{\mathrm{n_{tot_{chit}}}} + \frac{\mathrm{m(O)_{chit}}}{\mathrm{n_{tot_{chit}}}} + \frac{\mathrm{m(N)_{chit}}}{\mathrm{n_{tot_{chit}}}} = \frac{\mathrm{m_{tot_{chit}}}}{\mathrm{n_{tot_{chit}}}} \tag{5.3}$$

$$\frac{\mathrm{m(N)_{chit}}}{\mathrm{n_{tot_{chit}}}} \cdot \left(\frac{\mathrm{m_{tot_{chit}}}}{\mathrm{n_{tot_{chit}}}}\right)^{-1} = \frac{\mathrm{m(N)_{chit}}}{\mathrm{m_{tot_{chit}}}} = \%\mathrm{wt(N)_{chit}} \tag{5.4}$$

where $\mathrm{m_{tot_{chit}}}$ is the total mass of chitosan and $\%\mathrm{wt(C)_{chit}}$ is the weight percentage of carbon in chitosan. The same procedure was then used also with the other components of chitosan and with all the elements of r-PET. So, the theoretical homogeneous composition of the fibers was so calculated:

$$\%\mathrm{wt(N)_{chit}} \cdot \%\mathrm{wt(chit)_{fiber}} + \%\mathrm{wt(N)_{rPET}} \cdot \%\mathrm{wt(rPET)_{fiber}} = \%\mathrm{wt(N)_{fiber}} \tag{5.5}$$

$\%\mathrm{wt(chit)_{fiber}}$ and $\%\mathrm{wt(chit)_{fiber}}$ – respectively the weight percentage of chitosan and recycled PET in fibers – were known by the amount of material used to prepare the solution. Finally, the atomic composition of the fibers for each component was found:

$$\frac{\%\mathrm{wt(N)_{fiber}}}{\mathrm{AM(N)}} \cdot \frac{1}{\frac{\%\mathrm{wt(C)_{fiber}}}{\mathrm{AM(C)}} + \frac{\%\mathrm{wt(O)_{fiber}}}{\mathrm{AM(O)}} + \frac{\%\mathrm{wt(N)_{fiber}}}{\mathrm{AM(N)}}} = \%\mathrm{at(N)_{fiber}} \tag{5.6}$$

In order to evaluate the distribution of the chitosan between the bulk and the surface of the fibers, the concentration of the nitrogen was taken into account. In fact, it is the only element that differentiates the chitosan from the r-PET. The results were so collected and compared with the measures of XPS of the membranes in Table 5.4. The concentration in the case of the fibrous filters was generally higher than the one calculated using the pure components. This result suggests that the chitosan tends to concentrate more on the surface of the fibers [43]. It is possible that, during the electrospinning, the free charges in the solution are forced to accumulate on the outermost part of the flux and the dissolved chitosan, rich in protonated amine groups, is dragged on the surface.

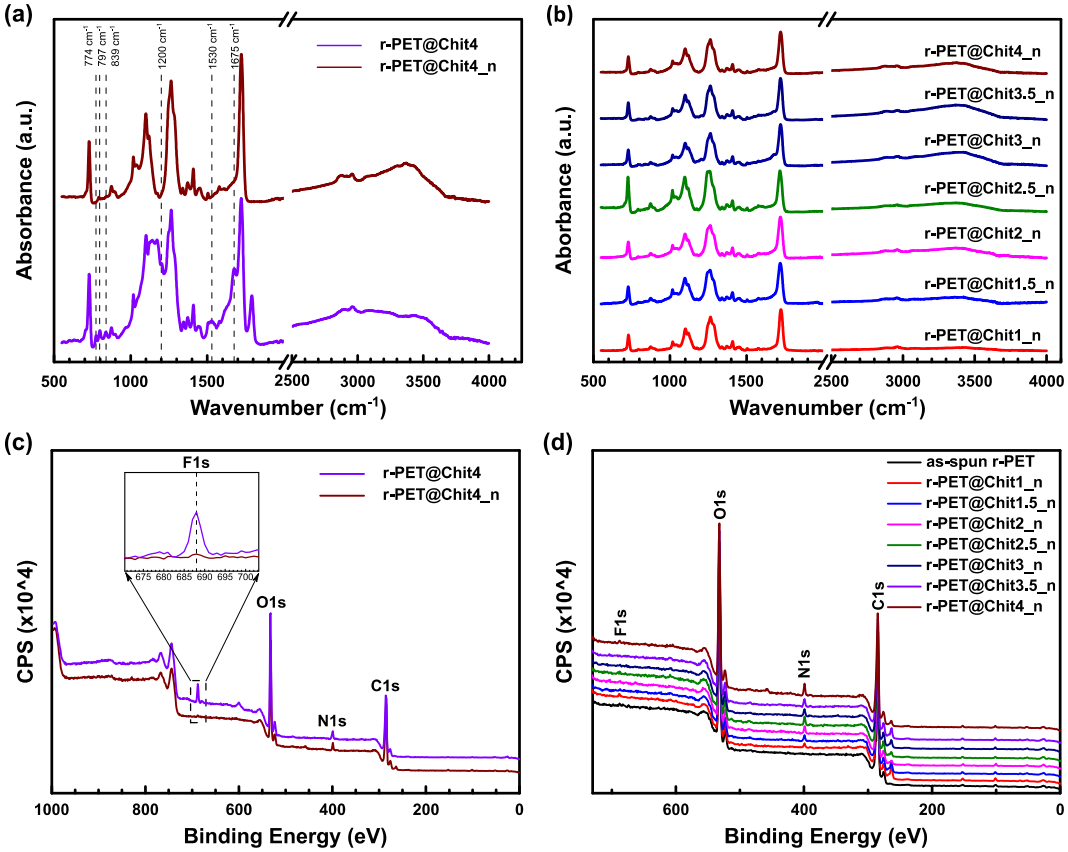

Fig. 5.7 (a) FT-IR spectra of r-PET@Chit4 before and after the neutralization. The peaks which disappear after the treatment are evidenced. (b) Comparison of the IR absorption spectrum of all the neutralized samples. (c) The XPS signal of the same membranes as example. The region of the F1s peak is enlarged to better evaluate the intensity of that signal. (d) XPS spectra of all the membrane after neutralization

Table 5.3 Atomic percentage of the elements on the membrane surface both before and after the neutralization.

Sample	%at C		%at N		%at O		%at F	
	as-spun	neutralized	as-spun	neutralized	as-spun	neutralized	as-spun	neutralized
r-PET@Chit1	66.90	69.20	1.75	1.21	30.26	29.31	1.11	0.29
r-PET@Chit1.5	64.77	69.34	2.50	1.53	30.76	29.00	1.99	0.14
r-PET@Chit2	63.91	68.53	2.52	1.95	31.50	29.34	2.09	0.18
r-PET@Chit2.5	62.86	68.92	2.88	1.92	31.34	28.94	2.93	0.24
r-PET@Chit3	61.95	68.51	2.96	1.94	32.50	29.47	2.60	0.09
r-PET@Chit3.5	62.72	68.58	3.05	1.91	32.45	29.34	1.79	0.18
r-PET@Chit4	60.22	68.01	3.79	3.12	32.85	28.58	3.14	0.29

Table 5.4 Comparison between the atomic percentage of nitrogen on the neutralized membrane surface and the one calculated supposing a homogeneous distribution of chitosan between the surface and the bulk of the fibers

Sample	%at N	
	membrane	theoretical
r-PET@Chit1	1.21	0.67
r-PET@Chit1.5	1.53	0.97
r-PET@Chit2	1.95	1.23
r-PET@Chit2.5	1.92	1.49
r-PET@Chit3	1.94	1.67
r-PET@Chit3.5	1.91	1.87
r-PET@Chit4	3.12	2.05

5.3 Mechanical properties

The membranes were also evaluated in their mechanical properties. The strain-stress plots in Fig. 5.8 showed a tendency for the mats to break in a two-step process: during the first stage of the process, a relatively small elongation was obtained by the increasing of the applied stress, but after a certain point, the deformation increased significantly until the specimen breaks. The decrease in the slope of the stress-strain curve can be explained by the presence in the membrane of the inter-bonding structure [44]. In fact, in the first step, the non-bonded segments of the fibers aligned and elongate until some of the fibers entanglements break, with a consequent decrease in the membrane rigidity. Because the alignment of the fibers in the membranes is non-ordered and it can be affected by the reorganization of the fibers during the neutralization process, the mechanical characteristics of the fibrous mat vary greatly regardless of the chitosan content.

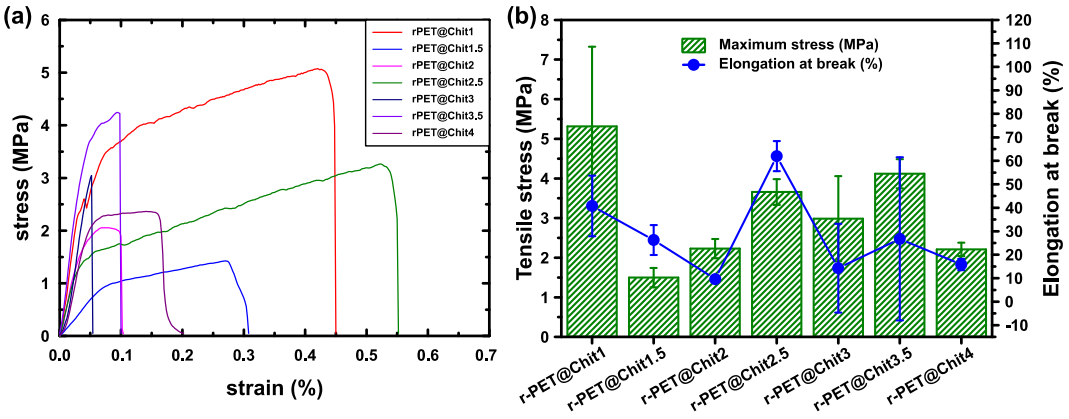

Fig. 5.8 (a) Strain-stress curves of the tested membranes and (b) the values of the maximum stress tolerated by each sample and the elongation at break for different chitosan concentration

5.4 Functionalization

In this Section, the functional properties of interest for this study were investigated. For practical reasons, only the r-PET@Chit2 membrane was used as a sample for these measurements, apart from the contact angle. The main reason for this choice is that the amount of chitosan on this fibrous mat – which is the main parameter that affects the following properties – is pretty much the same as the one for the higher concentrations of chitosan in solution. Moreover, this membrane shows the greater couple of underwater oil (UWO) and underoil water (UOW) contact angles for the hexane.

First of all, the amphiphilic property of the membrane was confirmed by measuring the water and oil contact angels for four different types of oils: two light (kerosene and hexane) and two heavy (carbon tetrachloride and tetrachloroethylene). Besides, the UWO and the UOW contact angle was determined for all the different concentrations of chitosan using the hexane. Finally, the test was repeated on the r-PET@Chit2 using the other three solvents.

The intrusion pressure of the membrane for the different types of oil was then measured to evaluate the capacity of the sample in retaining the selected liquid at higher pressure.

Moreover, the filtration tests were performed both using a simple mixture of oil and water, and an emulsion of them. The filtration efficiency and the filtrated liquid flux ware so measured.

5.4.1 Contact angle

In order to comprehend the effect of the chitosan on the properties of the surface of the membrane, the contact angle analysis was conducted on all the samples. It is well known that the r-PET presents hydrophobic and oleophilic properties. Still, it is also expected that the high roughness of the fibrous mats enhanced these

properties obtaining in this way an increase in water contact angle (Section 2.1). As reported in Fig. 5.9a, the as-spun r-PET follows the main literature showing a water contact angle of 134.0° and absorbing the oil droplet of different types of solvents. On the other hand, the functionalization made by the chitosan was effective; in fact, for each concentration of the biopolymer, the samples resulted amphiphilic.

Moreover, the underwater oil contact angle of the as-spun r-PET is 0° for the hexane, because the fibers were not wetted by the water so that the organic solvent could pass through (Fig. 2.4b). However, in the presence of the chitosan, the UWO CA increase significantly, becoming higher than 157° Fig. 5.9b. So, it is possible to define such membranes as underwater superoleophobic. Analogous considerations can be done for the underoil analysis. In this case, the underoil superhydrophobicity was slightly enhanced by the presence of the biopolymer. In fact, the UOW CA for the as-spun r-PET is 154°, while the same angle for the functionalized mats is always higher than 157°.

The r-PET@Chit2 membrane seems to be the one with the better wettability properties because it showed both high and constant CA values (168° for both UWO and UOW contact angle). For this reason, this sample was used to investigate the influence of the solvent on the solvent repulsion. Fig. 5.9c showed the underoil water and underwater oil CA for four different types of heavy and light oils. The results of the measurement evidenced substantial independence of the contact angle from the kind of solvent used.

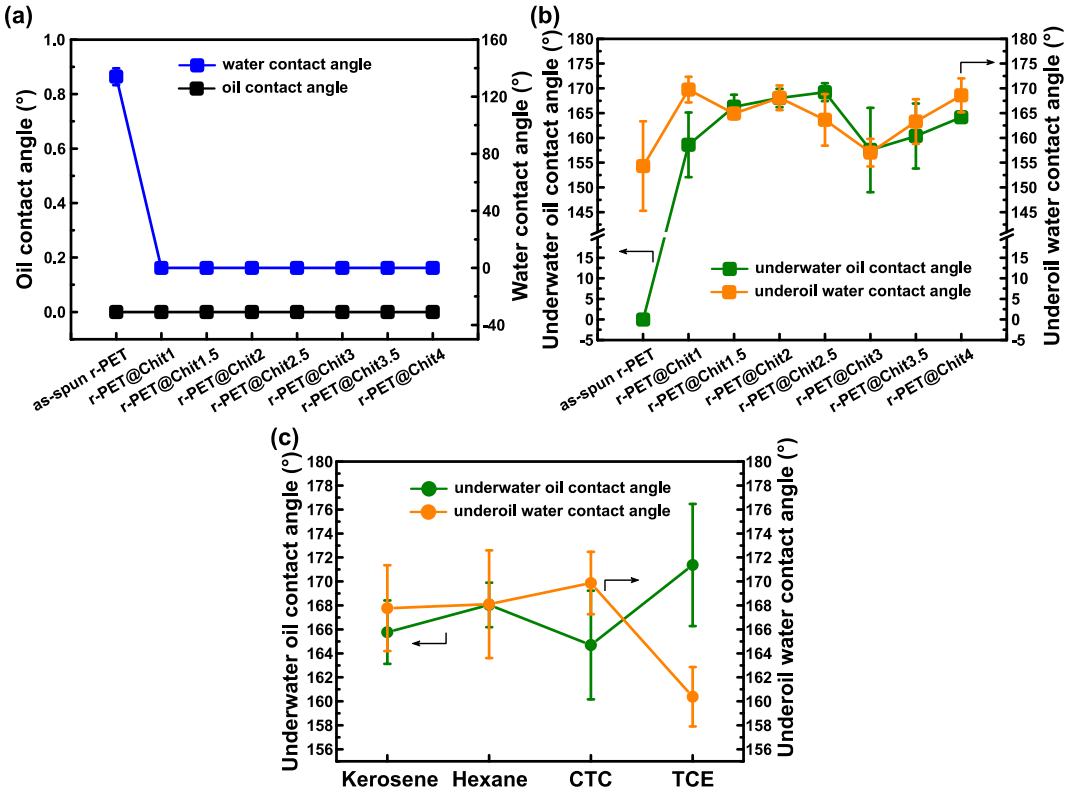

Fig. 5.9 (a) Water and oil contact angles in air and (b) underwater oil and underoilwater contact angles for all the sample. (c) Underoil water and underoil water contact angles of r-PET@Chit2 measured for four different kind of oils.

5.4.2 Intrusion pressure

The intrusion pressure measures the amount of pressure that the membrane can support without losing the retained liquid. The procedure adopted to measure this parameter was already presented in Section 4.4.8. For the light oils, the results were 45.3 ± 1.0 kPa and 47.7 ± 0.5 kPa, respectively, with the hexane and the kerosene (Fig. 5.10). However, for the carbon tetrachloride and the tetrachloroethylene, the intrusion pressure was 18.3 ± 0.5 kPa and 23.6 ± 3.0 kPa. The difference in the oil and the water intrusion pressure could be explained by the fact that the membrane contains a lot of hydrophilic groups (the chitosan content on the surface is higher

than the expected as previously said in Section 5.2.2) which may favor the substitution of the attached oil with the water on the fibers. As previously discussed in Section 2.1, the presence of a liquid with a good affinity on the surface of the fibers determines low contact angles, and consequently, the loss of the filtration properties.

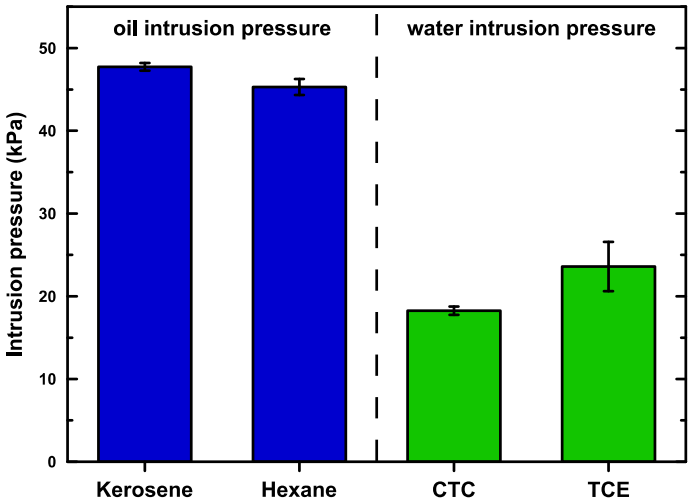

Fig. 5.10 Intrusion pressure values on the 2.0/8 membrane with for different kind of oils: kerosene, hexane, carbon tetrachloride and tetrachloroethylene.

5.4.3 Filtration performances

Finally, the ability of the design membrane r-PET@Chit2 both in the simple oil-water mixtures and emulsions separation was investigated. Two principal parameters were evaluated during the test: the flux of the liquid through the filter and the separation efficiency. Again, during this investigation, four different types of oils were tested (kerosene, hexane, CTC, and TCE).

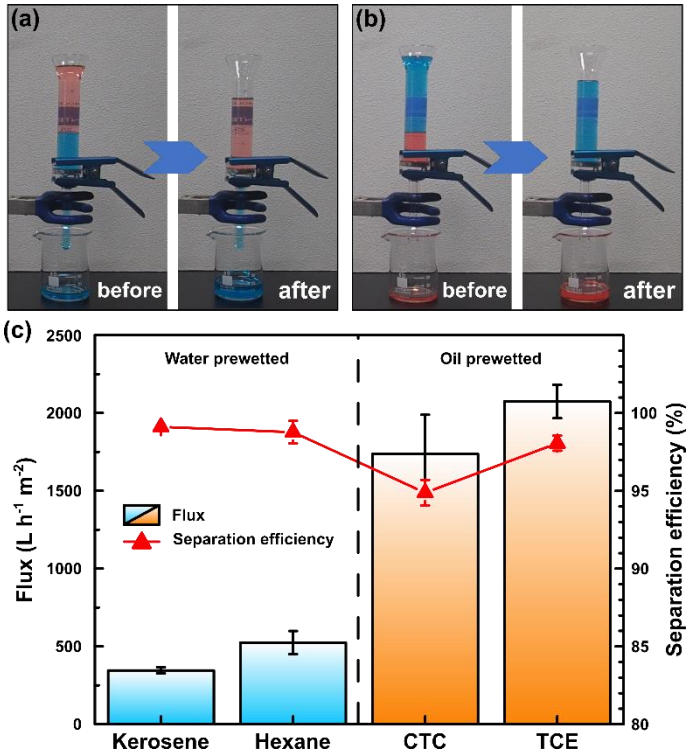

Fig. 5.11. Mixture separation of (a) heavy and (b) light oils at the beginning and the end of the process. (c) Flux and separation efficiency of mixture separation.

First of all, the mixture separation was performed, as previously explained in Section 4.4.9. The flux (J) was determined by weighing the collected liquid after the filtration and using the following equation:

$$J = \frac{m}{t \rho A} \tag{5.7}$$

where m is the mass of the filtered product, t is the collecting time, ρ is the density of the weighted liquid, and A is the area of the filter. It results in relatively low flux for all the combinations of light and heavy oil tested (Fig. 5.11c). In particular, the water separation from light oils showed the worst values, 346 ± 20 L h^{-1} m^{-2} for the kerosene/water mixture and 525 ± 75 L h^{-1} m^{-2} for the hexane/water mixture. This phenomenon could be attributed to the higher affinity of the membrane with water compared to oils, as already experienced with the intrusion pressure.

The efficiency was then measured as the fraction of liquid that is successfully filtrated. So, it was calculated as:

$$\eta_m = \frac{m_f}{m_0} \times 100\% \tag{5.8}$$

where η_m is the separation efficiency, m_f the mass of the filtrated liquid, and m_0 the mass of the liquid before filtration. The collected data are summarized in Fig. 5.11c and showed high values of η_m, higher than 95%. In particular, the best separation efficiency was reached with the kerosene/water mixture, equal to 99.1%. Compared with other sustainable amphiphilic membranes for oil-water mixture separation (Table 5.5) the fluxes resulted higher, although the efficiencies remain competitive. The large difference in the oils and water fluxes is probably due to the difference in viscosity of the liquids. As shown in Table 5.7 the water has higher viscosity respect to the heavy oils. In addition, the density of the heavy oil/water mixtures is greater than the other two mixtures, so that in the first case the liquid is more pushed to flow into the pores.

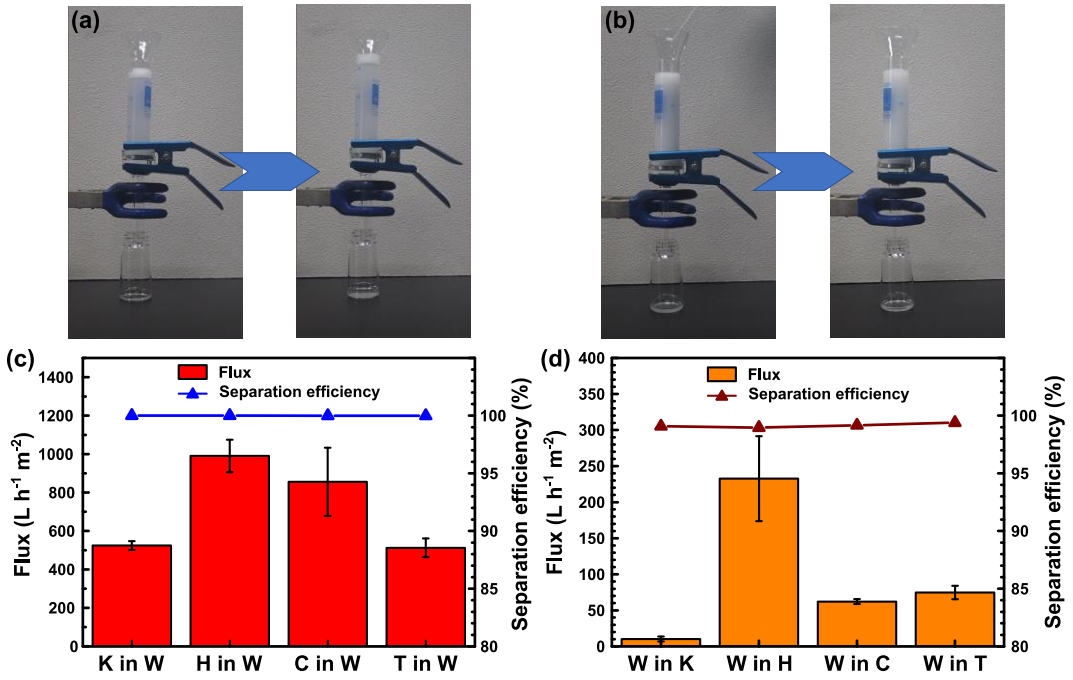

Fig. 5.12. The setup used for the emulsion separation is showed by the pictures of oil-in-water (a) and water-in-oil (b) emulsions, at the beginning of the filtration and after a couple of minutes. The flux and the efficiency measured in (c) oil in water emulsion and (d) water in oil emulsion are here reported.

Furthermore, the capacity of the membrane to retain also small baubles of liquid was investigated with the emulsion separation. In Section 4.4.9 it was explained the procedure adopted for the preparation of the

equipment for the test. The used emulsions had a range of particle size of c.a. 100-5700 nm for the water in oil and 19-8700 nm for the oil in water (Fig. 5.13). The filtration was so performed, and, again, the flux and the efficiency were calculated. The first parameter was measured by weighing the filtered liquid after 1 min and using again Equation 5.7. It was found that the rate of separation in the case of oil in water emulsion is higher than the one measured for the water in oil one. The higher value of the flux was measured with the CTC in water emulsion and is equal to 2027 ± 210 L h^{-1} m^{-2} (Fig. 5.12c-d).

On the other hand, this time, the efficiency of the membrane (η_e) was determined on the basis of the amount of the emulsified component in the filtration product. In particular, it was calculated by:

$$\eta_e = \frac{C_i - C_f}{C_i} \times 100\% \tag{5.9}$$

where C_i and C_f are the emulsion concentration before and after the filtration, respectively. For all the tested emulsions C_i is equal to 1wt%. The Karl-Fisher measurements established the amount of water in the oil emulsions, and it was used to estimate the separation efficiency. It was so found that in the filtration feed, the amount of water is lower than 117 ppm, for a separation efficiency > 99.0%. Moreover, the GC showed a concentration of oil in water after the filtration smaller than 1 ppm for efficiencies > 99.99%. For this reason, from the DLS measurements and the optical microscope images of the filtrated emulsions, nothing was detected (Fig. 5.13). Respect to other membranes for on-demand oil-water emulsion separation (Table 5.6), the filter of our design presented relatively low fluxes, while the efficiency is one of the higher. The main advantage, in this case, is the choice of the materials of the membranes, which makes the membrane here presented a sustainable solution for both mixtures and emulsion separation. Also in this case the fluctuation in the oil emulsion fluxes can be reconducted to the difference in the liquid viscosity. In fact, the hexane is the liquid with the lower viscosity, which is almost six time lower respect to the one of the kerosene (Table 5.7).

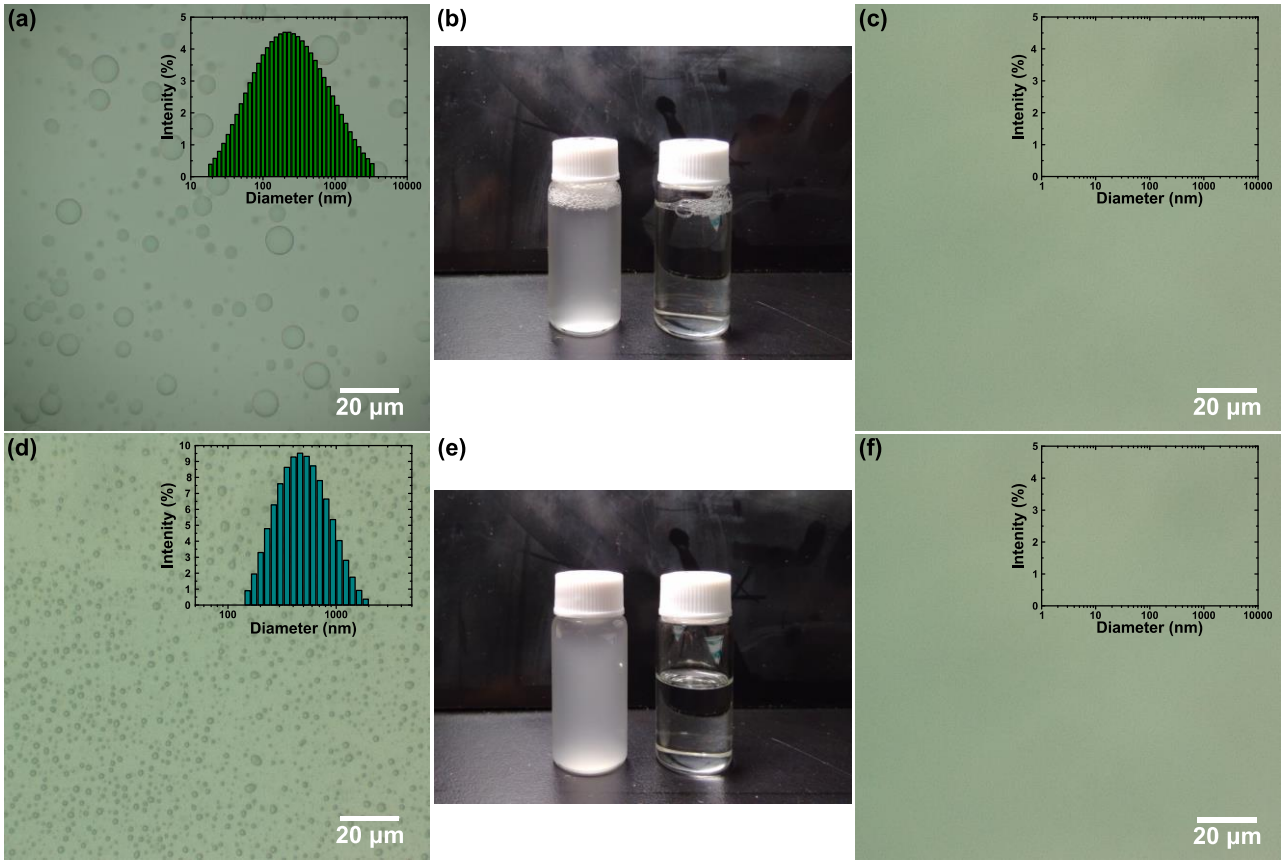

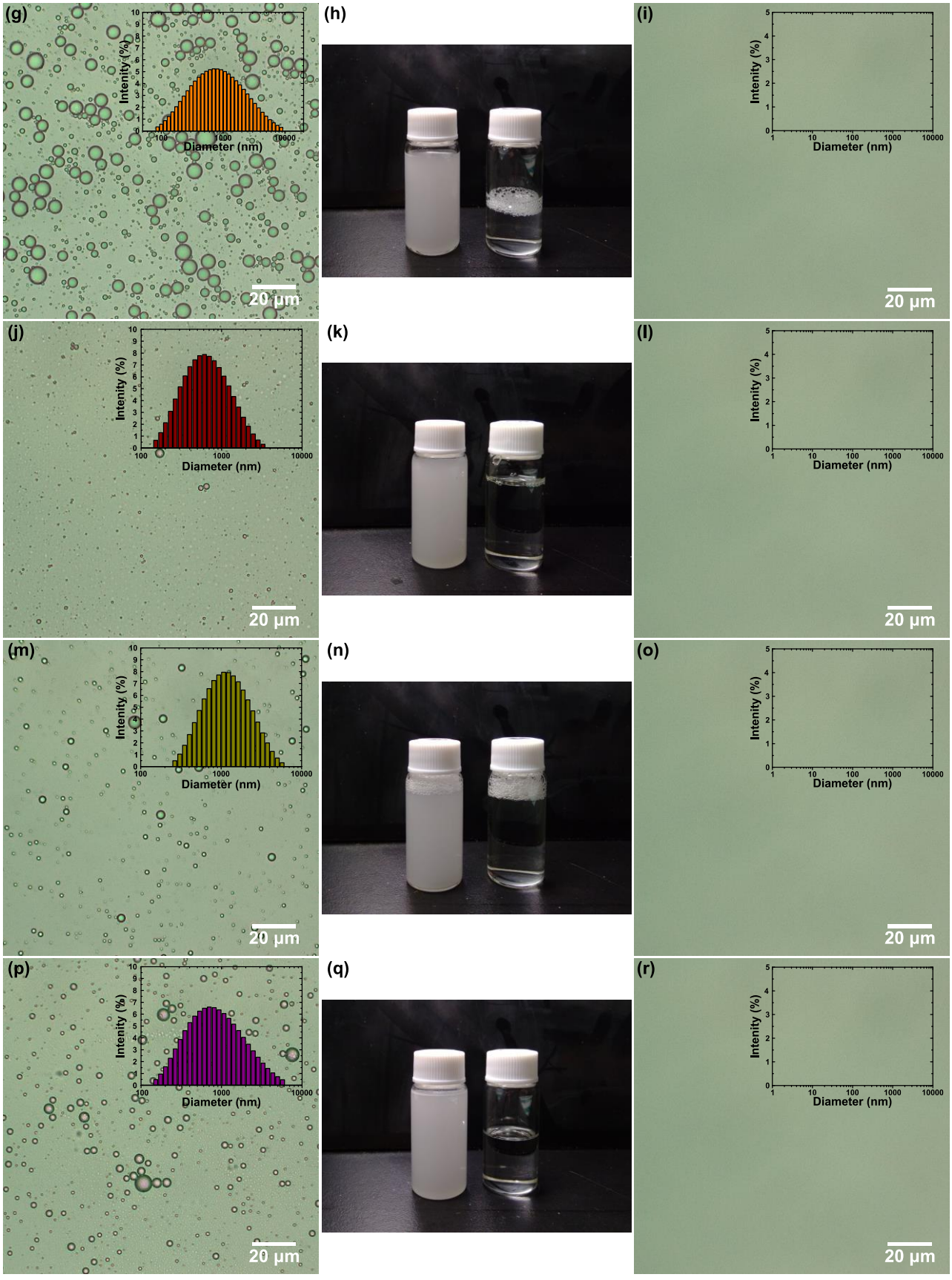
(g)
(h)
(i)
(j)
(k)
(l)
(m)
(n)
(o)
(p)
(q)
(r)
Intenity (%)
Diameter (nm)
20 μm

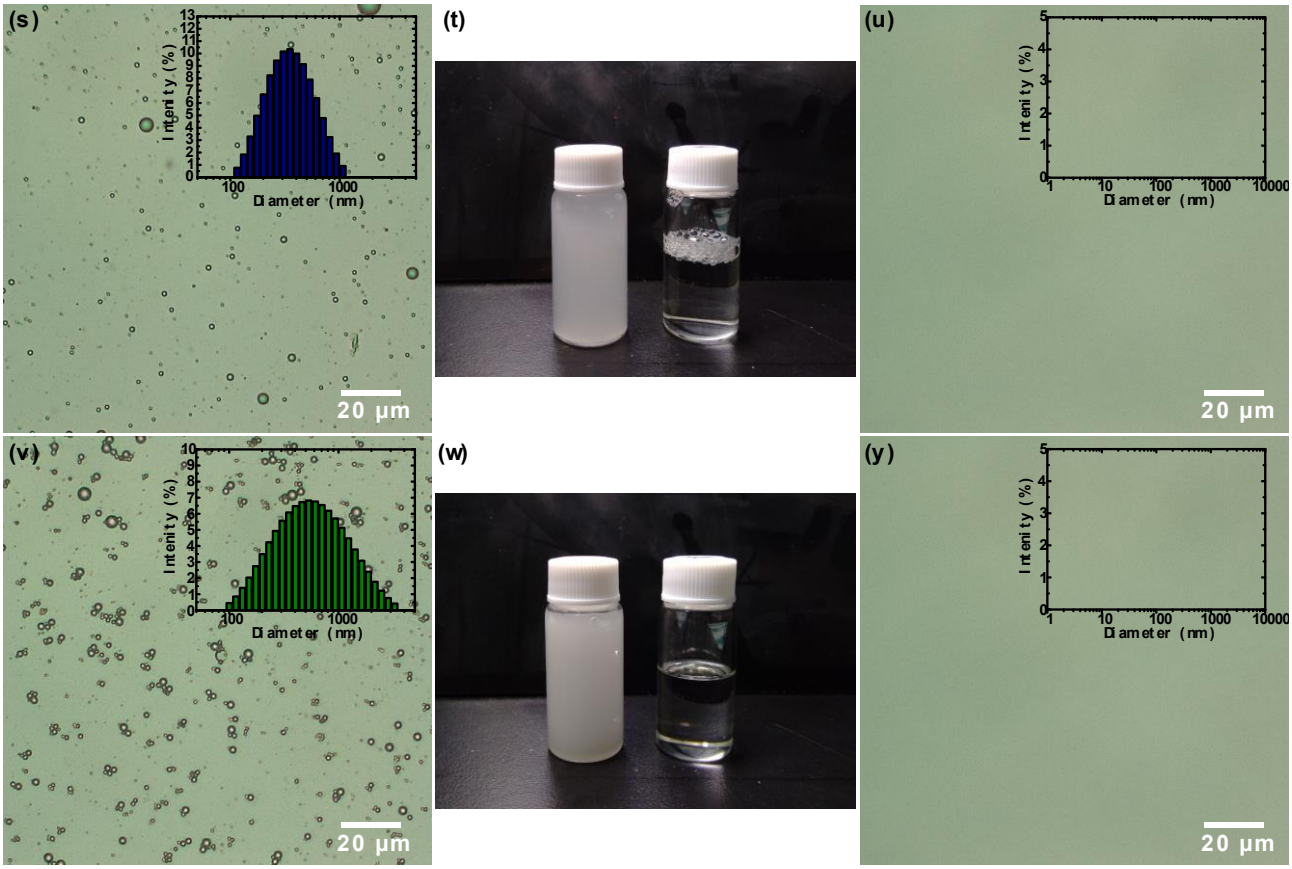

Fig. 5.13. Here are collected the optical microscope images of (a, g, m, s) oil in water and (d, j, p, v) water in oil emulsions togheter with the corriponding DLS signal. These results are compared with the same analysis operated on the filtrated emulsion (c, f, i, l, o, r, u, y). For completeness, the pictures of the emulsions pre and post filtration are also shown (b, e, h, k, n, q, t, w).

Table 5.5. Comparison between the oil-water mixtures separation performances of different amphiphilic membranes with the nanofibrous filter of our design.

Sample	Oil-water mixture	Flux (L m^{-2} h^{-1})	Separation efficiency (%)	Reference
Corn cub powders coated meshes	Hexane-water	4	> 99.9	[12]
	Dichloromethane-water	6	> 99.9	
Waste potato residue coated mesh	Kerosene-water	7	98.5	[10]
	Chloroform-water	9	98	
Waste cigarette filter nanofibrous membranes	Kerosene-water	1000	> 99.9	[24]
	Trichloromethane-water	1300	> 99.9	
rPET@Chitosan nanofibrous membrane	Hexane-water	524 ± 75	98.8	This work
	Tetrachloroethylene-water	2074 ± 107	98.1	

Table 5.6. Comparison between the oil-water emulsion separation performances of different amphiphilic membranes with the nanofibrous filter of our design.

Sample	Oil-water emulsion	Flux (L m^{-2} h^{-1})		Separation efficiency (%)		Reference
		Oil in water	Water in oil	Oil in water	Water in oil	
Carbon black-coated membrane	Hexane-water	3500	6500	99.9	99.7	[9]
Fluorinated silica nanoparticles coated paper towel	Hexadecane-water	4480	—	99.9	—	[181]
Waste cigarette filter nanofibrous membranes	Kerosene-water	100	150	99.4	99.7	[24]
rPET@Chitosan nanofibrous membrane	Hexane-water	991 ± 84	233 ± 59	99.9	98.9	This work

Table 5.7. Values of the viscosity and density for the different liquids used in the filtration tests.

Liquid	Viscosity [mPa s]	Density [g/cm^3]
water	1.00 [182]	0.99 [182]
kerosene	1.92 [182]	0.79 [183]
hexane	0.31 [184]	0.66 [185]
carbon tetrachloride	0.89 [186]	1.62 [187]
tetrachloroethylene	0.97 [186]	1.59 [188]

6 Conclusion

In the present work, the recycled PET and the chitosan have been used to design low-cost, sustainable, and efficient fibrous membranes for the oil/water separation. The selected technique for the synthesis of the fibers was the electrospinning, a cost-effective and straightforward technology wildly use in this research field. In particular, the study focused on the influence that the chitosan concentration in the blend has on the main properties of the separation membrane. To do that, at first, the parameters for good electrospinning have been set, and the fibrous mats are successfully prepared.

The morphological analysis from FE-SEM and laser microscope have shown that the obtained membranes possessed almost easy controllable shape and dimension. In fact, from the collected pictures, it can be observed that an increase in the polymer content usually leads to an increasing in the yarn roughness. It is known that this property has a significant influence on the separation performances; for this reason, the possibility of having good control over it is of particular interest.

The chemical composition of the fibers, especially of their surface, also represents an influent parameter concerning the ability of the membrane to perform the task for which it was designed. It was so found that the as-spun layers needed further treatment to eliminate all the residual traces of the used solvent. FT-IR and XPS analysis, in fact, have shown the presence of undesired salts of TFA, which could pollute the filtered water and contribute actively to the partial dissolution of the chitosan in water. For this reason, the membranes have been immersed in a supersaturated solution of sodium hydrogen carbonate and successfully neutralized. It was also found that the chitosan tends to concentrate more on the surface of the electrospun fibers than in their core. This fact favors the functionalization of the membranes and helps to obtain the predicted wettability.

The mechanical test has demonstrated important difficulties in controlling precisely the stability of the prepared filter. However, the measured maximum elongation stress and the elongation at break results to be promising respect to similar membranes.

The wettability analysis was conducted on the membranes with different concentrations of chitosan, and all of them have shown the amphiphilic properties that are requested in prewetted selective separation. In fact, the simultaneous hydro- and oleophilicity in a porous surface leads to underwater superoleophobicity and underoil superhydrophobicity because of the absorption of the surrounded liquid. The designed membranes have maintained high underliquid contact angles (> 150°) also for different types of heavy and light oils. This behavior suggests that similar performances could be obtained with many other solvents.

Finally, the capacity of the membrane in oil/water separation has been investigated. One of the principal drawbacks of such as filtration membrane is usually the weak resistance to separation failures. However, the object of this study has found to possess relatively high values of intrusion pressure, especially for what concerns oil retention, which resists under over 45 kPa of applied pressure. Moreover, the membrane has also shown interesting filtration performances for both oil/water mixtures and emulsions. In particular, it has been found that the filters possess high efficiency, over 95% for the simple mixtures, and 99.99% for light or heavy oil/water emulsions with a bubble size between a few tens of nanometers to some microns. The principal drawback of the designed membrane can be found in the low flux through the fibers of the filtrated liquid. This parameter could be adjusted by controlling the pore size of the filter, as evident from Equation 5.7. Anyway, it was already explained (Section 2.2) that the dimension of the porosity also affects the intrusion pressure values; for this reason, a better compromise between these two parameters could be found in a future study.

It is possible to conclude that the main aim of this work has been reached, designing a low-cost and sustainable membrane for selective oil/water separation of mixtures and emulsions. The membrane seems to have promising filtration performances with its high efficiency and capacity to withstand high pressures.

Further studies could be carried out in the future to enhance the filtration rate, which is a key parameter in the practical application of this membrane. Besides, it could be useful to understand better how to control more precisely the mechanical properties. Finally, in order to increase further the sustainability of the production process, it could be interesting to substitute at least part of the TFA as the solvent used, for example, with dichloromethane.

References

[1] A. Jernelöv, "How to defend against future oil spills," *Nature*, vol. 466, no. 7303, pp. 182–183, 2010.

[2] United Nations, "Executive Summary - Wastewater The Untapped Resource," 2017.

[3] J. Lehmköster, T. Schröder, and D. Ladischensky, "Oil and gas from the sea," *World Ocean Rev.*, p. 47, 2012.

[4] National Research Council, *Oil in the Sea III: Inputs, Fates, and Effects*. 2003.

[5] American Petroleum Institue, "Monographs on Refinery Environmental Control- Management of Water Discharges - Design and Operation of Oil-Water Separators," *Api Publ.*, pp. 1–5, 1990.

[6] K. T. Klasson, P. A. Taylor, J. F. Walker, et al., "Investigation of a centrifugal separator for in-well oil water separation," *Pet. Sci. Technol.*, vol. 22, no. 9–10, pp. 1143–1159, 2004.

[7] Z. shan Bai, H. lin Wang, and S. T. Tu, "Oil-water separation using hydrocyclones enhanced by air bubbles," *Chem. Eng. Res. Des.*, 2011.

[8] T. Frising, C. Noïk, and C. Dalmazzone, "The liquid/liquid sedimentation process: From droplet coalescence to technologically enhanced water/oil emulsion gravity separators: A review," *Journal of Dispersion Science and Technology*. 2006.

[9] G. Cao, Y. Wang, C. Wang, and S.-H. Ho, "A dually prewetted membrane for continuous filtration of water-in-light oil, oil-in-water, and water-in-heavy oil multiphase emulsion mixtures," *J. Mater. Chem. A*, pp. 11305–11313, 2019.

[10] J. Li, D. Li, Y. Yang, et al., "A prewetting induced underwater superoleophobic or underoil (super) hydrophobic waste potato residue-coated mesh for selective efficient oil/water separation," *Green Chem.*, vol. 18, no. 2, pp. 541–549, 2016.

[11] L. Liu, J. Lei, L. Li, et al., "A facile method to fabricate the superhydrophobic magnetic sponge for oil-water separation," *Mater. Lett.*, vol. 195, pp. 66–70, 2017.

[12] J. Li, X. Bai, X. Tang, et al., "Underwater superoleophobic/underoil superhydrophobic corn cob coated meshes for on-demand oil/water separation," *Sep. Purif. Technol.*, vol. 195, no. December 2017, pp. 232–237, 2018.

[13] X. Du, S. You, X. Wang, Q. Wang, and J. Lu, "Switchable and simultaneous oil/water separation induced by prewetting with a superamphiphilic self-cleaning mesh," *Chem. Eng. J.*, vol. 313, pp. 398–403, 2017.

[14] G. Kwon, A. K. Kota, Y. Li, et al., "On-demand separation of oil-water mixtures," *Adv. Mater.*, vol. 24, no. 27, pp. 3666–3671, 2012.

[15] H. N. Doan, D. K. Nguyen, P. P. Vo, et al., "Facile and Scalable Fabrication of Porous Polystyrene Fibers for Oil Removal by Centrifugal Spinning," *ACS Omega*, vol. 4, p. acsomega.9b02091, 2019.

[16] W. Ma, Q. Zhang, D. Hua, et al., "Electrospun fibers for oil-water separation," *RSC Adv.*, vol. 6, no. 16, pp. 12868–12884, 2016.

[17] F. Ejaz Ahmed, B. S. Lalia, N. Hilal, and R. Hashaikeh, "Underwater superoleophobic cellulose/electrospun PVDF-HFP membranes for efficient oil/water separation," *Desalination*, 2014.

[18] J. J. Li, L. T. Zhu, and Z. H. Luo, "Electrospun fibrous membrane with enhanced swithchable oil/water wettability for oily water separation," *Chem. Eng. J.*, 2016.

[19] M. Obaid, N. A. M. Barakat, O. A. Fadali, et al., "Effective and reusable oil/water separation membranes based on modified polysulfone electrospun nanofiber mats," *Chem. Eng. J.*, 2015.

[20] W. Ma, Z. Guo, J. Zhao, et al., "Polyimide/cellulose acetate core/shell electrospun fibrous membranes for oil-water separation," *Sep. Purif. Technol.*, 2017.

[21] J. Lin, B. Ding, J. Yang, J. Yu, and G. Sun, "Subtle regulation of the micro- and nanostructures of electrospun polystyrene fibers and their application in oil absorption," *Nanoscale*, 2012.

[22] Z. Jiang, L. D. Tijing, A. Amarjargal, et al., "Removal of oil from water using magnetic bicomponent composite nanofibers fabricated by electrospinning," *Compos. Part B Eng.*, 2015.

[23] W. Fang, L. Liu, T. Li, et al., "Electrospun N-Substituted Polyurethane Membranes with Self-Healing Ability for Self-Cleaning and Oil/Water Separation," *Chem. - A Eur. J.*, 2016.

[24] W. Liu, M. Cui, Y. Shen, et al., "Waste cigarette filter as nanofibrous membranes for on-demand immiscible oil/water mixtures and emulsions separation," *J. Colloid Interface Sci.*, vol. 549, pp. 114–122, 2019.

[25] P. K. Sow, Ishita, and R. Singhal, "Sustainable approach to recycle waste polystyrene to high-value

submicron fibers using solution blow spinning and application towards oil-water separation," *J. Environ. Chem. Eng.*, vol. 8, no. 2, p. 102786, 2020.
[26] M. Shioya and T. Kikutani, "Synthetic Textile Fibres," *Text. Fash.*, no. January, pp. 139–155, 2015.
[27] L. Bartolome, M. Imran, B. G. Cho, W. A. Al-masry, and D. H. Kim, "Recent developments in PET recycling," *Mater. Recycl. - Trends Perspect.*, pp. 65–84, 2012.
[28] B. Geyer, G. Lorenz, and A. Kandelbauer, "Recycling of poly(ethylene terephthalate) – A review focusing on chemical methods," *Express Polym. Lett.*, vol. 10, no. 7, pp. 559–586, 2016.
[29] N. Malesic-Eleftheriadou, E. Evgenidou, G. Z. Kyzas, D. N. Bikiaris, and D. A. Lambropoulou, "Removal of antibiotics in aqueous media by using new synthesized bio-based poly(ethylene terephthalate)-TiO2 photocatalysts," *Chemosphere*, 2019.
[30] A. M. Atta, M. E. Abdel-Raouf, S. M. Elsaeed, and A. A. A. Abdel-Azim, "Curable resins based on recycled poly(ethylene terephthalate) for coating applications," *Prog. Org. Coatings*, 2006.
[31] A. R. Ajitha, M. K. Aswathi, and P. Manju, "Applications of Waste Poly(Ethylene Terephthalate) Bottles," *Recycl. Polyethyl. Terephthalate Bottles*, pp. 169–189, Jan. 2019.
[32] N. E. Zander, M. Gillan, and D. Sweetser, "Recycled PET nanofibers for water filtration applications," *Materials (Basel).*, vol. 9, no. 4, pp. 1–10, 2016.
[33] H. N. Doan, P. Phong Vo, K. Hayashi, et al., "Recycled PET as a PDMS-Functionalized electrospun fibrous membrane for oil-water separation," *J. Environ. Chem. Eng.*, vol. 8, no. 4, p. 103921, 2020.
[34] Y. Wang, C. Lai, H. Hu, et al., "Temperature-responsive nanofibers for controllable oil/water separation," *RSC Adv.*, 2015.
[35] J. J. Li, Y. N. Zhou, and Z. H. Luo, "Smart Fiber Membrane for pH-Induced Oil/Water Separation," *ACS Appl. Mater. Interfaces*, 2015.
[36] Y. Wang, C. Lai, X. Wang, et al., "Beads-on-String Structured Nanofibers for Smart and Reversible Oil/Water Separation with Outstanding Antifouling Property," *ACS Appl. Mater. Interfaces*, 2016.
[37] L. Xu, N. Liu, Y. Cao, et al., "Mercury ion responsive wettability and oil/water separation," *ACS Appl. Mater. Interfaces*, 2014.
[38] X. Du, S. You, X. Wang, Q. Wang, and J. Lu, "Switchable and simultaneous oil/water separation induced by prewetting with a superamphiphilic self-cleaning mesh," *Chem. Eng. J.*, vol. 313, pp. 398–403, 2017.
[39] P. Sangsanoh and P. Supaphol, "Stability improvement of electrospun chitosan nanofibrous membranes in neutral or weak basic aqueous solutions," *Biomacromolecules*, vol. 7, no. 10, pp. 2710–2714, 2006.
[40] L. Wen, Y. Tian, and L. Jiang, "Bioinspired super-wettability from fundamental research to practical applications," *Angew. Chemie - Int. Ed.*, vol. 54, no. 11, pp. 3387–3399, 2015.
[41] J. Almodóvar and M. J. Kipper, "Coating Electrospun Chitosan Nanofibers with Polyelectrolyte Multilayers Using the Polysaccharides Heparin and N,N,N-Trimethyl Chitosan," *Macromol. Biosci.*, vol. 11, no. 1, pp. 72–76, 2011.
[42] M. Hasegawa, A. Isogai, F. Onabe, and M. Usuda, "Dissolving states of cellulose and chitosan in trifluoroacetic acid," *J. Appl. Polym. Sci.*, vol. 45, no. 10, pp. 1857–1863, 1992.
[43] K. H. Jung, M. W. Huh, W. Meng, et al., "Preparation and antibacterial activity of PET/chitosan nanofibrous mats using an electrospinning technique," *J. Appl. Polym. Sci.*, 2007.
[44] Z. Zhu, W. Wang, D. Qi, et al., "Calcinable Polymer Membrane with Revivability for Efficient Oily-Water Remediation," *Adv. Mater.*, vol. 30, no. 30, 2018.
[45] J. A. Lopes-da-Silva, B. Veleirinho, and I. Delgadillo, "Preparation and characterization of electrospun mats made of PET/chitosan hybrid nanofibers," *J. Nanosci. Nanotechnol.*, vol. 9, no. 6, pp. 3798–3804, 2009.
[46] J. Ge, D. Zong, Q. Jin, J. Yu, and B. Ding, "Biomimetic and Superwettable Nanofibrous Skins for Highly Efficient Separation of Oil-in-Water Emulsions," *Adv. Funct. Mater.*, 2018.
[47] C. Chen, D. Weng, A. Mahmood, S. Chen, and J. Wang, "Separation Mechanism and Construction of Surfaces with Special Wettability for Oil/Water Separation," *ACS Appl. Mater. Interfaces*, 2019.
[48] Herodotus, Baloe, and William, *Herodotus*. London, 1830.
[49] S. Dalvi, *Fundamentals of Oil & Gas Industries for Beginners*. 2015.
[50] D. Crespy, M. Bozonnet, and M. Meier, "100 Years of Bakelite, the material of a 1000 uses," *Angewandte Chemie - International Edition*. 2008.
[51] H. Bautista and K. M. M. Rahman, "Review on the Sundarbans Delta Oil Spill: Effects on Wildlife and Habitats," *Международный научно-исследовательский журнал*, vol. 1 (43) Par, pp. 93–96, 2016.

[52] G. M. Tehrani, S. B. Tavakoly Sany, R. Hashim, and A. Salleh, “Predictive environmental impact assessment of total petroleum hydrocarbons in petrochemical wastewater effluent and surface sediment,” *Environ. Earth Sci.*, 2016.
[53] J. M. Teal and R. W. Howarth, “Oil spill studies: A review of ecological effects,” *Environ. Manage.*, vol. 8, no. 1, pp. 27–43, 1984.
[54] M. Afenyo and F. Khan, “Assessing the risk of potential oil spills in the Arctic due to shipping,” *Marit. Transp. Reg. Sustain.*, pp. 179–193, Jan. 2020.
[55] D. Kukkar, A. Rani, V. Kumar, et al., “Recent advances in carbon nanotube sponge–based sorption technologies for mitigation of marine oil spills,” *J. Colloid Interface Sci.*, vol. 570, pp. 411–422, Jun. 2020.
[56] M. de O. Soares, C. E. P. Teixeira, L. E. A. Bezerra, et al., “Oil spill in South Atlantic (Brazil): Environmental and governmental disaster,” *Mar. Policy*, vol. 115, p. 103879, May 2020.
[57] R. D. Wilson, P. H. Monaghan, A. Osanik, L. C. Price, and M. A. Rogers, “Natural marine oil seepage,” *Science (80-.).*, 1974.
[58] M. Fingas, “Introduction and the oil spill problem,” in *Oil Spill Science and Technology*, 2010, pp. 1–48.
[59] ITOPF, “Oil Tanker Spill Statistics 2019,” 2020.
[60] Kenry and C. T. Lim, “Nanofiber technology: current status and emerging developments,” *Prog. Polym. Sci.*, vol. 70, pp. 1–17, Jul. 2017.
[61] Y.-Z. Long, X. Yan, X.-X. Wang, J. Zhang, and M. Yu, *Electrospinning: The Setup and Procedure*. Elsevier Inc., 2019.
[62] A. Haider, S. Haider, and I. K. Kang, “A comprehensive review summarizing the effect of electrospinning parameters and potential applications of nanofibers in biomedical and biotechnology,” *Arabian Journal of Chemistry*, vol. 11, no. 8. Elsevier B.V., pp. 1165–1188, 01-Dec-2018.
[63] Y. Shi, J. Wei, S. Li, S. Peng, and B. Zhang, “Experimental study on containment of moderate-viscous oil by floating boom subject to waves and currents,” *Appl. Ocean Res.*, vol. 94, p. 102003, Jan. 2020.
[64] H. M. Brown, R. H. Goodman, C.-F. An, and J. Bittner, “Boom failure mechanisms: Comparison of channel experiments with computer modelling results,” *Spill Sci. Technol. Bull.*, vol. 3, no. 4, pp. 217–220, Jan. 1996.
[65] I. B. Ivshina, M. S. Kuyukina, A. V. Krivoruchko, et al., “Oil spill problems and sustainable response strategies through new technologies,” *Environmental Sciences: Processes and Impacts*. 2015.
[66] E. L. Schrader, “Remediation of floating, open water oil spills: Comparative efficacy of commercially available polypropylene sorbent booms,” *Environ. Geol. Water Sci.*, 1991.
[67] M. Fingas, “Physical Spill Countermeasures,” in *Oil Spill Science and Technology*, 2011.
[68] A. Bayat, S. F. Aghamiri, A. Moheb, and G. R. Vakili-Nezhaad, “Oil spill cleanup from sea water by sorbent materials,” *Chem. Eng. Technol.*, 2005.
[69] M. Toyoda and M. Inagaki, “Heavy oil sorption using exfoliated graphite: New application of exfoliated graphite to protect heavy oil pollution,” *Carbon N. Y.*, vol. 38, no. 2, pp. 199–210, Jan. 2000.
[70] H. -M Choi and J. P. Moreau, “Oil sorption behavior of various sorbents studied by sorption capacity measurement and environmental scanning electron microscopy,” *Microsc. Res. Tech.*, 1993.
[71] M. Inagaki, A. Kawahara, and H. Konno, “Sorption and recovery of heavy oils using carbonized fir fibers and recycling,” *Carbon N. Y.*, vol. 40, no. 1, pp. 105–111, Jan. 2002.
[72] Q. F. Wei, R. R. Mather, A. F. Fotheringham, and R. D. Yang, “Evaluation of nonwoven polypropylene oil sorbents in marine oil-spill recovery,” *Mar. Pollut. Bull.*, vol. 46, no. 6, pp. 780–783, Jun. 2003.
[73] M. Roulia, K. Chassapis, C. Fotinopoulos, T. Savvidis, and D. Katakis, “Dispersion and Sorption of Oil Spills by Emulsifier-Modified Expanded Perlite,” *Spill Sci. Technol. Bull.*, vol. 8, no. 5–6, pp. 425–431, Jan. 2003.
[74] M. Inagaki, A. Kawahara, Y. Nishi, and N. Iwashita, “Heavy oil sorption and recovery by using carbon fiber felts,” *Carbon N. Y.*, vol. 40, no. 9, pp. 1487–1492, Aug. 2002.
[75] H. Chapman, K. Purnell, R. J. Law, and M. F. Kirby, “The use of chemical dispersants to combat oil spills at sea: A review of practice and research needs in Europe,” *Mar. Pollut. Bull.*, vol. 54, no. 7, pp. 827–838, 2007.
[76] R. C. Prince, “Oil spill dispersants: Boon or bane?,” *Environ. Sci. Technol.*, 2015.
[77] M. F. Fingas, R. Stoodley, and N. Laroche, “Effectiveness testing of spill-treating agents,” *Oil Chem. Pollut.*, vol. 7, no. 4, pp. 337–348, Jan. 1990.

[78] M. Fingas, “Spill-Treating Agents,” in *Oil Spill Science and Technology*, Gulf Professional Publishing, 2011, pp. 429–433.
[79] F. L. Motta, S. R. Stoyanov, and J. B. P. Soares, “Application of solidifiers for oil spill containment: A review,” *Chemosphere*, vol. 194, pp. 837–846, Mar. 2018.
[80] R. M. Atlas, “Petroleum biodegradation and oil spill bioremediation,” *Mar. Pollut. Bull.*, vol. 31, no. 4–12, pp. 178–182, Apr. 1995.
[81] L. H. Hu, S. Liu, W. Peng, and R. Huo, “Experimental study on burning rates of square/rectangular gasoline and methanol pool fires under longitudinal air flow in a wind tunnel,” *J. Hazard. Mater.*, 2009.
[82] L. van Gelderen, N. L. Brogaard, M. X. Sørensen, et al., “Importance of the slick thickness for effective in-situ burning of crude oil,” *Fire Saf. J.*, vol. 78, pp. 1–9, Nov. 2015.
[83] M. Fingas, “An Overview of In-Situ Burning,” in *Oil Spill Science and Technology*, Gulf Professional Publishing, 2011, pp. 737–903.
[84] D. D. Evans, W. George, H. R. Baum, W. D. Walton, and B. Kevin, “In Situ Burning of Oil Spills,” vol. 106, no. 1, pp. 231–278, 2001.
[85] M. Fingas, “In-Situ Burning,” in *The Basics of Oil Spill Cleanup*, CRC Press, 2013, pp. 168–183.
[86] F. A. Osamor, *Oil/water separation: state-of-the-art*. Industrial Environmental Research Laboratory, Office of Research and Development, U.S. Environmental Protection Agency ;--for sale by the National Technical Information Service, 1978.
[87] U. Daiminger, W. Nitsch, P. Plucinski, and S. Hoffmann, “Novel techniques for oil/water separation,” *J. Memb. Sci.*, 1995.
[88] K. Jaji and M. Wash, “Treatment of oilfield produced water with dissolved air flotation,” *Dep. Civ. Resour. Eng.*, 2012.
[89] M. Fingas, “Separation, Pumping, Decontamination, and Disposal,” in *The Basics of Oil Spill Cleanup*, 2012, pp. 117–129.
[90] K. T. Klasson, P. A. Taylor, J. F. Walker, et al., “Modification of a centrifugal separator for in-well oil-water separation,” in *Separation Science and Technology*, 2005.
[91] N. Kharoua, L. Khezzar, and Z. Nemouchi, “Computational fluid dynamics study of the parameters affecting oil-water hydrocyclone performance,” *Proc. Inst. Mech. Eng. Part E J. Process Mech. Eng.*, 2010.
[92] J. Saththasivam, K. Loganathan, and S. Sarp, “An overview of oil-water separation using gas flotation systems,” *Chemosphere*. 2016.
[93] P. Barthe, M. Chaugny, S. Roudier, and L. D. Sancho, “Best Available Techniques (BAT) Reference Document for theRefining of Mineral Oil and Gas,” 2015.
[94] S. Jafarinejad, “6.4.3 Secondary Treatment,” in *Petroleum Waste Treatment and Pollution Control*, Elsevier, 2017, p. 196.
[95] R. N. Hazlett, “Fibrous bed coalescence of water: Steps in the Coalescence Process,” *Ind. Eng. Chem. Fundam.*, 1969.
[96] D. Hu, X. Li, L. Li, and C. Yang, “Designing high-caliber nonwoven filter mats for coalescence filtration of oil/water emulsions,” *Sep. Purif. Technol.*, 2015.
[97] C. Shin and G. G. Chase, “Water-in-Oil Coalescence in Micro-Nanofiber Composite Filters,” *AIChE J.*, 2004.
[98] J. Gutteter-Grudziński and A. Moraczewski, “Coalescence filtration of ship oil bilge water with an nonwoven fabric,” *Desalin. Water Treat.*, 2011.
[99] H. J. Tanudjaja, C. A. Hejase, V. V. Tarabara, A. G. Fane, and J. W. Chew, “Membrane-based separation for oily wastewater: A practical perspective,” *Water Research*. 2019.
[100] M. Han, J. Zhang, W. Chu, J. Chen, and G. Zhou, “Research Progress and prospects of marine Oily wastewater treatment: A review,” *Water (Switzerland)*. 2019.
[101] L. Yu, M. Han, and F. He, “A review of treating oily wastewater,” *Arabian Journal of Chemistry*. 2017.
[102] R. K. Gupta, G. J. Dunderdale, M. W. England, and A. Hozumi, “Oil/water separation techniques: A review of recent progresses and future directions,” *J. Mater. Chem. A*, vol. 5, no. 31, pp. 16025–16058, 2017.
[103] A. A. El-Samak, D. Ponnamma, M. K. Hassan, et al., “Designing Flexible and Porous Fibrous Membranes for Oil Water Separation—A Review of Recent Developments,” *Polymer Reviews*. 2020.
[104] T. Young, “III. An essay on the cohesion of fluids,” *Philos. Trans. R. Soc. London*, 1805.
[105] S. Wang and L. Jiang, “Definition of superhydrophobic states,” *Advanced Materials*. 2007.

[106] Y. Guan, F. Cheng, and Z. Pan, "Superwetting polymeric three dimensional (3D) porous materials for Oil/Water separation: A review," *Polymers (Basel).*, vol. 11, no. 5, 2019.
[107] A. B. D. Cassie and S. Baxter, "Wettability of porous surfaces," *Trans. Faraday Soc.*, vol. 40, no. 5, pp. 546–551, 1944.
[108] R. N. Wenzel, "Resistance of solid surfaces to wetting by water," *Ind. Eng. Chem.*, 1936.
[109] J. J. Li, Y. N. Zhou, and Z. H. Luo, "Polymeric materials with switchable superwettability for controllable oil/water separation: A comprehensive review," *Progress in Polymer Science*. 2018.
[110] J. Li, D. Li, Y. Yang, et al., "A prewetting induced underwater superoleophobic or underoil (super) hydrophobic waste potato residue-coated mesh for selective efficient oil/water separation," *Green Chem.*, vol. 18, no. 2, pp. 541–549, 2016.
[111] M. A. Gondal, M. S. Sadullah, M. A. Dastageer, et al., "Study of factors governing oil-water separation process using TiO 2 films prepared by spray deposition of nanoparticle dispersions," *ACS Appl. Mater. Interfaces*, 2014.
[112] D. Tian, X. Zhang, Y. Tian, et al., "Photo-induced water-oil separation based on switchable superhydrophobicity- superhydrophilicity and underwater superoleophobicity of the aligned ZnO nanorod array-coated mesh films," *J. Mater. Chem.*, 2012.
[113] N. Tucker, J. J. Stanger, M. P. Staiger, H. Razzaq, and K. Hofman, "The history of the science and technology of electrospinning from 1600 to 1995," *J. Eng. Fiber. Fabr.*, vol. 7, no. 3, pp. 63–73, 2012.
[114] J. Cooley, "Improved methods of and apparatus for electrically separating the relatively volatile liquid component from the component of relatively fixed substances of composite," GB 06385, 1900.
[115] G. R. Mitchell, "The Development of Electrospinning Technologies for Commercial Application," in *Electrospinning*, Mitchell,., The Royal Society of Chemitry, Ed. 2015, pp. 34–56.
[116] W. J. Morton, "Method of dispersing fluids," US Pat. 705, 691, 1902.
[117] J. Zeleny, "The electrical discharge from liquid points, and a hydrostatic method of measuring the electric intensity at their surfaces," *Phys. Rev.*, 1914.
[118] J. Zeleny, "Instability of electrified liquid surfaces," *Phys. Rev.*, 1917.
[119] A. Formhals, "Process and apparatus for preparing artificial threads," US Patent 1, 975, 504, 1934.
[120] G. I. Taylor, "Disintegration of water drops in an electric field," *Proc. R. Soc. London. Ser. A. Math. Phys. Sci.*, vol. 280, pp. 383–97, 1964.
[121] R. Halaui, E. Zussman, R. Khalfin, R. Semiat, and Y. Cohen, "Polymeric microtubes for water filtration by co-axial electrospinning technique," *Polym. Adv. Technol.*, 2017.
[122] Z. Cheng, J. Cao, L. Kang, et al., "Novel transparent nano-pattern window screen for effective air filtration by electrospinning," *Mater. Lett.*, 2018.
[123] X. H. Qin and S. Y. Wang, "Filtration properties of electrospinning nanofibers," *J. Appl. Polym. Sci.*, 2006.
[124] Q. Tian, N. Wu, B. Wang, and Y. Wang, "Fabrication of hollow SiC ultrafine fibers by single-nozzle electrospinning for high-temperature thermal insulation application," *Mater. Lett.*, 2019.
[125] I. D. Kim and A. Rothschild, "Nanostructured metal oxide gas sensors prepared by electrospinning," *Polymers for Advanced Technologies*. 2011.
[126] O. Landau and A. Rothschild, "Microstructure evolution of TiO 2 gas sensors produced by electrospinning," *Sensors Actuators, B Chem.*, 2012.
[127] S. Hong, M. Hou, H. Zhang, et al., "A high-performance PEM fuel cell with ultralow platinum electrode via electrospinning and underpotential deposition," *Electrochim. Acta*, 2017.
[128] S. H. Choi, D. Hwang, D. Y. Kim, et al., "Amorphous zinc stannate (Zn2SnO4) nanofibers networks as photoelectrodes for organic dye-sensitized solar cells," *Adv. Funct. Mater.*, 2013.
[129] J. Liang, L. T. Bu, W. G. Cao, T. Chen, and Y. C. Cao, "Facile fabrication of coaxial-cable like Mn2O3 nanofiber by electrospinning: Application as electrode material for supercapacitor," *J. Taiwan Inst. Chem. Eng.*, 2016.
[130] T. Maeda, K. Hagiwara, S. Yoshida, T. Hasebe, and A. Hotta, "Preparation and characterization of 2-methacryloyloxyethyl phosphorylcholine polymer nanofibers prepared via electrospinning for biomedical materials," *J. Appl. Polym. Sci.*, 2014.
[131] M. He, H. Jiang, R. Wang, Y. Xie, and C. Zhao, "Fabrication of metronidazole loaded poly (ε-caprolactone)/zein core/shell nanofiber membranes via coaxial electrospinning for guided tissue regeneration," *J. Colloid Interface Sci.*, 2017.
[132] K. A. Khalil, H. Fouad, T. Elsarnagawy, and F. N. Almajhdi, "Preparation and characterization of

electrospun PLGA/silver composite nanofibers for biomedical applications," *Int. J. Electrochem. Sci.*, 2013.
[133] D. Pisignano, "Electrospinning," in *Polymer Nanofibers - Building Blocks for Nanotechnology*, no. 29, Royal Society of Chemistry, 2013, pp. 50–131.
[134] "Electrically driven jets," *Proc. R. Soc. London. A. Math. Phys. Sci.*, 1969.
[135] A. L. Yarin, S. Koombhongse, and D. H. Reneker, "Taylor cone and jetting from liquid droplets in electrospinning of nanofibers," *J. Appl. Phys.*, 2001.
[136] J. H. He, Y. Wu, and W. W. Zuo, "Critical length of straight jet in electrospinning," *Polymer (Guildf).*, vol. 46, no. 26, pp. 12637–12640, 2005.
[137] D. H. Reneker and A. L. Yarin, "Electrospinning jets and polymer nanofibers," *Polymer (Guildf).*, vol. 49, no. 10, pp. 2387–2425, 2008.
[138] H. Fong, I. Chun, and D. H. Reneker, "Beaded nanofibers formed during electrospinning," in *Polymer*, 1999.
[139] W. Zuo, M. Zhu, W. Yang, et al., "Experimental study on relationship between jet instability and formation of beaded fibers during electrospinning," *Polym. Eng. Sci.*, 2005.
[140] G. R. Williams, B. T. Raimi-Abraham, and C. J. Luo, "Electrospinning fundamentals," *Nanofibres Drug Deliv.*, pp. 24–59, 2018.
[141] S. Koombhongse, W. Liu, and D. H. Reneker, "Flat polymer ribbons and other shapes by electrospinning," *J. Polym. Sci. Part B Polym. Phys.*, 2001.
[142] N. Bhardwaj and S. C. Kundu, "Electrospinning: A fascinating fiber fabrication technique," *Biotechnol. Adv.*, vol. 28, no. 3, pp. 325–347, 2010.
[143] A. S. Motamedi, H. Mirzadeh, F. Hajiesmaeilbaigi, S. Bagheri-Khoulenjani, and M. Shokrgozar, "Effect of electrospinning parameters on morphological properties of PVDF nanofibrous scaffolds," *Prog. Biomater.*, 2017.
[144] S. S. S. Bakar, K. C. Fong, A. Eleyas, and M. F. M. Nazeri, "Effect of Voltage and Flow Rate Electrospinning Parameters on Polyacrylonitrile Electrospun Fibers," in *IOP Conference Series: Materials Science and Engineering*, 2018.
[145] M. M. Demir, I. Yilgor, E. Yilgor, and B. Erman, "Electrospinning of polyurethane fibers," *Polymer (Guildf).*, 2002.
[146] H. Homayoni, S. A. H. Ravandi, and M. Valizadeh, "Electrospinning of chitosan nanofibers: Processing optimization," *Carbohydr. Polym.*, vol. 77, no. 3, pp. 656–661, 2009.
[147] B. Cramariuc, R. Cramariuc, R. Scarlet, L. Rozemarie, and I. G. Lupu, "Fiber diameter in electrospinning process," *J. Electrostat.*, vol. 71, no. 3, pp. 189–198, 2013.
[148] V. Pillay, C. Dott, Y. E. Choonara, et al., "A review of the effect of processing variables on the fabrication of electrospun nanofibers for drug delivery applications," *J. Nanomater.*, vol. 2013, 2013.
[149] H. Shao, J. Fang, H. Wang, and T. Lin, "Effect of electrospinning parameters and polymer concentrations on mechanical-to-electrical energy conversion of randomly-oriented electrospun poly(vinylidene fluoride) nanofiber mats," *RSC Adv.*, vol. 5, no. 19, pp. 14345–14350, 2015.
[150] J. M. Deitzel, J. Kleinmeyer, D. Harris, and N. C. Beck Tan, "The effect of processing variables on the morphology of electrospun nanofibers and textiles," *Polymer (Guildf).*, 2001.
[151] R. H. Colby, L. J. Fetters, W. G. Funk, and W. W. Graessley, "Effects of Concentration and Thermodynamic Interaction on the Viscoelastic Properties of Polymer Solutions," *Macromolecules*, 1991.
[152] M. G. McKee, G. L. Wilkes, R. H. Colby, and T. E. Long, "Correlations of Solution Rheology with Electrospun Fiber Formation of Linear and Branched Polyesters," *Macromolecules*, 2004.
[153] G. R. Mitchell, *Electrospinning: principles, practice and possibilities*. The Royal Society of Chemistry, 2015.
[154] P. K. Baumgarten, "Electrostatic spinning of acrylic microfibers," *J. Colloid Interface Sci.*, 1971.
[155] T. Lin and J. Fang, "Electrospinning," in *Fundamentals of Electrospinning & Electrospun Nanofibers*, DEStech Publications, 2017, pp. 25–66.
[156] L. Huang, N. N. Bui, S. S. Manickam, and J. R. McCutcheon, "Controlling electrospun nanofiber morphology and mechanical properties using humidity," *J. Polym. Sci. Part B Polym. Phys.*, 2011.
[157] S. A. Theron, A. L. Yarin, E. Zussman, and E. Kroll, "Multiple jets in electrospinning: Experiment and modeling," *Polymer (Guildf).*, 2005.
[158] H. S. SalehHudin, E. N. Mohamad, W. N. L. Mahadi, and A. Muhammad Afifi, "Multiple-jet

electrospinning methods for nanofiber processing: A review," *Materials and Manufacturing Processes*. 2018.
[159] Y. K. Wu, L. Wang, J. Fan, et al., "Multi-jet electrospinning with auxiliary electrode: The influence of solution properties," *Polymers (Basel).*, 2018.
[160] Y. Zhang, Z. Cheng, Z. Han, et al., "Stable multi-jet electrospinning with high throughput using the bead structure nozzle," *RSC Adv.*, 2018.
[161] A. Jaworek and A. Krupa, "Jet and drops formation in electrohydrodynamic spraying of liquids. A systematic approach," *Exp. Fluids*, 1999.
[162] C. Pu, J. He, S. Cui, and W. Gao, "Double-nozzle air-jet electrospinning for nanofiber fabrication," *J. Appl. Polym. Sci.*, 2014.
[163] J. He, K. Qi, L. Wang, et al., "Combined application of multinozzle air-jet electrospinning and airflow twisting for the efficient preparation of continuous twisted nanofiber yarn," *Fibers Polym.*, 2015.
[164] I. C. Um, D. Fang, B. S. Hsiao, A. Okamoto, and B. Chu, "Electro-spinning and electro-blowing of hyaluronic acid," *Biomacromolecules*, 2004.
[165] Y. X. Zhao, X. H. Zhou, L. Li, et al., "Preparation of porous CeO2/CuO/Al2O3 fibers via electro-blown spinning method," *Mater. Lett.*, 2016.
[166] S. H. Kim, S. H. Kim, S. Nair, and E. Moore, "Reactive electrospinning of cross-linked poly(2-hydroxyethyl methacrylate) nanofibers and elastic properties of individual hydrogel nanofibers in aqueous solutions," *Macromolecules*, 2005.
[167] J. P. Theron, J. H. Knoetze, R. D. Sanderson, et al., "Modification, crosslinking and reactive electrospinning of a thermoplastic medical polyurethane for vascular graft applications," *Acta Biomater.*, 2010.
[168] Y. Ji, K. Ghosh, B. Li, et al., "Dual-syringe reactive electrospinning of cross-linked hyaluronic acid hydrogel nanofibers for tissue engineering applications," *Macromol. Biosci.*, 2006.
[169] H. Pan, L. Li, L. Hu, and X. Cui, "Continuous aligned polymer fibers produced by a modified electrospinning method," *Polymer (Guildf).*, 2006.
[170] X. Cui, L. Li, J. Xu, and F. Xu, "Fabrication of continuous aligned polyvinylpyrrolidone fibers via electrospinning by elimination of the jet bending instability," *J. Appl. Polym. Sci.*, 2010.
[171] F. Xu, L. Li, and X. Cui, "Fabrication of aligned side-by-side TiO 2/SnO 2 nanofibers via dual-opposite-spinneret electrospinning," *J. Nanomater.*, 2012.
[172] R. Kessick, J. Fenn, and G. Tepper, "The use of AC potentials in electrospraying and electrospinning processes," *Polymer (Guildf).*, 2004.
[173] S. Sarkar, S. Deevi, and G. Tepper, "Biased AC electrospinning of aligned polymer nanofibers," *Macromol. Rapid Commun.*, 2007.
[174] Z. Sun, E. Zussman, A. L. Yarin, J. H. Wendorff, and A. Greiner, "Compound Core-Shell Polymer Nanofibers by Co-Electrospinning," *Adv. Mater.*, 2003.
[175] D. Han and A. J. Steckl, "Superhydrophobic and oleophobic fibers by coaxial electrospinning," *Langmuir*, 2009.
[176] J. P. Chen, S. H. Chen, and G. J. Lai, "Preparation and characterization of biomimetic silk fibroin/chitosan composite nanofibers by electrospinning for osteoblasts culture," *Nanoscale Res. Lett.*, vol. 7, no. 1, pp. 1–11, 2012.
[177] J. Merchiers, W. Meurs, W. Deferme, et al., "Influence of polymer concentration and nozzle material on centrifugal fiber spinning," *Polymers (Basel).*, 2020.
[178] R. H. Colby, "Structure and linear viscoelasticity of flexible polymer solutions: Comparison of polyelectrolyte and neutral polymer solutions," *Rheologica Acta*. 2010.
[179] M. Lavorgna, F. Piscitelli, P. Mangiacapra, and G. G. Buonocore, "Study of the combined effect of both clay and glycerol plasticizer on the properties of chitosan films," *Carbohydr. Polym.*, vol. 82, no. 2, pp. 291–298, 2010.
[180] M. F. Queiroz, K. R. T. Melo, D. A. Sabry, G. L. Sassaki, and H. A. O. Rocha, "Does the use of chitosan contribute to oxalate kidney stone formation?," *Mar. Drugs*, 2015.
[181] D. Ge, L. Yang, C. Wang, et al., "A multi-functional oil-water separator from a selectively pre-wetted superamphiphobic paper," *Chem. Commun.*, 2015.
[182] J. P. Abulencia and L. Theodore, *Fluid Flow for the Practicing Chemical Engineer*. 2010.
[183] NACALAI TESQUE, "No Title." [Online]. Available: https://www.nacalai.co.jp/ss/ec/EC-srchdetl.cfm?Dum=1&syohin=1981065&syubetsu=3. [Accessed: 02-Sep-2020].

[184] T. Klein, S. Yan, J. Cui, et al., “Liquid Viscosity and Surface Tension of n-Hexane, n-Octane, n-Decane, and n-Hexadecane up to 573 K by Surface Light Scattering,” *J. Chem. Eng. Data*, 2019.
[185] NACALAI TESQUE, “No Title.” [Online]. Available: https://www.nacalai.co.jp/ss/ec/EC-srchdetl.cfm?Dum=1&syohin=1792175&syubetsu=3. [Accessed: 02-Sep-2020].
[186] S. A. Mumford and J. W. C. Phillips, “The physical properties of some aliphatic compounds,” *J. Chem. Soc.*, 1950.
[187] FUJIFILM Wako Pure Chemical Corporation, “No Title.” [Online]. Available: https://labchem-wako.fujifilm.com/jp/product/spec_03-0127.pdf?jeAttribute=E. [Accessed: 02-Sep-2020].
[188] FUJIFILM Wako Pure Chemical Corporation, “No Title.” [Online]. Available: https://labchem-wako.fujifilm.com/us/product/spec_20-0368.pdf?jeAttribute=E. [Accessed: 02-Sep-2020].
[189] D. H. Reneker and A. L. Yarin, “Electrospinning jets and polymer nanofibers,” *Polymer*. 2008.